



University  
of Glasgow

Santiago Prieto, Ricardo Ignacio (2014) *Transient gravitational waves at r-mode frequencies from neutron stars*. PhD thesis.

<http://theses.gla.ac.uk/5530/>

Copyright and moral rights for this thesis are retained by the author

A copy can be downloaded for personal non-commercial research or study, without prior permission or charge

This thesis cannot be reproduced or quoted extensively from without first obtaining permission in writing from the Author

The content must not be changed in any way or sold commercially in any format or medium without the formal permission of the Author

When referring to this work, full bibliographic details including the author, title, awarding institution and date of the thesis must be given



---

# Transient Gravitational Waves at $r$ -mode Frequencies from Neutron Stars

---

Ricardo Ignacio Santiago Prieto, M.Q.Eng.

School of Physics & Astronomy  
College of Science & Engineering  
University of Glasgow

Submitted in fulfilment of the requirements  
for the Degree of Doctor of Philosophy

September 2014

© R. I. Santiago Prieto 2014

# Abstract

A search for long transient gravitational waves associated with neutron stars is presented. The estimated length of these sources is from hours to weeks. Two types of astrophysical sources are considered: pulsar timing glitches associated with  $r$ -modes oscillations in the interior of isolated neutron stars, and Type I X-Ray bursts in neutron stars from binary systems. These signals follow the model of an  $e$ -folding sinusoid signal with a duration dependant on dissipation processes in the interior of the neutron stars and the gravitational radiation reaction. Estimations of the timescales of gravitational wave signals emitted by stable stars are presented. From this study, it is concluded that detecting signals from faster spinning neutron stars is more feasible than from slower neutron stars.

The study of this type of transient gravitational wave signals is explored for the first time using an adaptation of the  $\mathcal{F}$ -statistic gravitational wave search method used regularly in continuous gravitational wave searches. This adaptation, proposed by Prix et al, is a search methodology in which the duration of a signal plays a significant role in its detection. This code is part of the LAL/LAL-apps data analysis algorithm libraries of the LIGO and VIRGO scientific collaborations (LVC). The use of this method in the gravitational wave search presented in this thesis was implemented in two different environments: gaussian noise data and data in gravitational wave detector-like noise. For the latter, injections of long transient signals with durations  $\sim 10^4$  s on the LVC

Engineering Run 3 were done.

A comparison between the results obtained in these two studies is presented. It shows that, by having a good characterisation of unwanted noise lines, it is possible to distinguish the frequency of the injected signal within a small search band of only a few frequency bins. On the other hand, the recovery of the duration of the signal would require a broad search band over time. This estimation is set to be approximately  $\pm\tau$ , where  $\tau$  is the damping time of the injected signal, in order to construct a complete  $\tau$  distribution. For example, for a signal that last  $\sim 3.5$  days, an total  $\tau$  interval of  $\sim 6.5 - 7$  days is required.

# Declaration

I hereby declare that all the elements presented in this thesis are of my own authorship, except where explicitly indicated in the text. Particularly, the theoretical calculations in chapter 3 were done in collaboration with Dr D. Ian Jones. All other numerical calculations in this chapter are my own work. This thesis is the result of the research I carried out in the Institute for Gravitational Research at the University of Glasgow between October 2009 and April 2014. This work has not been submitted for any other degree at the University of Glasgow or any other institution.

Ricardo Ignacio Santiago Prieto

# Acknowledgements

I would like to thank my PhD supervisors Dr Ik Siong Heng and Professor Graham Woan, from whose knowledge, experience and patience, the roots of this work began to grow and kept doing so until the end of the writing of this thesis. Thanks to Dr Ian Jones and Dr James Clark. All the help I received from you was essential to the results of this research. Thanks to Dr Reinhard Prix and Dr Stefanos Giampanis for all the time they spent in discussions and emails helping me understand the  $\mathcal{F}$ -statistic code.

It is very important to me to thank specially the Institute for Gravitational Research at the University of Glasgow. Moving to a new country is a challenging task, but the fortune to work in a such friendly and competitive group made this much easier. Being part of you was an experience that, I am sure, not all the people have. Thank you Professor Jim Hough, Professor Sheila Rowan and Professor Ken Strain for the opportunity and the support throughout my studies in Scotland. Thanks Russell Jones for the first scottish hand I shook, that was the preview of the fantastic time I had. Thank you all for all the good moments.

Thank you to the University of Glasgow and the Overseas Research Students Awards Scheme (ORSAS) for funding this research.

Thanks to all the people involved in the Journal Club: Martin, Graham, Siong, Yiming, Xilong, Chris, Jade, Gareth, Matt. Thanks to Matt and later to Yiming for organising it. In my passing through the IGR I shared office

with many interesting people. Thank you Craig Lawrie for my training in the (very) strong scottish accent, to Mr Alastair Grant for the uncountable stories about his country and all the experience, and to Steven O' Shea for the nice talks. Thanks to Matt Abernathy. Whenever you want, the spanish lessons can continue on this side of the Rio Bravo (Grande). To Colin Gill: in Mexico I will always have good guacamole to share. Thanks to Josh Logue for being a good friend and for being always a good reference of a tidy desk. Thanks to Matt Pitkin and Chris Messenger for always being there when I sneak into their offices asking questions. I will always remember Erin Macdonald, Gareth Davies and Jade Powell for always being so smiley. While in Scotland I also learnt two things: football and hillwalking. Thank you for the unforgettable games: Euan C., Euan B., Sat, Eric, Peter, Gail, Craig, Siong, Heather. Gail, thanks for the incredible adventures throughout Scotland that you shared with us. Those views are now indelible images in our hearts.

Quiero agradecer a todos los que hicieron de mi vida en Glasgow una de las experiencias más hermosas de mi vida. Primero a mis padres, Rico y Mima, a quienes debo todo. Con semejante empujonte, no podría hacer menos. A ustedes esto y mucho más. A Ana Ceci mi hermana, mi primera amiga, mi amiga eterna. A Javi y a su entrega día a día. Al amor que los unió y trajo a mi vida a Paolita y a Mari. Hijas: A ustedes esta plataforma de lanzamiento. Gracias Efrén y Cristina. Amo tanto apoyo y consejos y los agradeceré siempre. A mi querida Flavita, la primera amiga, gracias por esas charlas tan buenas, por las controversias lingüísticas, y nuestra introducción a Chilito po'. Desde Millport hasta la entrega de la tesis. Y aún habrá más. A la Latinoamérica que conocí: Carlitos, Federico y Claudia, Cristobal y Paulina, Tania y Alan, Nano y Jou, Gaby e Inti, Silvita, Danilinho, Juan

Pablo, Fiorella, Daniela, Ademar (son of Ademar - son of Ademar), Cecinho (golero). Inolvidables tardes-noches-madrugadas con ustedes. ¡Viva Latinoamérica! Al México lindo y querido que me acompañó: Rafael (Pinocho), Ger y Steph, Carmina, Alan y Paulina, Hegel, Emmanuel, Jorge Ricardo (mi tocayo-vecino y gran amigo), Anya y Simon, Angie y Jamie, Miguel y Carmie, Cristina, Chucho, Johnny, Juan Carlos Nambo. A los jugadores en Leeds. Un honor ser campeón a su lado. Al conjunto intersección de México-Europa: Cesarú, Juan y Natalie (y el (la) que viene en camino), Diego y Klotildi, Armando y Cri. Que grandes ilusiones las de reencontrarnos, y lo mejor es que siguen siendo.

Gracias a los que dejé en México. Alejandro León de la Barra, todos los días son oportunidades para aplicar la sabiduría compartida. Y seguiré el consejo de mantenerme haciendo lo que más me gusta. Yuri, Checo, Leo, Mario, Alejandro, ha valido la pena el dejar de compartir, gracias mis hermanos.

A mis compadres, Ana y Luis y nuestra ahijada, Carmen, que nos une. Siempre querremos más tiempo para compartir. Y así será.

Cristy linda, mi Cristy, mi eternidad: A ti todo el esfuerzo, las lágrimas y las carcajadas. Gracias por los años, por la edición de esta tesis y la edición de mi vida. Gracias por esos ojos que hacen que valgan la pena los días más nublados. A tu sonrisa, tu valentía, tu pureza. Al ejemplo que me das todos los días. Tu existencia, belleza mía, hace de este mundo uno mejor. Gracias mi amor. En ti todo, sin ti nada.

# Contents

<b>List of Figures</b>	<b>x</b>
<b>List of Tables</b>	<b>xiii</b>
<b>Preface</b>	<b>1</b>
<b>1 Gravitation</b>	<b>3</b>
1.1 Historical Review . . . . .	4
1.2 General Relativity . . . . .	5
1.2.1 Geometrical description . . . . .	6
1.2.2 Energy-momentum description . . . . .	8
1.2.3 Summary . . . . .	9
1.3 Gravitational waves . . . . .	9
1.4 Gravitational wave detectors . . . . .	11
1.4.1 The first approach . . . . .	12
1.4.2 Laser interferometry and PTA . . . . .	14
1.4.3 The future . . . . .	19
1.5 Gravitational wave classification . . . . .	21
1.5.1 Transient gravitational waves . . . . .	22
1.5.2 Non-transient gravitational waves . . . . .	25
1.5.3 Summary . . . . .	26

<b>2</b>	<b>Neutron stars</b>	<b>28</b>
2.1	Historical review . . . . .	29
2.2	Neutron star structure . . . . .	31
2.3	Pulsars . . . . .	33
2.4	Neutron star transients . . . . .	35
2.4.1	Glitches in radio pulsar observations . . . . .	36
2.4.2	Type I X-ray bursts . . . . .	40
2.4.3	Summary . . . . .	41
2.5	Quasi-normal mode oscillations in neutron stars . . . . .	42
2.6	Neutron star instabilities . . . . .	44
2.6.1	Chandrasekhar-Friedman-Schutz mechanism . . . . .	44
2.6.2	$r$ -modes in neutron stars . . . . .	46
<b>3</b>	<b>Gravitational wave emission and signal attributes</b>	<b>48</b>
3.1	Pulsar beam orientation . . . . .	49
3.2	The $r$ -modes waveform . . . . .	51
3.2.1	Amplitude of the waveform . . . . .	51
3.2.2	Frequency of the waveform . . . . .	52
3.2.3	Characteristic time . . . . .	53
3.3	Gravitational wave energy and detection statistic . . . . .	59
3.4	Gravitational wave energy modulation . . . . .	62
3.4.1	The $\beta$ parametrisation . . . . .	63
3.5	Neutron star transients detection . . . . .	65
3.5.1	Pulsar glitch detection . . . . .	66
3.5.2	Type I X-ray burst transients detection . . . . .	68
3.5.3	Refinement of the Levin & Ushomirsky model . . . . .	70
3.6	Numerical estimates . . . . .	72
3.6.1	Stabilised LMXBs . . . . .	78

3.6.2	Summary . . . . .	80
<b>4</b>	<b>Search for long transient gravitational waves from <math>r</math>-modes</b>	<b>81</b>
4.1	Gravitational wave data . . . . .	82
4.2	Matched Filtering . . . . .	83
4.2.1	Signal-to-noise ratio of transient signals . . . . .	83
4.2.2	$\mathcal{F}$ -statistic in long transient gravitational wave searches	84
4.3	Heterodyning . . . . .	86
4.4	Search for long transient gravitational waves in simulated data	90
4.4.1	Data generation and signal injections . . . . .	91
4.4.2	Gravitational wave search methodology . . . . .	98
4.4.3	Performing a search for long transient gravitational waves . . . . .	99
4.4.4	Results . . . . .	103
4.4.5	Signal duration uncertainty . . . . .	108
4.4.6	Summary . . . . .	110
<b>5</b>	<b>Search for long transient gravitational waves in the Engineering run 3 analysis</b>	<b>111</b>
5.1	Data Generation: Engineering Run 3 . . . . .	112
5.1.1	Coloured noise data analysis . . . . .	114
5.2	Transient Signal Injections . . . . .	116
5.3	Science data . . . . .	122
5.4	Noise characterisation . . . . .	126
5.4.1	Unwanted noise lines . . . . .	127
5.5	Results . . . . .	132
5.5.1	V1 Reinjections . . . . .	137
5.5.2	Signal distribution in ER3 data . . . . .	141

5.5.3 Summary . . . . .	142
<b>6 Conclusions</b>	<b>143</b>
<b>Appendices</b>	<b>147</b>
<b>A Pulsar glitches database</b>	<b>147</b>
<b>B Uncertainties</b>	<b>155</b>
B.1 Uncertainties on $d\tau$ . . . . .	155
B.2 Uncertainties on $F^{1/2} \left( \frac{\delta u}{u} \right)^2$ . . . . .	156

# List of Figures

1.1	GW polarisations and their effect on gravitational wave detectors	11
1.2	Principles of a laser-based gravitational wave detector . . . . .	16
1.3	Advanced LIGO sensitivity curves and design sensitivity curves of current and future gravitational wave detectors. . . . .	17
1.4	LIGO Science Runs $S1 - S5$ . . . . .	18
2.1	Neutron star lighthouse beacon model and structure. . . . .	30
2.2	Pulsar characteristic age (P $\dot{P}$ diagram). . . . .	35
2.3	Representation of a pulsar timing glitch. . . . .	37
2.4	Frequent glitching pulsars. . . . .	38
2.5	Glitches vs distance and $\Delta\Omega/\Omega$ . . . . .	39
3.1	Graphical representation of the inclination angle $\iota$ and the po- larisation angle $\psi$ of a NS. . . . .	50
3.2	Slippage parameter $\delta u/u$ in the crust core interface of the NS. . . . .	56
3.3	$r$ -mode timescales . . . . .	58
3.4	$\delta u/u$ tuning with respect to $f_{\text{star}}$ . . . . .	60
3.5	Zoom in to $\delta u/u$ tuning with respect to $f_{\text{star}}$ . . . . .	61
3.6	The damping time $\tau$ as a function of the frequency $\omega$ for dif- ferent values of $\beta$ . . . . .	65
3.7	Detection parameter $h_{\text{rss}}$ for pulsar glitches. . . . .	68

3.8	$h_{\text{rss}}$ of glitches and Type I X-Ray bursts and gravitational wave detectors sensitivity curves. . . . .	72
3.9	$h_{\text{rss}}$ of glitches from MSP. . . . .	74
3.10	$h_{\text{rss}}$ for selected sources with gravitational wave detector sensitivity curves. . . . .	76
3.11	$h_{\text{rss}}$ of LMXBs in the stable regime and gravitational wave detectors sensitivity curves. . . . .	79
4.1	Heterodyning process in the time domain. . . . .	88
4.2	Heterodyning result in the frequency domain. . . . .	91
4.3	Transient windows with <code>Mfdv4</code> . . . . .	93
4.4	Transient signal adaptation of the CW analysis. . . . .	95
4.5	The effect of the polarisation angle $\psi$ and the inclination angle $\iota$ on a signal simulated with <code>Mfdv4</code> . . . . .	97
4.6	Search method of <code>CFSv2</code> . . . . .	102
4.7	Comparison of <code>CFSv2</code> output $2\mathcal{F}$ and $\max 2\mathcal{F}$ in a frequency band of 0.1 Hz (top) and 1 Hz (bottom). . . . .	103
4.8	Output distributions of $\tau$ and $f_{\text{signal}}$ associated with $\max 2\mathcal{F}$ for signals of $\rho_{\text{opt}}^{f_{\text{crit}}=640} \approx 11.6$ . . . . .	105
4.9	Output distributions of $\tau$ and $f_{\text{signal}}$ associated with $\max 2\mathcal{F}$ for signals of $\rho_{\text{opt}}^{f_{\text{crit}}=730} \approx 4.2$ . . . . .	106
4.10	Output distributions of $\tau$ and $f_{\text{signal}}$ associated with $\max 2\mathcal{F}$ for signals with $5 \times \rho_{\text{opt}}^{f_{\text{crit}}=640} \approx 56.5$ . . . . .	107
4.11	Output distributions of $\tau$ and $f_{\text{signal}}$ associated with $\max 2\mathcal{F}$ for signals with $5 \times \rho_{\text{opt}}^{f_{\text{crit}}=730} \approx 21$ . . . . .	107
5.1	Injection methodology and validation . . . . .	118
5.2	Noise floor methodology and validation. . . . .	119
5.3	Noise floor for injection 1 in L1. . . . .	120

5.4	Noise floor for injection 2 in V1 . . . . .	120
5.5	Only noise frame file vs Signal + noise frame file. . . . .	121
5.6	Long transient signal injections in ER3. . . . .	124
5.7	CFSv2 spectrum in coloured noise data. . . . .	127
5.8	CFSv2 spectrum in coloured noise data with signal injected. . .	128
5.9	CFSv2 spectrum of voltage harmonics and injected signal. . . .	128
5.10	Voltage harmonics data glitches and injected signal peak. . . .	129
5.11	Voltage harmonic removal. . . . .	130
5.12	CFSv2 spectrum with removed voltage harmonics and injected signal. . . . .	130
5.13	CFSv2 spectra of the VIRGO gravitational wave detector around the injected signal frequency of 826.6 Hz. . . . .	131
5.14	Noise + signal distributions of Injection 1 in H1 before and after the unwanted noise lines removal. . . . .	133
5.15	ER3 noise distributions with long transient gravitational wave injections. Recovered injections 1 in H1 and L1. . . . .	135
5.16	ER3 noise distributions with long transient gravitational wave injections. Injections 2 and 3 in L1. . . . .	136
5.17	Reinjection methodology and validation . . . . .	138
5.18	Spectrum of the reinjected 10× the original signal in V1 data.	139
5.19	Spectrum of the reinjected 5× the original signal in V1 data. .	139
5.20	Noise distribution of the reinjected 10× the original signal in V1 data. . . . .	140
5.21	Noise distribution of the reinjected 5× the original signal in V1 data. . . . .	140
5.22	CFSv2 distributions of 20 injections in ER3 data . . . . .	142
B.1	90% confidence interval calculation . . . . .	155

# List of Tables

1.1	The modern resonant-bars gravitational wave detectors . . . . .	13
1.2	Gravitational wave classification . . . . .	27
2.1	Pulsar classification . . . . .	34
2.2	Type I X-ray burst classification . . . . .	41
3.1	Representative sources for the analysis . . . . .	74
3.2	Type I X-Ray sources tested for detectability . . . . .	79
4.1	Commands of the <code>lalapps_Makefakedata_v4</code> . . . . .	94
4.2	Commands of the <code>lalapps_ComputeFStatistic_v2</code> . . . . .	101
4.3	Parameters of the source used in the analysis. . . . .	104
4.4	Uncertainties on $d\tau_{90\%}$ and $F^{1/2}(\delta u/u)^2$ . . . . .	109
5.1	Engineering Runs dates. . . . .	113
5.2	Parameters of the signals injected in ER3 noise. . . . .	116
5.3	ER3 science segments for long transient signal injections. . . . .	117
5.4	ER3 science segments of transient signals. . . . .	123
5.5	Parameters of the signals injected in ER3 noise. . . . .	125
5.6	Data loss after unwanted noise lines removal. . . . .	132
5.7	$2\mathcal{F}/\max 2\mathcal{F}$ values of long transient signals injected in ER3. . . . .	134
5.8	Reinjections in V1 ER3 data. . . . .	137

A.1 Pulsar glitch data base used in this analysis . . . . . 148

# Nomenclature

$\alpha_p$	Pulsar magnetic inclination angle
$\Delta\Omega$	Measurement of the increase in the rotational frequency relative to the initial rotational frequency $\Omega$ during a glitch
$\iota$	Inclination angle
$\Omega$	Pulsar rotation rate = $2\pi f_{star}$
$\omega$	Angular mode frequency = $2\pi f_{rot}^{mode}$
$\Omega_k$	Keplerian rotational frequency
$\psi$	Polarisation angle
$\rho_s$	Nuclear equilibrium density $\cong 2.7 \times 10^{14} \text{ g cm}^{-3}$
$c$	Speed of light = $299,792,458 \text{ m s}^{-1}$
$f_{inertial}^{mode}$	$r$ -mode frequency in the inertial frame
$f_{rot}^{mode}$	$r$ -mode frequency in the rotating frame
$f_{star}$	Pulsar spin frequency
$M_{\odot}$	One solar mass = $1.9891 \times 10^{30} \text{ kg}$
$R_6$	NS radius in Levin & Ushomirsky notation = $1.17 \times 10^6 \text{ cm}$ .

AXP Anomalous X-Ray Pulsars

G Gravitational constant =  $6.67384 \times 10^{-11} \text{ m}^3 \text{ kg}^{-1} \text{ s}^{-2}$

GRR Gravitational Radiation Reaction

MJD Modified Julian Date

MSP Millisecond Pulsars

QNM Quasi-normal modes

SGR Soft Gamma-Rays Repeaters

# Preface

Understanding the where and when of the human existence in the Universe is one of the most ancient questions, and probably will always be present. This question has led to the development of several interpretations of the Universe. Throughout the centuries, technology has been the cornerstone to help nature's observers to answer these and many other queries. In this context, the initial questions of the 'where' and 'when' have been relatively satisfied, giving rise to more complicated questions like 'why' or 'how'.

A set of ideas that are just a small sample of the great creativity that scientists have had is included in the following pages. These fantastic ideas have set all the elements to write these lines that are about violent phenomena that happened far away and, in consequence, correspond to a past in which none of us were alive.

Firstly, in chapter 1 the fundamental ideas of modern gravitation are presented. Particularly, a general description of the Theory of General Relativity proposed by Albert Einstein is given. Also, the concept of a gravitational wave is discussed. Then, the generalities of the past, current and future gravitational wave detectors are discussed, as well as the main gravitational wave sources in which the gravitational wave spectrum is classified. A gravitational wave classification that distinguishes transient from non-transient gravitational waves is also presented in this chapter. All these concepts set the basis of this study and are essential for the validation of some equations

throughout the text.

Then, in chapter 2 a description of the neutron star model that is considered in this thesis is presented. Neutron stars transients like pulsar glitches and Type I X-ray bursts are described. Finally, a discussion of quasinormal modes of oscillation in neutron stars, considering the Chandrasekhar-Friedman-Schutz mechanism and the  $r$ -mode mechanism, is presented.

Chapter 3 gives a description of the gravitational wave signals used in this work. In this chapter, the Levin & Ushomirsky model for the timescale of a gravitational wave associated with pulsar glitches is described. A discussion about the amount of energy that is transferred from the glitch to the gravitational wave is presented through the definition of a parameter  $\beta$ . In the context of the Type I X-Ray bursts, a reinterpretation of the Levin & Ushomirsky model in which the fastest pulsars are stabilised is presented. Finally, some numerical estimates using all the equations discussed in this chapter are given.

Chapters 4 and 5 present the results of a detection analysis of long transient gravitational waves in white noise and in coloured noise, respectively. These analyses follow the methodology developed by Prix et al [1] in which an adaptation of the  $\mathcal{F}$ -statistic search for transient gravitational waves is proposed. These two final chapters contain results that have to be contrasted with each other in order to validate a search over real data of these kinds of signals.

# Chapter 1

## Gravitation

This is an introductory chapter to the science behind gravitational waves. Firstly, a review of the development of this science from a historical perspective is discussed culminating with a description of the General Theory of Relativity. Secondly, the essential elements of General Relativity such as the Einstein field equations are presented. In this section, the analysis of these field equations is discussed from both a geometric and an energy-momentum perspective. With these elements, gravitational waves are defined as a solution of the field equations. Then, a review of gravitational wave detectors from the resonant bars to the current laser interferometers, including a brief description of the future detectors, is discussed. Finally, a classification of gravitational waves based on their duration is presented. In this classification, a distinction between transient and non-transient gravitational waves is discussed and from this main classification a sub-classification based on the astrophysical sources is presented.

## 1.1 Historical Review

Gravitation is an interpretation of the Universe, of how it behaves and how it looks like. The word comes from the latin etymology *gravitās* that refers to weight or heaviness. So, in principle, any event in the Universe that involves an object with weight can be interpreted as a gravitational event. Since the time of the Greeks it was known that there is no motion without a cause and the interpretation of the Universe was based on answering questions like why the Universe behaves in such a way rather than how things work. A series of refinements trying to answer this question have taken place throughout time. It was after the great contributions of Nicolas Copernicus (1473-1543) and Galileo Galilei (1564-1642), that Sir Isaac Newton (1642-1727) proposed a geometrical description of why the Universe behaves like it does. He found the link between the trajectory of a free-falling object on Earth and the orbits of the planets around the Sun. This was an amazing achievement, but the question of how this happened was only partially solved. This idea assumed that gravitational events have causes that “transmit” instantaneously their effects. This implies that these effects have an *infinite* nature. A medium in which objects move had to be considered ‘infinitely’ rigid, allowing ‘infinite’ speeds. After them, Albert Einstein (1879-1955) made public a revolutionary concept of the understanding of the Universe. Since then, people started to refer to Gravitation as Relativity, although the concept of relativity was previously used by Galileo. In 1905 Einstein published three papers in which he described the brownian motion, the photoelectric effect (for which he received the Nobel prize in 1921 <sup>1</sup>) and a special case of the Theory of Relativity. The

---

<sup>1</sup>Actually, the Nobel committee awarded the prize “for his services to *Theoretical Physics, and especially for his discovery of the law of the photoelectric effect*” [2].

latter has two fundamental postulates, which state that,

1. The rules in which nature behaves are invariant with respect to an inertial observer.
2. The speed of light  $c$  is constant irrespective of whether it is an inertial or non-inertial reference frame in which it is measured.

These postulates set down the rules for the ‘generalisation’ of the theory which was published years later (1914-16) as the General Theory of Relativity (GR). The generalisation of this theory with respect to the special one is based on its capability to describe physical events from the point of view of both accelerated observers, subject to a gravitational field, and inertial observers, who do not feel a gravitational field. Special relativity, in contrast, allows for inertial observer descriptions only. A fact that made GR a novel theory is the proposal of a joint *space-time* that is susceptible of being measured. Newton’s theory cannot be qualified as erroneous because, under certain *non-relativistic* circumstances, describes gravitational events correctly.

## 1.2 General Relativity

The concept of GR is described by the Einstein Field Equations (EFE). This field is composed of 10 equations that, broadly speaking, contain information of two sorts:

- *Geometrical*, which models the way in which space-time is modified in the presence of mass.
- *Energy and momentum*, which describes the amount of momentum that a mass carries as well as the stress that can be applied to the medium.

### 1.2.1 Geometrical description

General Relativity considers the Universe as a medium with some stiffness in which everything coexists. With this interpretation of the Universe as a more ‘flexible’ medium, some geometrical considerations have to be taken into account because, in the presence of massive objects, space-time tends to curve. With the intention of measuring this flexibility, having a *manifold*, which is a geometrical object that generalises the intuitive concept of the *curvature* of a medium, is essential. Furthermore, the concept of curvature can be explained by a *parallel transport of a vector* around a surface that eventually reaches its initial position. If after the transportation the direction of the vector has changed, the angular difference is a measure of the curvature.

As a first step, with the use of well-known references such as the cartesian spatial plane, with  $x$ ,  $y$ ,  $z$  as the spatial coordinates, in combination with a 4th dimension  $t$ , the temporal coordinate, a measuring system called *metric* can be defined. This metric is useful to understand how a manifold is modified. The most simple metric is a flat metric with coordinates

$$(dx_\mu, dx_\nu) = (-ct, x, y, z) \quad (1.1)$$

in which  $\mu$  and  $\nu$  take the values of  $[0, 1, 2, 3]$  corresponding to the coordinates  $[t, x, y, z]$ , respectively. This metric can also be written as

$$\eta_{\mu\nu} = \begin{pmatrix} -1 & 0 & 0 & 0 \\ 0 & 1 & 0 & 0 \\ 0 & 0 & 1 & 0 \\ 0 & 0 & 0 & 1 \end{pmatrix}, \quad (1.2)$$

which is known as the Minkowski metric. With the help of these elements, it is possible to measure distances over the manifold as

$$ds^2 = g_{\mu\nu} dx^\mu dx^\nu, \quad (1.3)$$

that is reminiscent of the traditional pythagorean way to measure distances in flat space except for the  $g_{\mu\nu}$  term, that is called the *metric tensor* and that sets a correction to flat space when in a curved space-time. The standard way to understand the curvature of manifolds is through the Riemann-Christoffel curvature tensor, given by

$$R^\alpha{}_{\mu\beta\nu} = \partial_\beta \Gamma_{\mu\nu}^\alpha - \partial_\nu \Gamma_{\mu\beta}^\alpha + \Gamma_{\mu\nu}^\delta \Gamma_{\delta\beta}^\alpha - \Gamma_{\mu\beta}^\delta \Gamma_{\delta\nu}^\alpha, \quad (1.4)$$

in which the  $\Gamma$  terms are called the Christoffel symbols, that compensate the fact that the derivatives of tensors do not transform between frames of reference. For a vector  $V$  in the frame of reference  $x$ , a Christoffel symbol is defined as

$$\Gamma^r{}_{mn} = \frac{\partial}{\partial y^n} \frac{\partial x^r}{\partial y^m} V(x). \quad (1.5)$$

A contraction of equation 1.4, is set as:

$$R_{\mu\nu} \equiv R^\alpha{}_{\mu\alpha\nu} = \partial_\alpha \Gamma_{\mu\nu}^\alpha - \partial_\nu \Gamma_{\mu\alpha}^\alpha + \Gamma_{\mu\nu}^\delta \Gamma_{\delta\alpha}^\alpha - \Gamma_{\mu\alpha}^\delta \Gamma_{\delta\nu}^\alpha \quad (1.6)$$

and a further contraction to represent the trace of the Ricci curvature is

$$R = g^{\mu\nu} R_{\mu\nu}. \quad (1.7)$$

Equations 1.6 and 1.7 are respectively, the Ricci tensor and the Ricci scalar. Then, with all this in mind, a more general view of how a curved space-time is deformed is expressed with the Einstein tensor  $G_{\mu\nu}$

$$G_{\mu\nu} = R_{\mu\nu} - \frac{1}{2}g_{\mu\nu}R. \quad (1.8)$$

### 1.2.2 Energy-momentum description

The deformation of space-time is an effect of the interaction of any mass distribution with it. This means that the energy and the momentum of these mass distributions are the energy source of the gravitational field in GR. These interactions have to be represented in an invariant way, and are described by a tensor  $T^{\mu\nu}$  called the *stress-energy momentum tensor*. Following [3] and [4], this tensor, in terms of its components at some arbitrary frame of reference, is:

$$\mathbf{T}(\nabla x^\mu, \nabla x^\nu) = T^{\mu\nu} \equiv \left\{ \begin{array}{l} \text{flux of the } \mu \text{ component} \\ \text{of 4-momentum across a} \\ \text{surface of constant } x^\nu \end{array} \right\}, \quad (1.9)$$

in which the  $\mu$  component of the 4-momentum<sup>2</sup> is

$$p^\mu \equiv \langle \nabla x^\mu, \vec{p} \rangle, \quad (1.10)$$

and  $\nabla x^\mu$  is the gradient of  $x^\mu$ . Thus, the change,  $\Delta p^\mu$ , in the  $\mu$  component of the 4-momentum due to the flux through a surface element,  $\Delta S^\nu$ , at constant  $x^\nu$ , is given by

$$\Delta p^\mu = T^{\mu\nu} \Delta S^\nu. \quad (1.11)$$

---

<sup>2</sup>The 4-momentum of a particle is a vector whose components in some reference frame give the particle's energy and momentum relative to that frame.

The tensor  $T^{\mu\nu}$  encodes all the possible interactions that the mass has with a medium: the component  $T^{00}$  represents the mass-energy density  $\rho_E$ , the components  $T^{0i}$  represent the energy flux across the  $x^i$  surface, the components  $T^{i0}$  represent the momentum density, and finally, the components  $T^{ij}$  ( $i, j \neq 0$ ) represent the flux of the  $i$  momentum across the  $j$  surface. Depending on the situation, one or another of the components leads to an approximation of  $T^{\mu\nu}$ . For example, for slow motions, the velocity-dependent components are much smaller than the mass-energy ones, making  $T^{00}$  a good approximation of  $T^{\mu\nu}$ .

### 1.2.3 Summary

Given the description of the geometry of space-time as well as the gravitational interactions that lead to its deformation, the relation of these two concepts, encapsulated in the EFE, is given by

$$G_{\mu\nu} \equiv R_{\mu\nu} - \frac{1}{2}g_{\mu\nu}R = kT^{\mu\nu}, \quad (1.12)$$

in which the coupling constant  $k$  is assumed to have geometric units of  $G = c = 1$ . In a way, the left-hand side of equation 1.12 represents a strain produced by a stress described by the right-hand side of the equation.

## 1.3 Gravitational waves

Riemannian spaces, of which space-time is an example, are locally flat. This means that in a local inertial frame the direction of a vector that is parallel transported around the frame will not change. If a small perturbation  $h_{\mu\nu}$  affects a flat metric, like  $\eta_{\mu\nu}$ , the metric will take the form

$$g_{\mu\nu} = \eta_{\mu\nu} + h_{\mu\nu} \quad \text{with} \quad |h_{\mu\nu}| \ll 1. \quad (1.13)$$

This approximation, called *weak-field approximation*, also assumes that  $T^{\mu\nu} = 0$ , since the flat space-time is considered to be in vacuum or in the absence of energy or mass. Following now [5] the solution to EFE is a wave equation of the form

$$\left( -\frac{1}{c^2} \frac{\partial^2}{\partial t^2} + \nabla^2 \right) h_{\mu\nu} = 0, \quad (1.14)$$

which means that, in this approximation, the metric perturbation has the same mathematical shape of a wave, traveling at the speed of light. The term  $h_{\mu\nu}$  in equation 1.14 can be thought as the *gravitational wave* (GW) field which, according to GR, is *transverse* and *traceless*. Transverse waves contain vibrations perpendicular to their propagation direction. This nature implies that, if the propagation direction is  $z$ , the  $z$ -components of the wave are 0. The traceless condition implies that  $h_{xx} = -h_{yy}$  and  $h_{xy} = h_{yx}$ . In order to make the metric perturbation only spatial, the Lorentz gauge can be chosen [6], so  $h_{tt} = h_{ti} = 0$ , and with all these, the perturbation takes the form:

$$h_{\mu\nu} = \begin{pmatrix} 0 & 0 & 0 & 0 \\ 0 & h_{xx} & h_{xy} & 0 \\ 0 & h_{xy} & -h_{xx} & 0 \\ 0 & 0 & 0 & 0 \end{pmatrix} \quad (1.15)$$

which leads to only two independent polarisation states of the gravitational wave denoted as  $h_+$  and  $h_\times$ . Simple solutions of equation 1.14 will be then

$$h_+ = h_{xx} = -h_{yy} = \text{Re}\{A_+ e^{-i\omega(t-z/c)}\} \quad \text{and} \quad (1.16)$$

$$h_\times = h_{xy} = -h_{yx} = \text{Re}\{A_\times e^{-i\omega(t-z/c)}\}, \quad (1.17)$$

each one corresponding to each polarisation of the wave, and  $A_{\{+,\times\}}$  being the amplitude of each polarisation. Derivations of all the equations in this section

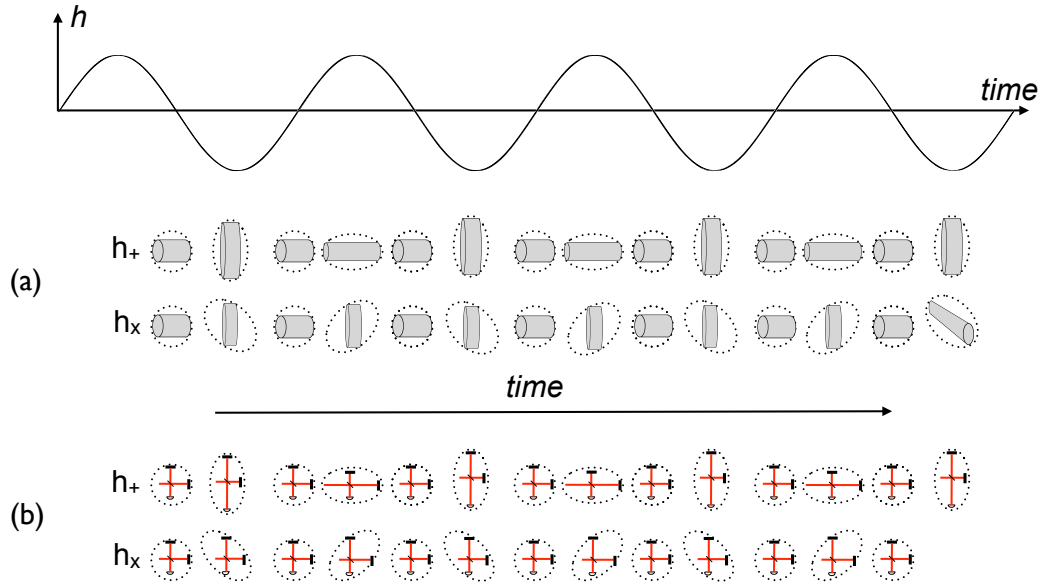


Figure 1.1: **GW polarisations and their effect on gravitational wave detectors over time.** This figure shows the effect of each gravitational wave polarisations over (a) a resonant mass gravitational wave detector and (b) a laser interferometer detector. This figure is partially inspired by figure 1 in [8].

can be found in [3, 4, 6, 7].

If these waves pass near a mass distribution, they will ‘squeeze’ and ‘stretch’ this distribution in the direction of the wave’s polarisations. Particularly, if this mass distribution is set as a gravitational wave detector, as described in section 1.4, it will be modified according to the wave’s polarisation as shown in figure 1.1.

## 1.4 Gravitational wave detectors

After theoretical estimations of the origin of gravitational waves, it was clear by the 1980’s, that gravitational waves could only be detected if the source was extraterrestrial. This gave the character of astronomical to these kind of searches. Until that time, astronomy was limited to electromagnetic searches and the astronomical detectors were built according to this kind of source. With gravitational wave astronomy, something similar has to be done. For

the construction of gravitational wave detectors, two main properties are considered: their capability to have mechanical displacements and the way this can happen through the wave polarisation. The search for gravitational waves has brought an amazing era of creativity that has led to the most accurate way to measuring distances smaller than the size of the nucleus of an atom. The technology involved in gravitational wave detection has improved faster in the recent times and now a ‘first steps era’ can be distinguished from a ‘modern era’. These eras are represented by two different types of gravitational wave detectors, respectively: resonant bars and laser interferometers.

In addition to these ‘eras’, the future detectors also play a fundamental role. These future detectors are under planning and construction and with them the first detection of gravitational waves seems to be imminent.

### 1.4.1 The first approach

Without any doubt, the credit of the first experimental design of a gravitational wave detector has to be given to Joseph Weber (1919-2000), who, during the 1960’s, was the pioneer in the development of instrumentation for the direct detection of gravitational radiation using isolated resonant-mass antennas at the University of Maryland, in the USA. A good review of Joseph Weber’s publications and experiments can be found in [9] and the references therein. After his experiments, a number of other scientists designed and built gravitational wave detectors which were improved versions of Weber’s first designs.

The main aim of these devices is to measure resonances in masses as a consequence of the passing by of a gravitational wave. Each of these devices is a huge aluminium alloy cylindrical mass ( $\gtrsim 1$  ton) hung with vibration isolators and cooled at a cryogenic level. These devices are equipped with a series of

sensors connected to electronics that act as strain detectors of the normal oscillating modes of the mass. The data collection is based on readings related to the amplitude of the resonance of these masses, through transduction principles. In addition to this, in order to have more reliable readings, the results obtained in one of these antennas has to be confirmed by another measurement in a similar device separated by reasonable distance. This helps to get rid of false detection local perturbations, such as earthquakes. Despite the lack of trustable results, the science around these oscillating bar antennas was not unsuccessful. Maryland's and many other research groups around the globe (Rochester, Glasgow, Munich-Frascati, Moscow, Tokyo) set the first standards of experimental considerations and characterisation of gravitational wave data. After them, advances in several areas such as cryogenic principles, computer processing techniques, electronic devices, material properties, thermal noise research and some other areas in physics, have contributed to the field of gravitational wave searches.

Table 1.1: **The modern resonant-bars gravitational wave detectors** [10]

Detector	Weight (kg)	Location	Temp (K)
EXPLORER	2270	CERN, Geneva, CH	2.6
ALLEGRO	2296	Lousiana, USA	4.3
NIOBE	1500	Perth, Australia	5
NAUTILUS	2260	Rome, Italy	0.13
AURIGA	2230	Padova, Italy	0.2

The science of a resonant-mass antenna has been continuously improving and, as a result, a network that pursuits the first detection of gravitational waves is currently in operation. By 1997 there were 5 resonant-bars active in the network (ALLEGRO, EXPLORER, AURIGA, NAUTILUS and NIOBE). Today, there are only three detectors in operation (EXPLORER, NAUTILUS, and AURIGA). Table 1.1 shows an overview of some of their features. Since their

maximum strain sensitivity is in the order of  $10^{-21} \text{ Hz}^{-1/2}$  an improvement in sensitivity is needed. Interferometry-based detectors started to become the way forward.

### 1.4.2 Laser interferometry and PTA

Parallel to the development of resonant-bar technology, some other ideas have been implemented as gravitational wave detection devices like *laser interferometer antennas* and the *Pulsar Timing Array* project (PTA). In the following a brief description of them is presented.

The operational principle of interferometers is comparable to the functionality of a microphone rather than that of an optical telescopes. In some sense, the search for gravitational waves is understood as ‘listening’ the universe instead of ‘observing’ it as in electromagnetic astronomy. The tuning of this ‘microphone’ will define the astrophysical source that it is intended to hear. Given the effect that gravitational wave polarisations have, as seen in figure 1.1, the ‘L’-like shape of a Michelson interferometer makes these devices a sensible tool to be used in the detection of gravitational waves. In principle, while the two reflective mirrors used as test masses are equidistant from the beamsplitter, the arms of the interferometer will have the exact same size and a destructive interference with two superimposed laser beams will happen. As a consequence, no signal will be detected by the sensors set at the recombination point of the interferometer. This principle is shown in a simplified way in figure 1.2(a). On the other hand, if the arms’ length changes even by a very small fraction, a constructive interference takes place and a signal will be recorded. A sketch of this effect is shown in figure 1.2(b). The resulting signal will have similar properties to the gravitational wave signal that induced the mirror displacement in the first place. The amplitude of the signal is generally

denoted as  $h$  and quantified as:

$$\frac{h}{2} \sim \frac{\Delta l}{l}, \quad (1.18)$$

in which  $l$  is the arm length of the interferometer and  $\Delta l$  is the variation of this length as a consequence of the gravitational wave passing by.

Many considerations have to be taken into account to guarantee the reliability in the measurement of a displacement due to a gravitational wave in this kind of detectors: a stable laser beam, novel optical laser cleaning devices, ultra reflective mirror coatings applied to the test masses, and extremely sensitive suspensions to isolate these masses from Earth-originated vibrations and gravity gradient noises. Also in order to avoid light scattering inside the vacuum chambers where the laser beams are propagating, cryogenic temperatures to control as much as possible thermal noise from the test masses and their suspensions are fundamental. The different quantum noise contributions, such as the loss in photon numbers as a function of the position of the sensor in the interference fringe point, called the photoelectron shot noise, and the radiation pressure due to the light scattering produced by the beamsplitter, are very important issues to be taken into account. More details about all these kind of noise sources can be found in [8, 11, 12]. The effect of these noise sources on the sensitivity of a gravitational wave detector is shown in figure 1.3(a). In the same way as with the resonant bars, it is fundamental to have simultaneous gravitational wave detections from different sites to validate a direct detection. Currently there are several gravitational wave detectors all around the world. The **L**aser **I**nterferometer **G**ravitational-wave **O**bservatory, or LIGO detectors, are a series of three detectors in the U.S.A. in two different sites: (1) two detectors at a northwest site in Hanford, Washington: a 4 km-arm length (**H1**) and a 2 km-arm length (**H2**), and (2) one detector at a

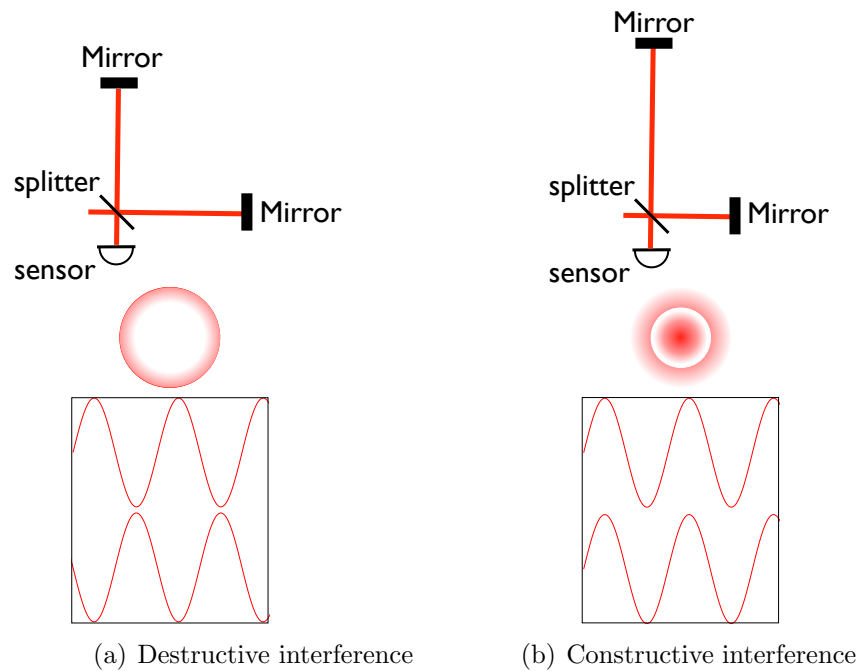


Figure 1.2: **Principles of a laser-based gravitational wave detector.** In this figure a sketch to represent destructive and constructive interferometry with the laser beams of a simplified gravitational wave detector is shown. Real gravitational wave detectors include many other optical devices.

southeast site in Livingston, Louisiana with a 4 km-arm length detector (**L1**). The global network consists of a detector in northern Italy called VIRGO, which is an Italian-French consortium with a 3 km-arm length, a 300 m-arm length detector outside Tokyo, Japan called TAMA and the German-British project GEO600, which has a 600 m-arm length interferometer in Hannover, Germany. The design sensitivity curves of these detectors, as well as future projects which will be discussed in the next section, are provided in figure 1.3(b).

Briefly after starting operation, LIGO and GEO600 agreed to collaborate, since for strong sources, the German-British detector will help to provide more accuracy on the direction and polarisation of such signals. Also LIGO and VIRGO more recently have started to share the analysis effort. They

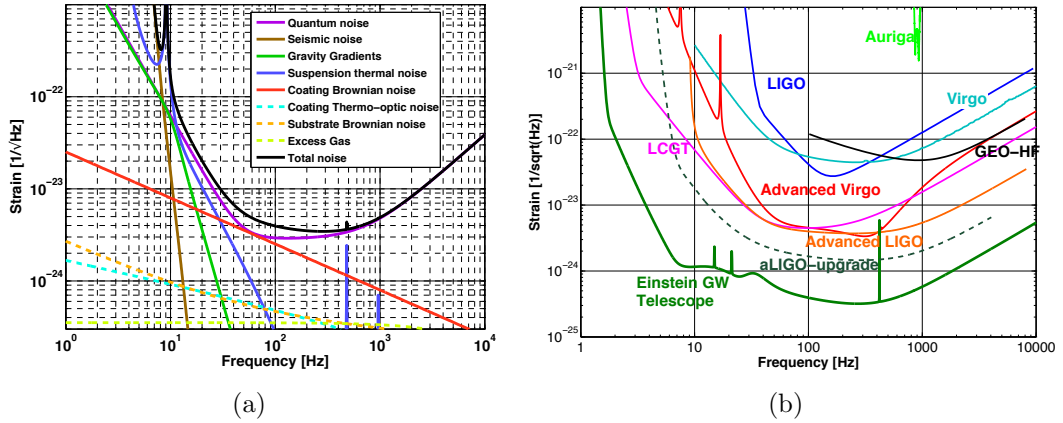


Figure 1.3: **Advanced LIGO sensitivity curves and design sensitivity curves of current and future gravitational wave detectors.** In panel (a) the noise contributions for the Advanced LIGO detector are shown. In panel (b) the sensitivity curves of current and future detectors are shown. In addition, the sensitivity of a resonant bar is shown for comparison. These figures are extracted from [12].

have agreed that all data collections will be analysed and published as a joint collaboration. These detectors have a similar sensitivity above  $\sim 1$  kHz. Until now, there have been six scientific runs with the LIGO detectors which are named “Sn”, where n is the run number. These runs differ from each other on the improved sensitivity reached by the detectors, as shown in figure 1.4. The success of a science run depends on the engineering improvements on different aspects of the detectors and on the correct implementation of the software infrastructure. Between S6 and S7, a major improvement that will lead to the new generation of gravitational wave detectors will happen. This new generation of interferometers are called advanced detectors.

### Advanced LIGO and Advanced VIRGO

Currently, the LIGO and VIRGO detectors are undergoing an engineering upgrade that will lead to ten times better sensitivity than originally designed, as seen in figure 1.3(b). These projects, called Advanced LIGO and Advanced VIRGO, are the next generation of gravitational wave detectors. Some of the

technological improvements for the LIGO detectors are listed below [13]:

- At the most sensitive frequency band, a strain noise of  $3 \times 10^{-24} \text{ Hz}^{-1/2}$  will be achieved. This means that  $\sim 1000$  times more volume of space will be reachable by the detectors.
- The inclusion of a 3rd 4 km-arm length detector in the Hanford site, as an extension to the current 2 km one, is proposed. Signal recycling cavities will also be adapted to allow tuning of the quantum noise contribution improving the sensitivity at some frequencies at the expense of others.
- An increment in the laser power from 10 W to 180 W.
- Better seismic isolation through an innovative quadrupole suspension test mass chain, supported by fused silica fibres.
- Heavier, larger and thicker test masses in order to reduce radiation pressure noise. Innovative coatings that reduce light absorption will be applied to these mirrors.

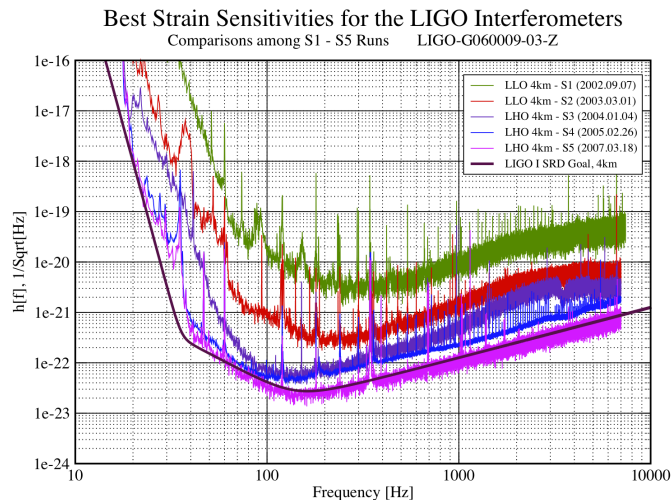


Figure 1.4: **LIGO Science Runs S1 – S5**. This figure, extracted from [14], shows the evolution of the sensitivity of the LIGO detectors in the first five scientific runs. Here LHO stands for LIGO Hanford and LLO for LIGO Livingston.

### **Pulsar timing array (PTA)**

PTA is a project that aims to detect low-frequency gravitational waves in the range of  $10^{-9} - 10^{-8}$  Hz. This project is based on a method that uses a set of millisecond pulsars which are known to have the most accurate pulsation timing ever recorded. The precision in the time of arrival (TOA) that has been achieved is  $\sim 30$  ns for PSR J0437–4715. In principle, the computation of the residuals of the TOA does not consider deviations in the trajectory of the light caused by gravitational waves that add timing residuals. As a consequence, this effect will lead to a variation in the predicted residuals from pulsar observations. This can be translated as a direct observation of gravitational waves. It is believed that a gravitational wave that passes close to a pulsar, the Earth or through the interstellar medium between them, may contribute to a delay in the order of  $10^{-9}$  s in the arrival time of these pulsations. Further details on this project can be found at [15].

### **1.4.3 The future**

There is a linear correlation between the arm length of the interferometers and their sensitivity to detect gravitational waves. With the use of equation 1.18, and considering a gravitational wave with  $h \sim 10^{-23}$  m, a  $\Delta l \sim 10^{-20}$  m in a 4 km interferometer is expected. On Earth there is a limitation of space to build larger interferometers due to the planet's curvature, the cost of large vacuum chambers, etc. These limitations, as well the interest in exploring the low frequency gravitational wave band, are the reasons why an initiative to build a new generation of gravitational wave detectors is now under research and development.

## ET

To achieve the goal of improving the sensitivity by  $\sim$  one order of magnitude with respect to the advanced detectors, the Einstein Telescope (ET) will be built underground at a depth between 100 m - 200 m. This will mainly contribute to the reduction of the residual seismic motion and the spatial rate of change of gravitational acceleration, named gravity gradient noise. The ET configuration consists of three detectors, each one with a pair of interferometers, in a configuration called *xylophone configuration*. In each detector one interferometer will be tuned for low-frequency signals (ET-LF) while the other one will specialise in high-frequency gravitational wave signals (ET-HF).

In ET-LF, by operating at a cryogenic temperature, noise sources like thermal and seismic will be suppressed. On the other hand, in ET-HF the high frequency sensitivity region will be improved by high laser light power and the inclusion of frequency dependant squeezed light technologies. The planned sensitivity curve for this detector is shown in figure 1.3(b). A detailed description of the instrumentation and the astrophysical goals can be found in [16].

## eLISA/NGO

The **e**volve **L**aser **I**nterferometer **S**pace **A**ntenna/**N**ew **G**ravitational Wave **O**bservatory is the latest and most revolutionary gravitational wave detector ever devised. Space-based gravitational wave detectors are designed for low-frequency gravitational waves, and particularly NGO will be tuned to a broad frequency band from  $\sim 0.1$  mHz to 1 Hz [17]. The detector consists of three spacecrafts referred to as *constellation*, that will be ‘optically connected’ via powerful lasers that will measure the distances between them, which are expected to be  $\sim 10^6$  km. The constellation will have a “V” shape with a space-

craft on each of the vertices. The central spacecraft will carry two free-falling masses, and each of these will be linked to the masses inside the spacecrafts at both ends of the baseline. Amongst the sources that a space-based gravitational wave detector could focus on are unresolved compact binaries, Type I supernovae (SNIa), ultra-compact X-ray binaries and black holes (isolated and binary). There are many challenges to build this detector, for example such a long baseline requires powerful lasers. A full description of the project is in [18].

## 1.5 Gravitational wave classification

Any massive object that has a non-spherical motion will produce gravitational waves. This statement opens up the options to a variety of sources that could or could not be detected with the gravitational wave detector infrastructure. This means that any gravitational wave classification will not necessarily be complete because of the unknown sources. Man-made gravitational waves are in principle plausible to be produced but in fact they are undetectable. In [19], Schutz and Sathyaprakash did a theoretical exercise of this possibility and got an estimate of the gravitational wave amplitude of  $h \sim 10^{-43}$  m. They did a thought experiment by rotating in a central pivot a 10 m long beam which has at its edges two 10 kg masses. With these estimates, this possibility is excluded and leaves as an only option sources of astrophysical origin.

Based on the range of frequencies and on the detection methods, Thorne in [20] proposed a classification as follows: *high-frequency waves* (HF) in the range of 1 Hz – 10<sup>4</sup> Hz detectable by ground-based detectors, *low-frequency waves* (LF) in the range of 10<sup>-4</sup> Hz – 1 Hz detectable by space-based detectors, *very-low-frequency waves* (VLF) in the range of 10<sup>-7</sup> Hz – 10<sup>-9</sup> Hz detectable by millisecond-pulsars timing and *extremely-low-frequency waves* (ELF) in the

range of  $10^{-15}$  Hz –  $10^{-18}$  Hz detectable by the analysis of the anisotropy of microwave background. The most investigated frequency ranges nowadays are HF and LF because they are the most sensitive frequencies for current and future detectors. The upper limit for the frequency in which a gravitational wave can be detected is ruled by the mass of the source and cannot have a period larger than  $4\pi GM/c^3$  (the time it takes light to travel around the gravitational radius, given by  $2GM/c^2$ ) [20]:

$$f \lesssim \frac{1}{4\pi GM/c^3} \sim 10^4 \text{ Hz} \frac{M_\odot}{M}. \quad (1.19)$$

From an astrophysical point of view, gravitational waves can be separated as *bursts*, *inspirals*, *continuous* and *stochastic waves*. This classification is highly linked to the data analysis techniques involved in their detection. Furthermore, if their duration is considered, gravitational waves can be classified in two big groups: *transient gravitational waves* and *non-transient gravitational waves*. In this work, this latter classification will be the primary reference.

In the following, a more detailed description of transient gravitational wave sources is provided, compared with the other sources, since they are the main focus of this study.

### 1.5.1 Transient gravitational waves

Transient gravitational wave signals are associated to gravitational events that could be completely detected. In other words, because of its transitory nature, it could be possible to ‘record’ these kind of signals from when they are produced by associating them to some electromagnetic emission until the event ends. The hypothetical recording is based on the fact that a detector is permanently collecting data. They can be subdivided into two classes:

short-duration transients and long-duration transients.

### Short-duration transients

The distinctive feature of these signals is their small duration, in a range from milliseconds to minutes. Their frequency range varies depending on the source which could be burst-type, inspiral or merging-type signals.

#### *Bursts*

There are many plausible sources of this type of gravitational waves, such as core-collapse of massive stars in supernovae explosions (CC SN), coincident emission of gravitational waves with  $\gamma$ -ray bursts (GRB) due to catastrophic energy release in stellar massive objects, anomalous X-ray pulsars (AXPs) or soft  $\gamma$ -ray repeaters (SGR) that are thought to be highly magnetised neutron stars called ‘magnetars’ in which when crustal fractures or non-radial excitation modes are present, gravitational radiation is released. Burst sources tend to have poorly known or unknown signal-phase evolution. On the one hand, this gives the data analysis another uncertainty to be taken into account when modelling signal sources, but on the other hand, because of their short duration, a phase evolution of a signal is not a main contributing factor and in consequence the data analysis techniques are not too sensitive to this feature. In [19], an estimate for the gravitational wave amplitude, assuming prior knowledge of the emitted energy and the duration of the collapse event, leads to

$$h \sim 6 \times 10^{-21} \left( \frac{E}{10^{-7} M_{\odot}} \right)^{1/2} \left( \frac{1 \text{ ms}}{T} \right)^{1/2} \left( \frac{1 \text{ kHz}}{f} \right) \left( \frac{10 \text{ kpc}}{r} \right), \quad (1.20)$$

which in principle could be detected by current gravitational wave detectors. Unfortunately, a problem with these sources is that they do not occur often

and there has not been an event of this kind in the time when gravitational wave detectors have been in operation. For example, Type II supernovae are believed to happen in a rate of 0.1 to 0.01 a year in Milky Way-type galaxies. Magnetised neutron stars are sources of short-duration gravitational waves. These are associated to sudden energy releases from magnetic fields of around  $10^{15} - 10^{16}$  gauss. It is thought that SGRs and AXPs could be different observational interpretations of this same event.

### ***Compact binary coalescence***

A compact binary coalescence or CBC are inspiral events of the merging process that involves two massive and compact objects such as black holes or neutron stars. They could be pairs of neutrons stars (NS-NS), or black holes (BH-BH) or a combination of them (NS-BH). The distinction of these binary systems is that, due to the massive stars that form them, they can undergo a collapse to a more compact object without destroying one of the components of the binary system. The event rate estimations, frequencies and durations depend on the masses of the inspirals and their distances. For example, it is predicted that Advanced LIGO will be able to detect NS-NS inspirals at  $\sim 445$  Mpc, NS-BH at 927 Mpc, and BH-BH out to 2187 Mpc assuming a  $M_{NS} = 1.4 M_{\odot}$  and a  $M_{BH} = 10 M_{\odot}$  [21].

### **Long-duration transients**

This kind of gravitational wave rises as an intermediate classification between burst-type signals and continuous wave signals. The representative astrophysical events associated with this type of signals are instabilities in differential rotation of a collapsing star or at the internal fluid layers of neutron stars. Particularly for the latter, an extensive discussion is provided in chapter 2. In

the last three decades, these astrophysical events associated with currents in the internal fluid component of a neutron star, have raised the interest of scientists since they are susceptible of being associated to transient anomalies in the rotation of these stars and gravitational wave emissions. As they are one of the main subjects of analysis in this thesis, they will be the representative source of emission of this kind of sources within this classification. Particularly, the  $r$ -modes oscillations within the fluid component of the neutron star are a good example of this kind of gravitational wave source and will be also described in detail in chapter 2.

### 1.5.2 Non-transient gravitational waves

This classification stems from two facts: that indeed the nature of the sources is not transitory, that is, their timescale is much longer than the human timescale, or that the observational methods do not allow to record the events for their full duration.

#### *Continuous Waves*

These kind of gravitational waves are associated to long-lasting and nearly monochromatic signals. This monochromaticity refers to a small but measurable change in the phase of the signal. The common astrophysical sources are galactic and non-axisymmetric neutron stars, either isolated or part of binary systems. The lack of symmetry in these stars is related to a mass distribution that alters the roundness of the star and that is the cause of the gravitational wave emission. The roundness of the star can be measured in terms of the eccentricity as

$$\epsilon \equiv \frac{I_{xx} - I_{yy}}{I_{zz}}, \quad (1.21)$$

in which  $I_{xx}$ ,  $I_{yy}$  and  $I_{zz}$  correspond to the moment of inertia in the X-X, Y-Y

and Z-Z axes, respectively. With this in mind, the expected strain amplitude at the gravitational wave detector is given by [22]:

$$h = \frac{4\pi^2 G I_{zz} f_{GW}^2}{c^4 r} \epsilon = 1.1 \times 10^{-24} \left( \frac{I_{zz}}{I_0} \right) \left( \frac{f_{GW}}{1 \text{ kHz}} \right)^2 \left( \frac{1 \text{ kpc}}{r} \right) \left( \frac{\epsilon}{10^{-6}} \right), \quad (1.22)$$

where  $I_0 = 10^{45} \text{ g cm}^3$ , the gravitational wave frequency is twice the spin frequency of the star, and  $r$  is the distance to the source. The detection of gravitational waves of this kind could provide information about the evolution of neutron stars as well as a better understanding of the dynamics in the interior of these stars.

### *Stochastic waves*

These are the gravitational waves of cosmological type. They are a superposition of incoherent sources that includes background gravitational wave radiation from the Big Bang, as well as isotropic emissions from distant supermassive black holes or merging neutron stars. The resulting spectrum of this type of source is commonly described by the gravitational wave energy density per unit frequency normalised by the critical energy density,  $\rho_{\text{crit}} = 3H_0^2 c^2 / 8\pi G$  of the Universe (where  $H_0$  is Hubble's constant):

$$\Omega_{gw}(f) = \frac{f}{\rho_{\text{crit}}} \frac{d\rho(f)}{d\ln(f)}. \quad (1.23)$$

### 1.5.3 Summary

Table 1.2 summarises the classification presented in previous sections and gives an overview to make it easier for the reader to get a notion of the variety of gravitational wave sources.

Table 1.2: **Gravitational wave classification.** In this table a gravitational wave classification based on their transient nature is presented. It is important to highlight an intermediate class of long-transient gravitational wave of which an example are the  $r$ -modes oscillations in NS, subject of this thesis.

Classification		Astrophysical source		Duration [s]	Frequency range [Hz]
Transient	Short	Burst	CC SN GRB SGR	$\lesssim 0.01$ - minutes	$\sim 10^2 - 10^3$ *
		Inspiral	magnetars BH-BH NS-NS BH-NS		$\sim 10^3$ **  $1000 - 3000$ ***
	Long	$r$ -modes in NS (this work)	$\sim 10^3 - 10^5$	$\sim 40 - 200$ † $\sim 800 - 2500$ ‡ $\sim 10^3$ ⊞	
	CW Stochastic	NS Cosmic Background	$> T_{\text{obs}}$ not necessarily contiguous	typically $2 f_{\text{spin}}$ $10^{-18} - 10^4$	
Non-Transient					

\* From newborn boiling neutron star in the first 0.1 seconds of its life ( $\sim 100$  Hz) to its axisymmetric collapse, bounce, and oscillations ( $\sim 200$  Hz –  $10^3$  Hz, [20]).

\*\* NS-NS coalescence is currently a popular explanation for the  $\gamma$ -ray bursts [20].

\*\*\* If an  $f$ -mode emission from the NS is considered, and depending on the equation of state [23].

† If the sum of the BH masses is fairly large,  $\sim 40 - 200 M_{\odot}$ .

‡ The final NS-NS coalescence will emit in this range of frequencies; the upper bounds are not detectable due the shot noise.

⊞ If the BH is less massive than roughly  $10 M_{\odot}$ .

# Chapter 2

## Neutron stars

This chapter introduces the basic concepts that lay the foundations for later chapters. After a brief historical review, the structure, classification and basic characteristics of pulsars are discussed. In order to add further details about the astrophysical sources that are considered in this work, namely *pulsar glitches* and *Type I X-Ray bursts*, the lighthouse beacon model for pulsars first proposed by Gold [24] is discussed. Using a database constructed from [25], [26], [27] and [28], an analysis of the frequent glitching pulsars is presented. Then, a description of quasi-normal modes focused particularly on *r*-modes, which are the gravitational wave emission modes studied in this thesis, is presented. Finally, the description of the *r*-mode instability is presented together with a detailed explanation of the CFS (Chandrasekhar-Friedman-Schutz) instability, since the latter is a good reference for the description of the former.

## 2.1 Historical review

Neutron stars (NS) are fascinating stars. They are amongst the densest objects known and represent a natural laboratory to test extreme conditions of roundness, compactness, spin frequency, density, pressure, and magnetic fields. Their existence was first proposed in 1934 by Baade and Zwicky [29], who argued that the correlation between the amount of cosmic-ray radiation detected on Earth and *supernovae* observations leads to the idea that the latter are a transition phase from ‘regular’ stars to neutron stars.

Today, the most accepted description of the formation of a NS starts with a  $\sim 10 M_{\odot}$  star that uses up its nuclear fuel. After these massive stars undergo a supernova, around 10% of the stellar matter is left. For the most massive remnants, gravity dominates and keeps matter collapsing until it turns into a black hole. If the remnant is  $\sim M_{\odot}$ , the Pauli exclusion principle of degenerate matter keeps neutrons and protons apart and the NS becomes stable [30]. The discovery of radio astronomy along with the development of new theoretical models that predicted the existence of these stars, were the key to the first detection. In 1968, during an experiment which aimed to measure interplanetary scintillation, the observation of periodical pulsations led to the association of these pulsations with NS oscillations. Based on parallax measurements, Antony Hewish, Jocelyn Bell and collaborators, concluded that these pulsations, now known as PSR B1919+21 were coming from outside the Solar System but within the Galaxy. They proposed that these pulsations were originated either by a white dwarf or a NS [31]. The acronym PSR stands for **P**ulsating **S**ource of **R**adio. The subsequent numbers indicate the source’s location in right ascension and declination coordinates. Letters preceding coordinates refer to the epoch: B for epoch 1950 and J for epoch 2000. Appended letters distinguish close pulsars.

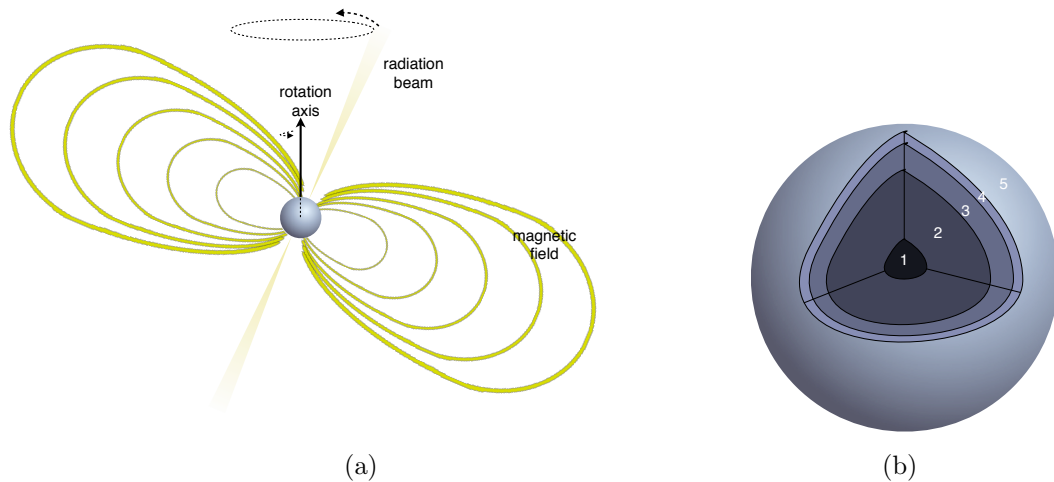


Figure 2.1: **Neutron star lighthouse beacon model and structure.** Panel (a) shows the lighthouse beacon model in which the light beam precesses around the rotational axis because of the non-axisymmetric nature. In panel (b) a representation of the NS layers is presented as follows: 1. the core, 2. the region of neutron superfluid, 3. the solid region with free electrons, 4. the crystalline crust and 5. the surface.

A few months before the discovery of the pulsating sources, Pacini [32] brought up the idea that after the collapse of a supernovae, a strong magnetic field present in the remnant star could act as a dipole. He suggested that the angle between this dipole and the angular momentum vector of the star would be arbitrary since the explosion is unlikely to be symmetric. According to this rotation model, this configuration would lead to electromagnetic energy emission from the NS.

Almost in parallel, Gold [24] published a similar solution to the nature of pulsars. Here, the link between the pulsations and the rotational frequency was described *a priori* to the first observation, setting relativistic effects of a co-rotating magnetosphere as the energy source of the emissions. The link between the pulsations and an actual physical characteristic of the star was also predicted by Gold: “*If the rotation period dictates the repetition rate, the fine structure of the observed pulses would represent directional beam rotating like a lighthouse beacon.*” [24]. During the time when Gold published his

paper, pulsating NS were starting to be called *pulsars* based on the *lighthouse beacon model* whose schematic representation is shown in figure 2.1(a). Later on, Gold, as well as Pacini, predicted a slowing down of such pulsations that was observed not long after in the Crab Pulsar. Other predictions like the presence of pulsars in supernovae remnants were confirmed by observation of the Crab Pulsar and the Vela Pulsar.

Nowadays, the interest in studying these stars lays on the understanding of the physics inside them and the origin and evolution of their pulses in either of the electromagnetic wavelengths like radio, X-ray or  $\gamma$ -ray. The combination of gravitational wave astronomy and electromagnetic astronomy, the so-called *multi-messenger* astronomy, is expected to provide answers to these questions.

## 2.2 Neutron star structure

The structure of a NS is described in this section, as well as the link between these stars and pulsars. Since the scope of this work does not include an extensive analysis of the physics inside NS, only a simple description of their structure is given to provide the reader with a general understanding to follow the research presented in the next chapters. From the innermost layer to the outside, the neutron star's internal structure is composed by [33] :

- A (possibly solid) core with a mean density of  $10^{15} \text{ g cm}^{-3}$ .
- A main region of neutron superfluid, with no viscosity, that maintains an equilibrium between neutron decay and proton-electron association. This region might rotate independently of the crust and this decoupling could then lead to an explanation for the irregularities on pulsar timing (see section 2.4.1).
- A solid region with a lower density that does not allow electrons to

penetrate the nucleus and combine with protons.

- Above the neutron ‘drip point’<sup>1</sup> ( $\rho_{dp} \sim 4 \times 10^{11} \text{ g cm}^{-3}$ ), a solid and crystalline crust approximately 1 km thick made by heavy nuclei, such as iron, covers the rest of the star.

In figure 2.1(b), a graphical representation of these layers is shown. The most accepted models which depend on the equation of state (EoS), a relation between the mean density  $\rho$  and the thermal pressure, set a NS radius in the range of 10.5 km to 11.2 km for masses between 0.5 to  $2 M_{\odot}$  and a maximum possible mass of  $3M_{\odot}$  [33].

Considering that NS are directly associated to pulsars, information from the latter can be used to study the structure and main characteristics of the former. This is based on two principles:

1. The equation of state. The understanding of the internal structure of the NS as described by the EoS will lead to a global understanding of the NS. This EoS can also be translated into a mass-radius relation. For example, as  $\rho$  approaches  $\rho_s = 2.7 \times 10^{14} \text{ g cm}^{-3}$ , the density of nuclear matter, the NS radius is mainly determined by the thermal pressure. A much more detailed analysis of this principle and a comparison of different EoS can be found at [35].
2. The relation between the centrifugal forces and the gravitational accelerations in terms of the rotational periodicity  $P$ . This rotational periodicity is known from the pulses and a relation between this periodicity

---

<sup>1</sup>This is a critical value of  $\rho$  in which the neutron chemical potential becomes positive [34].

and the lower limit for  $\rho$  of the NS can be set [36]:

$$P(\rho) > \left( \frac{3\pi}{G\rho} \right)^{1/2}, \quad (2.1)$$

as well as upper limits to physical parameters like the radius of the star

$$R = \left( \frac{GM}{4\pi^2} \right)^{1/3} P^{2/3}. \quad (2.2)$$

With these equations, and given the periodicity of the fastest known pulsar PSR J1748–2446ad of 1.40 ms [33], a mean density of around  $7.2 \times 10^{16} \text{ g cm}^{-3}$  and assuming  $M = M_{\odot}$ , an upper limit to the radius of 20.7 km is obtained. Also, equation 2.1 leads to  $\rho_s$ , a conservative lower limit of  $\rho$ , because as a consequence of an oblateness due to fast spinning, the gravitational acceleration at its equator will decrease and the centrifugal acceleration will increase.

## 2.3 Pulsars

There are two main categories of pulsars: young pulsars and old or *recycled* pulsars. The recycling process from which the latter take their name will be described later in this section.

Pulsars have been observed as isolated objects or as components of binary systems, as shown in table 2.1. These binary systems can be either a combination of two NS, a white dwarf and a NS, or a main-sequence star and a NS. Depending on the arrangements, a specific kind of electromagnetic radiation will be expected.

Based on the two most simple characteristics that can be obtained from pulsar observations, namely the rotational period  $P$  and the variation of the rota-

tional period over time  $\dot{P}$ , pulsars can be classified using a quantity named the *characteristic age*  $\tau_p$ , given by [36]

$$\tau_p \equiv \frac{P}{2\dot{P}} \quad (2.3)$$

This is the result of integrating the product  $P\dot{P}$  over time assuming that the pulsar is slowing down, that is  $P_0 \ll P$ , where  $P_0$  is the pulsating rate when the pulsar is born.

Table 2.1: Pulsar classification:  $P(\rho)$  and  $\dot{P}$  are based on equations 2.1 and 2.3, respectively.

Feature	Young	Millisecond (MSP) (recycled)
Period of rotation ( $P$ )	$10 \text{ ms} \lesssim P < P(\rho)$	$\lesssim 10 \text{ ms}$
Spin down rate ( $\dot{P}$ )	High ( $\dot{P} \sim 10^{-15} \text{ s s}^{-1}$ )	Low ( $\dot{P} \sim 10^{-20} \text{ s s}^{-1}$ )
Magnetic field ( $B$ )	$10^{12} - 10^{15} \text{ gauss}$	$10^8 - 10^9 \text{ gauss}$
Stellar arrangement	Typically isolated NS	Typically binary systems with at least one component a NS
Location within the Galaxy	Most of them in the galactic plane	Less in the galactic plane, many in globular clusters

This *spin evolution principle*, shown in the diagram of figure 2.2, classifies old millisecond pulsars (MSP) in a cluster at the bottom left, young pulsars in the big cluster in the middle, and small groupings of other types. The grey area is a region in which theoretical models do not expect to find pulsars. Also there are reference lines of constant characteristic age  $\tau_p$ , magnetic field strength  $B$  and spin-down luminosity  $\dot{E}$ . The single hatched and double hatched areas are ‘Vela-like’ with  $\tau_p \sim 10\text{--}100 \text{ kyr}$ , and ‘Crab-like’ with  $\tau_p < 10 \text{ kyr}$ , respectively.

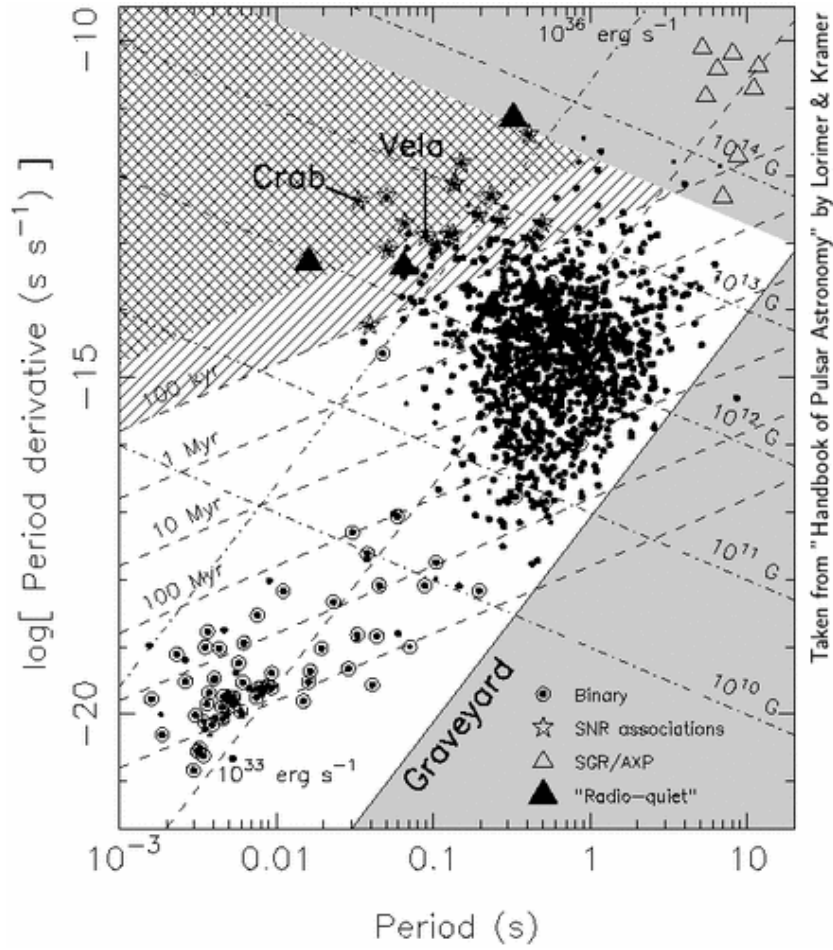


Figure 2.2: **Pulsar characteristic age ( $P\dot{P}$  diagram).** In this diagram, from [36], four main groups of pulsars can be distinguished: the central cluster of young pulsars, mainly in solid dot markers (isolated NS), the bottom left (less populated) MSP pulsar cluster, mainly circled-dot markers (binary systems), the SGR/AXP (soft-gamma repeaters/anomalous X-ray pulsars) empty triangle markers at the top left side and “radio-quiet” pulsars in filled triangle markers.

## 2.4 Neutron star transients

A very intriguing feature of pulsars is that their time of arrival (TOA), is nominally regular. As it was described in section 1.4.2, the accuracy on the arrival times of the pulses in radio pulsar observations could lead to the detection of gravitational radiation as in the case of PTA. From time to time, this TOA is not regular and opens up other ways to search for gravitational wave signals. These irregularities are separated into two main groups: *timing*

*noise* and *pulsar glitches*, and could be associated with gravitational waves emission from NS. Another transient events produced by NS and that might trigger gravitational radiation are the *Type I X-ray bursts* from NS in accreting binary systems.

This research covers an analysis over two kinds of events, each one associated to each class of pulsars, that are considered triggers of gravitational wave emissions. These events are *pulsar glitches*, from young pulsars in radio observations, and *Type I X-Ray bursts* from old recycled pulsars, like MSP. A detailed description of them is provided in the sections below, but not for timing noise. Good references for timing noise are [37] and chapter 7 in [33].

### 2.4.1 Glitches in radio pulsar observations

Pulsar glitches represent a dramatic change in the periodicity of a pulsar that, with their relatively constant shape, have been of interest to theoretical astrophysicists, radio astronomers, particle physicists and gravitational waves scientists. A pulsar glitch can be divided in two stages. The first stage is a sudden increment in the frequency of the observed pulses. This translates into a sudden increment on the pulsar rotation rate  $\Omega$ , if the lighthouse beacon model is considered. The second stage is a steady exponential recovery towards the pre-glitch pulsating rate. A simplified diagram of these two stages is shown in figure 2.3. In radio observations, radio astronomers measure the difference between  $\Omega$ , the rotation rate at the beginning of the glitch, and  $\Omega_f$ , the rotation rate just before the exponential recovery starts. This difference is more commonly referred to as  $\Delta\Omega$ . The standard notation for the magnitude of a glitch is defined by the ratio of the variation of the rotation rate during the glitch and the pre-glitch rotation rate,  $\Delta\Omega/\Omega$ .

The importance of knowing the physics behind the glitches falls into the un-

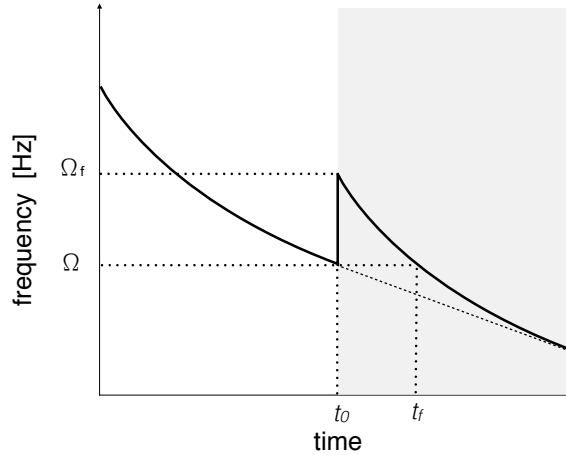


Figure 2.3: **Representation of a pulsar timing glitch.** This simple sketch represents how a pulsar glitch is seen in radio pulsar observations. The dashed line following the pre-glitch decay line shows that after the glitch, the exponential recovery brings the pulsation frequency to the pre-glitch rate. The light and dark sections separate the two main stages of the glitch.

derstanding of the internal structure of the NS, particularly the dynamics of the fluid component [38] and its interaction with the crust. There are many models that explain these interactions, such as ‘star quakes’ [39] or a pinning-unpinning process between a superfluid component and the crust [40]. In all of these models there is an agreement that a glitch is a consequence of the conservation of the angular momentum of the NS which, after the occurrence of the event that triggers the anomaly, tends to increase the spin frequency and produce the timing glitch. The variation of the spin frequency caused by a pulsar glitch is not easy to measure because they are very small, they do not occur often and also because each pulsar has different recurrent intervals. In a database created with data from [25], [26], [27] and [28], and included here in appendix A, a total of 352 glitches from 114 pulsars were analysed. From these pulsars, 12 have presented more than 5 glitches and are classified as frequent glitching pulsars.

In figure 2.4 it can be seen that these glitches occur within an interval of  $\sim 3$  years in the case of the Vela pulsar, PSR J0835–4510, or the Crab pulsar,

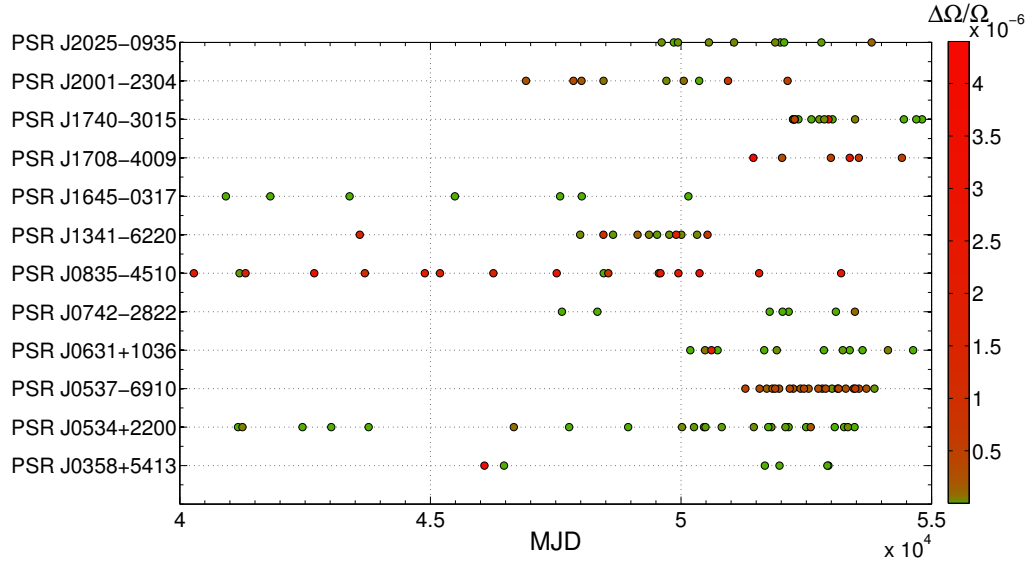


Figure 2.4: **Frequent glitching pulsars.** From a database of 114 pulsars, 12 pulsars that have produced in their observational history more than 5 glitches were selected. This plot covers a time interval of  $\sim 40$  yr. Each horizontal set of points (each point representing a glitch) corresponds to the pulsar labeled on the left vertical axis (PSR nomenclature). The horizontal axis is time in Modified Julian Days (MJD), in which the time between each minor tick is 500 days. In the case of the Vela Pulsar (PSR J0835–4510), approximately 1 or 2 glitches can be counted every 3 years.

PSR J0534+2200, which are references for the most representative glitching pulsars. Also, in figure 2.4 the strength of the variation of these glitches is presented, with green being the weakest and red the strongest. This picture shows that some pulsars glitch ‘regularly’ during the timespan shown, like the Vela pulsar, and some others produce glitches of similar intensity during a period of time and then stop, like PSR J0537–6910. From data in appendix A, the left panel of figure 2.5 shows that for most of the glitches  $\Delta\Omega/\Omega \lesssim 5 \times 10^{-6}$ , although a glitch with a value 20 times larger has been registered. The glitches considered in this database were produced by pulsars within a distance of  $\sim 50$  kpc, as shown on the right panel of figure 2.5. This plot does not necessarily mean that glitches only happen in nearby pulsars but rather that there is a limit on the reach of observations.

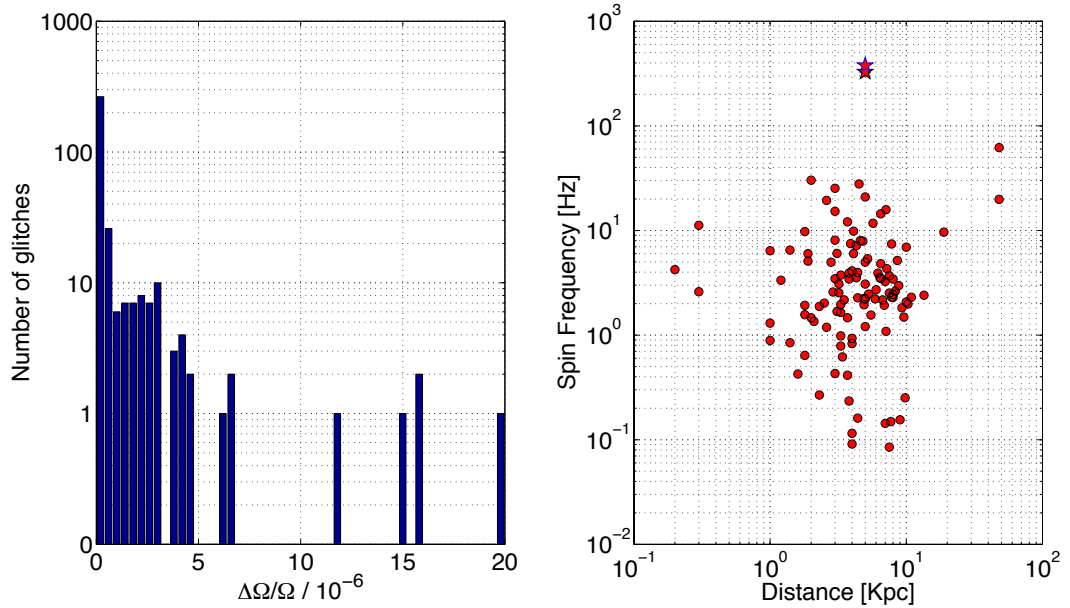


Figure 2.5: **Glitches vs distance and  $\Delta\Omega/\Omega$ .** The left panel shows the  $\Delta\Omega/\Omega$  variation of the glitches from appendix A. The most energetic glitch considered in this study is  $\sim 20$  times the average ( $\sim 10^{-6}$ ). The right panel shows the relation between the NS spin frequency and the distance to the pulsar that has produced glitches. The star markers represents the millisecond pulsar [41], [42].

### Glitches from millisecond pulsars

As mentioned before, most glitches are observed in young pulsars. Nevertheless, a ‘microglitch’ in the MSP pulsar PSR B1821–24 in the globular cluster M28 was observed [41]. The glitch had a  $\Delta\Omega/\Omega \sim 10^{-11}$ . It is interesting to mention that, given that most pulsar timing glitches happen in young pulsars, this MSP is the youngest amongst the host globular cluster, with a  $\tau_p$  of  $3 \times 10^7$  yr, and also one of the youngest amongst the Galactic field MSP. This rare glitch is the only one from a millisecond pulsar registered in the pulsar timing glitches catalogues.

During an X-ray observation of HETE J1900.1–2455, an accreting millisecond pulsar with a  $0.016 - 0.07 M_\odot$  brown dwarf companion, a small jump in the spin frequency of the star was observed: “... *detection of a dramatic brightening of the source on MJD 53,559, accompanied by a shift in the pulse*

*frequency with  $\Delta\Omega/\Omega \sim 6 \times 10^{-7}$ , and then the suppression of pulsations in subsequent observations”* [42]. Despite this description, the event was not catalogued as a glitch, which leaves PSR B1821–24 as the only glitching millisecond pulsar on the catalogues. On the right hand side panel of figure 2.5 these two objects are marked as red stars. Although it is known that there is no correlation between the spin frequency of a NS and its distance to Earth, this plot is interesting since it illustrates how the millisecond pulsars compare to the slower rotating NS.

### 2.4.2 Type I X-ray bursts

Type I X-ray bursts are explosive events that occur in binary systems in which one of the components is a NS. As shown in figure 2.2, most of the MSP are in binary systems, shown in circled-dot markers, that have a different evolutive course than the ‘regular’<sup>2</sup> one of isolated pulsars. Due to their proximity, material containing H and He is transferred from the less massive companion to the most gravitationally strong one, that generally is a NS. As a consequence of this matter transfer, the angular momentum of the accreting star increases. If these pulsars were isolated, it is believed that they would have a regular evolution, decaying in luminosity until they become unobservable, but the spinning up due to the accretion makes them radio emitters. This is where the nickname ‘recycled’ comes from. The material accretion also provides thermal energy to these stars making them X-ray sources, and are therefore called **Low Mass X-ray Binaries** (LMXBs).

During this process, the accreted material forms a very compressed and thick envelope in the surface of the NS crust, due to the strong gravitational at-

---

<sup>2</sup>This is: from its birth in a supernova until the final second, after the slowing down of the rotational period, in which radiation ceases.

Table 2.2: Type I X-ray burst classification (after Keek &amp; In t Zand, 2008 [43]).

Burst	Normal	Intermediate	Super
Duration	10 – 100 s	15 – 40 min	1 day
Energy	$10^{39}$ ergs	$10^{40} - 10^{41}$ ergs	$10^{42}$ ergs
Recurrence time	hours – days	tens of days	years
Number observed	$> 10^3$	$\sim 20$	15
Number of sources	$\sim 90$	8	10

traction of the star. In a few hours, thermal conditions for the fusion of H and He are reached due to the high densities. If the thermonuclear reaction is unstable, a fast ignition is produced burning most of the envelope at once and leading to a thermal decay of the crust [43]. This burst observed in X-ray frequencies is called Type I X-ray burst and could be used to probe the thermal properties of the crust. In table 2.2, extracted from [43], the three main types of these bursts can be seen. The selection criteria of these sources is described in chapter 3.

### 2.4.3 Summary

With these two kinds of transient events produced by NS, the study of one emission per group of pulsars is considered. That is, the *pulsar glitches* mainly associated with young pulsars, and *Type I X-ray bursts* associated with accreting and old NS in binary systems. The analyses of these sources are discussed in chapters 3, 4 and 5.

## 2.5 Quasi-normal mode oscillations in neutron stars

In compact stellar objects, such as a NS, General Relativity plays a role in the interpretation of oscillations within these objects. Perturbations caused by these objects (either electromagnetic or gravitational) are called *quasi-normal modes* (QNM) [44] and can be associated with gravitational wave emissions. They differ from the classical normal modes in their complex nature, in which the real part carries information about the oscillation frequency and the imaginary component contains the damping part. There are many kinds of QNM depending on the interaction that participates in their damping [44] :

- *g-modes*, which are restored by the buoyancy within the fluid interior of the NS in which the gradient of pressure is very small.
- *f-modes* or fundamental modes are non-radial oscillations only that tend to grow towards the surface of the NS. Their frequency is proportional to the mean density of the star.
- *p-modes*, in which pressure participates in the restoring mechanism in both radial and non-radial directions. The frequencies depend on the travel time of an acoustic wave across the star, typically higher than 4 – 7 kHz.
- *w-modes*, of which the standard version called “curvature modes” are the ones related with the space-time curvature and exist for all relativistic stars. The damping time is inversely proportional to the compactness of the star and the frequencies are of the order of 5 – 12 kHz.

- *r-modes*<sup>3</sup>, or rotational modes, are purely axial inertial modes which restoring force is the Coriolis force. See section 2.6.2.

As was said, the interest in understanding these modes is based on the fact that they could be associated with gravitational radiation, and from them learn about the physical mechanisms that happen in relativistic stars. Unfortunately, some of them like *g-modes*, once they emit gravitational radiation, stop oscillating and no further analysis can be done.

In this thesis, NS are considered as spheres that can be described by the Laplace equation in spherical coordinates  $(r, \theta, \psi)$ . The angular dependant solution of this equation is given by

$$Y_l^m(\theta, \psi) = N_l^m P_l^m(\cos \theta) e^{im\psi}, \quad (2.4)$$

in which  $\theta$  and  $\psi$  describe the latitude and longitude coordinates of the NS, respectively;  $Y_l^m$  are called the spherical harmonics of degree  $l$  and order  $m$ ,  $P_l^m$  is the associated Legendre polynomial and  $N_l^m$  is a normalisation constant given by

$$N_l^m = \sqrt{\frac{(2l+1)(l-m!)}{4\pi(l+m!)}}. \quad (2.5)$$

To get a better idea of what the spherical harmonics mean it is worth remembering that the Laplace equation is a harmonic function which describes potentials. So, in the context of QNM in which the restoring mechanisms are related to gravitational interactions, like *r-modes*, these harmonics describe how the gravitational potential behaves, and within the NS, the indices  $(l, m)$  define the boundaries of gravitational potential differentiation in the star.

---

<sup>3</sup>The name comes from their similarity to *Rossby waves* in the Earth's oceans. The motion of these waves is also ruled by the Coriolis force. They are responsible of climate exchange between latitudes due to current oscillations such as the Gulf stream.

## 2.6 Neutron star instabilities

Until now, a description of the structure of the NS as well as the physics behind some events observed in these stars that could be associated with gravitational radiation, has been made. In order to link all these descriptions with the analysis presented in this thesis, it is important to define the relation between these events and gravitational wave emission.

This link is strongly related with instabilities that happen in the inner layers of the NS that are associated with QNM. Some of these instabilities are driven by gravitational radiation. In 1970, Chandrasekhar [45] noted that the emission of gravitational radiation causes the amplitude of some QNM to grow. This mechanism, further studied by Friedman and Schutz [46] and called the *CFS mechanism*, is useful to describe other instabilities directly associated with QNM, such as the *r-mode* instability. As an important reference to understanding these instabilities, the description of the CFS mechanism is presented followed by the description of the *r-mode* instability, which is the main NS instability considered in this work.

### 2.6.1 Chandrasekhar-Friedman-Schutz mechanism

The space-time is used as a medium in which gravitational radiation propagates once it has been triggered by some of the mechanisms in, for example, an oscillating star. One of the mechanisms that explains the instabilities in rotating stars is the Chandrasekhar-Friedman-Schutz (CFS) mechanism, described first by Chandrasekhar and generalised by Friedman and Schutz.

To get a preliminary idea of the problem it is worth understanding it first from the perspective of a non-rotating star of angular momentum  $J_s = 0$ , with fluid internal layers just like a NS. A QNM oscillation in this star would generate certain patterns of motion, or perturbations, with some magnitude

$M_{p+}$  which move at some characteristic angular velocity  $\omega_{p+}$ . The ‘+’ sign refers to a ‘positive’ direction, which for convenience will be anti-clockwise.

This perturbation will increase the angular momentum of the entire star making  $J_{p+} > 0$ . Then, due to the perturbation triggered by the oscillation mode, there is an emission of gravitational radiation that carries some angular momentum of the star, decreasing  $J_{p+}$  and in consequence decreasing  $M_{p+}$ . By symmetry, there must exist a perturbation identical to the first one but moving in a ‘negative’ direction, clockwise following the convention, with  $J_{p-} < 0$ . This will be affected by the emission of gravitational waves carrying negative angular momentum and decreasing its magnitude. In this non-rotating context, no instability seems to be present in the system.

In the case of a rotating star the sign of the angular momentum carried by gravitational radiation will be related **only** with the sign of the total star’s angular momentum  $J_s$ , which following the convention will be set as ‘positive’ and anti-clockwise. From the point of view of an observer outside the star, while the spinning frequency of the star  $f_{\text{star}}$  increases, the angular momentum  $J_s$  will increase and so will the angular momentum  $J_{p+}$  of the perturbation moving in the same direction. At the same time, the opposite and ‘negative’ perturbation with angular momentum  $J_{p-}$ , instead of increasing will reduce its magnitude until, if the star rotates fast enough, it will become static. If the star rotates even faster,  $J_{p-}$  will become ‘positive’ and radiate positive angular momentum  $J'_{p+}$ . This  $J'_{p+}$  will be subtracted from  $J_{p-}$ , and hence will increase  $J_{p+}$  and so  $M_{p+}$ .

When the perturbation is sufficiently large, it will radiate angular momentum and the mode will grow. In other words, if the star is sufficiently fast, so that  $J_{p+}$  increases, it will be unstable due to a gravitational radiation reaction (*GRR*). However, in a more real context, due to the viscosity of the interior

layers of the NS, some dissipation processes will take place there, and a balance between these processes and the *GRR* will rule the emission of gravitational waves.

### 2.6.2 *r*-modes in neutron stars

As mentioned above, some mechanisms that are useful to explain astrophysical events like pulsar glitches [47] lead to gravitational radiation from the NS and are related with QNM [48]. In 1998 Andersson [49] demonstrated that *r*-modes can be unstable due to the emission of gravitational waves even from the slowest relativistic rotating stars. Andersson also showed that this instability is well explained by the CFS mechanism. If an oscillation mode  $\sigma_r$  exists in a non-rotating star, an oscillation mode  $-\bar{\sigma}_r$  will exist, where the bar means the complex conjugate. For this non-rotating star a symmetry between these perturbations exists. When the star rotates, this symmetry is broken which has some repercussions on the damping rates of the mode. For retrograde modes, the rotation decreases the damping rate to a more stable mode, while for prograde modes this rate increases which refers to a more unstable state. Each mode  $\sigma_r$  will be split in  $2l + 1$  modes, each corresponding to a value of  $m$ , where  $l$  and  $m$  refer to the spherical harmonics' degree and order, respectively, as discussed in section 2.5.

The gravitational radiation associated with the *r*-modes instability is related to current quadrupoles rather than mass quadrupoles (a more detailed explanation of this is provided in section 3.2.1). The current quadrupole  $l = 2$  has a stronger contribution to gravitational wave emission than the higher current multipoles  $l > 2$  by factors of the order of the rotation frequency of the star  $f_{\text{star}}$  [44]. For a given  $l$ , the strongest contribution to the mode function has  $l = m$ .

The relation of these harmonics with the amplitude and the frequency of a gravitational wave emission will be described in detail while describing the waveform associated with  $r$ -modes in sections 3.2.1 and 3.2.2.

# Chapter 3

## Gravitational wave emission and signal attributes

In this chapter, the mechanism by which a NS transient can lead to gravitational wave emission is presented. Firstly, the effects of the orientation of a pulsar with respect to the Earth are described. This is followed by a discussion of the gravitational wave signal parameters. Particularly, for the construction of the characteristic time of the signal which is ruled by the balance between the gravitational radiation reaction (*GRR*) and energy dissipation, a model proposed by Levin & Ushomirsky [50] is considered. This model assumes the existence of a viscous boundary layer in the crust-core interface of the NS. Then, the relation between the energy and the amplitude of the gravitational wave is calculated in two ways: assuming the Levin & Ushomirsky model, and with the introduction of a parameter  $\beta$  that modulates the energy transferred from the glitch to the gravitational wave. A detectability parameter  $h_{\text{rss}}$  is defined together with a series of numerical estimates for it. After this, a reinterpretation of the Levin & Ushomirsky model that focuses on Type I X-Ray Bursts is presented. The reason for this reinterpretation is that implementing the original Levin & Ushomirsky model to these type of emissions resulted in

some of the sources being in an unstable regime. This new approach addresses this issue. Finally, numerical estimates for both pulsar glitches and Type I X-Ray Bursts are presented considering both the unmodified and modified Levin & Ushomirsky models.

In this chapter it is shown that it is unlikely that the energy released by glitches or Type I X-Ray Bursts can reach the sensitivity of current gravitational wave detectors. As a result, the feasibility of detection is oriented to future detectors like Advanced LIGO and Advanced VIRGO or ET. Part of this detectability study has been published in [51]. The theoretical calculations were done in collaboration with Dr. D. Ian Jones and the other co-authors of the publication. The remainder of this chapter was done by the author based on this theoretical work.

### 3.1 Pulsar beam orientation

As in many magnetised and rotating objects in the universe, including the Sun and the Earth, the NS rotation axis  $\vec{\Omega}$  and the corresponding magnetic field axis are not always aligned. The detectability of a pulsar's electromagnetic emission is strongly related to the orientation of these axes. The amount of electromagnetic energy that is received from the star depends on the magnetic inclination angle  $\alpha_p$ , between the pulsar beam (that coincides with the magnetic dipole) and the line of sight from the Earth, as illustrated in figure 3.1. Particularly, the dipole's radiation power  $\dot{E}_{\text{dipole}}$  in terms of  $\alpha_p$  [36] is expressed as

$$\dot{E}_{\text{dipole}} = \frac{2}{3c^3} |\mathbf{m}|^2 \Omega^4 \sin^2 \alpha_p \quad (3.1)$$

where  $\mathbf{m}$  is the magnetic dipole's moment,  $\Omega$  is the rotation rate of the NS, and  $c$  is the speed of light. The magnetic inclination angle  $\alpha_p$  is also related to

the *inclination angle*  $\iota$  because the latter is parallel to the rotational axis  $\vec{\Omega}$ . Then, if the light-house beacon model is considered, the angle  $\iota$  is enough to describe these orientations, as shown in figure 3.1. The angle  $\iota$  also changes the amplitude of the gravitational wave observed at the gravitational wave detector. This is because the gravitational wave amplitude is changed by a factor of  $\cos(\iota)$ .

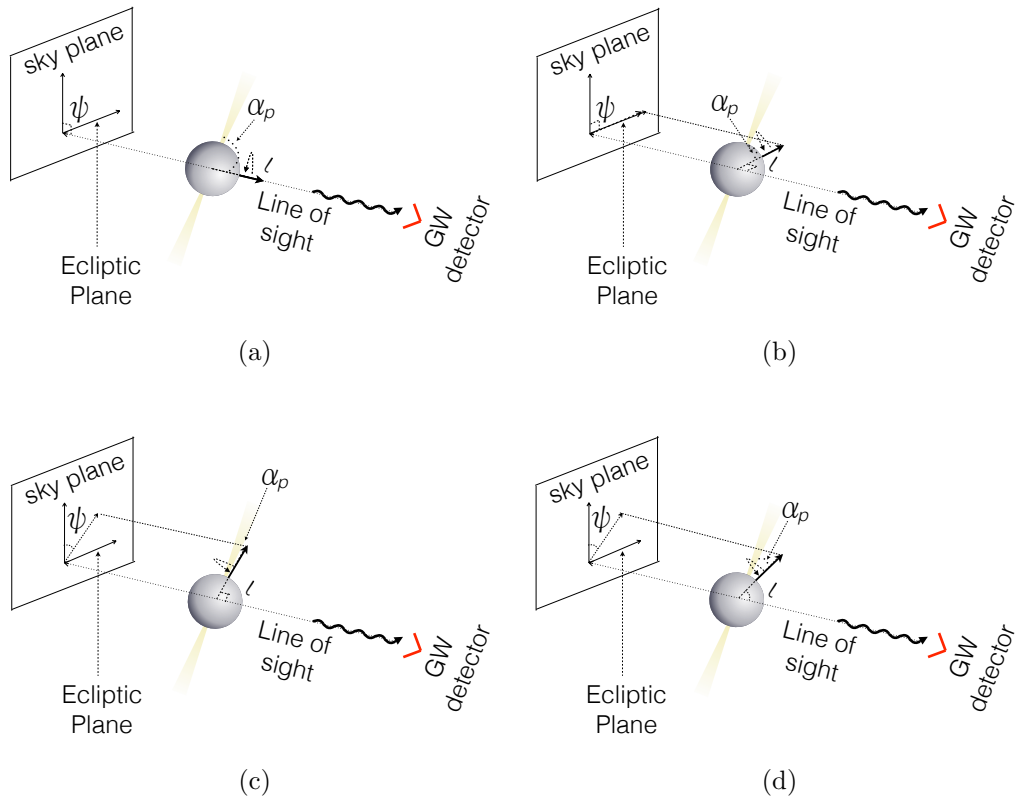


Figure 3.1: **Graphical representation of the inclination angle  $\iota$  and the polarisation angle  $\psi$  of a NS.** Four different combinations of these angles are shown: (a)  $\iota = 0^\circ$ ,  $\psi = 0^\circ$ ; (b)  $\iota = 90^\circ$ ,  $\psi = 90^\circ$ ; (c)  $\iota = 90^\circ$ ,  $\psi = 45^\circ$  and (d)  $\iota = 45^\circ$ ,  $\psi = 45^\circ$ .

Another orientation parameter that is considered in gravitational wave detection from pulsars is the polarisation angle  $\psi$ . This is the angle of the projection of  $\vec{\Omega}$  over the sky plane with respect to the same observer frame as determined by the orientation of the gravitational wave detector. In figure 3.1 a graphical representation of different configurations of these two orientation parameters

with respect to the NS and a gravitational wave detector, is presented. For instance, panel 3.1(a), shows the maximum contribution value of the angle  $\iota$  because it is parallel to the line of sight. This corresponds to a value for  $\psi$  of zero degrees. Panel 3.1(b), shows the case for a rotation axis perpendicular to the line of sight where  $\psi = 90^\circ$ .

## 3.2 The $r$ -modes waveform

Assuming an excited NS that oscillates with a particular period, this study considers that the  $r$ -mode gravitational wave signal takes the form of a sine wave with an exponential envelope, also known as *ringdown*. The decay of this periodical function is ruled by a factor  $\tau$ , which is defined as the time that is needed for the amplitude of the signal to be half of the initial amplitude. In the context of the  $r$ -mode emissions, the waveform frequency would be the same as the mode frequency in the rotational frame  $f_{\text{rot}}^{\text{mode}}$  and the value of  $\tau$  would depend on the gravitational radiation reaction  $GRR$  and dissipation processes. In this section, a description of the amplitude, the frequency and the characteristic time of the exponential decay is presented.

### 3.2.1 Amplitude of the waveform

Following [52], assuming that the gravitational wave emission is caused by the mass quadrupole motion in a slowly-rotating NS, with a Newtonian fluid interior and with spherical harmonics  $l = m = 2$ , the corresponding waveform equations for the two gravitational wave polarisations are

$$h_+^{22} = h_{22} A_+^{22} \sin(\omega t) e^{-t/\tau}, \quad (3.2)$$

$$h_\times^{22} = h_{22} A_\times^{22} \cos(\omega t) e^{-t/\tau}, \quad (3.3)$$

in which  $A_{\times}^{22} = 1 + \cos^2 \iota$  and  $A_{+}^{22} = 2 \cos \iota$ , with  $\omega$  the mode frequency. As described in section 2.6.2, the  $r$ -modes oscillations are dominated by the current quadrupole emission. According to [53], the difference in the radiation patterns between the mass quadrupole and the current quadrupole is the transformation of the polarisation angle  $\psi \rightarrow \psi + \pi/4$  which is equivalent, in terms of gravitational wave amplitudes, to  $h_{+} \rightarrow -h_{\times}$  and  $h_{\times} \rightarrow h_{+}$ , respectively, for each polarisation.

This relation leads to the  $r$ -modes waveform equations

$$h_{+}^{22} = -h_{22}A_{\times}^{22} \sin(\omega t)e^{-t/\tau}, \quad (3.4)$$

$$h_{\times}^{22} = h_{22}A_{+}^{22} \cos(\omega t)e^{-t/\tau}. \quad (3.5)$$

### 3.2.2 Frequency of the waveform

According to simple models of the theory of rotating fluids, the frequency of inertial modes, of which the  $r$ -modes are a subclass, lies in an interval up to four times the rotational frequency of the star [54]. These frequencies are also proportional to the angular velocity of the star because they appear as co-rotating with the star to a distant inertial observer. The  $r$ -modes in a rotating star have a frequency in the rotating frame of [44]

$$f_{\text{rot}}^{\text{mode}} = \frac{2mf_{\text{star}}}{l(l+1)}, \quad (3.6)$$

which, for the inertial observer will be

$$f_{\text{inertial}}^{\text{mode}} = f_{\text{rot}}^{\text{mode}} - mf_{\text{star}}. \quad (3.7)$$

For a ‘perfect fluid star’ in the inertial frame and setting  $l=m=2$  in equation 3.7, the mode frequency is

$$|f_{\text{inertial}}^{\text{mode}}| = \frac{4}{3}f_{\text{star}}, \quad (3.8)$$

and the  $r$ -mode frequency  $\omega$ , in a slowly-rotating Newtonian perfect fluid star, is defined as

$$\omega = 2\pi f_{\text{inertial}}^{\text{mode}}. \quad (3.9)$$

The relation between the  $f_{\text{star}}$  and the  $f_{\text{inertial}}^{\text{mode}}$  in equation 3.7 is subject to many corrections such as relativistic effects [55], which modify it by a fractional amount proportional to the stiffness of the star, or rotation [56], with an effect proportional to  $\Omega^2/\pi G\rho_{\text{avg}}$ , with  $\rho_{\text{avg}}$  the average density in the fluid component of the NS. Because of such factors, it is believed that the actual frequency of the mode is known to an accuracy of around 20% [57]. The uncertainty on the relation of the  $r$ -mode frequency and the spin frequency of the star becomes important when a gravitational wave target search is performed since they will define the length of the frequency search band. The length of this frequency band has implications on the computation time required to perform the analysis.

### 3.2.3 Characteristic time

The characteristic time of the waveform is of particular importance in this study since it is the component that gives the signal its long-transient nature. Since in this analysis an integration over time of the signal amplitude is done, the length of the signal will be useful to enhance its detectability.

The timescale in which the  $r$ -mode oscillation evolves is given by a balance of driving effects and damping effects [58], as mentioned at the end of section

2.6.1. The main driving effect is due to the  $GRR$ , while damping processes are mainly due to the internal viscosity of the NS. In general, this timescale can be expressed as in [59] as

$$\frac{1}{\tau} = \frac{1}{\tau_{\text{GRR}}} + \frac{1}{\tau_{\text{dissipation}}}. \quad (3.10)$$

Here, the gravitational radiation reaction timescale  $\tau_{\text{GRR}}$  is given as a function of the mode frequency  $\omega$  [58],

$$\frac{1}{\tau_{\text{GRR}}} = -\frac{32\pi G}{15^2 c^7} \omega^6 \tilde{J} M R^4, \quad (3.11)$$

in which the mode oscillation amplitude tends to grow. Also,  $M$  and  $R$  are the mass and the radius of the NS respectively,  $G$  the gravitational constant,  $c$  the speed of light and  $\tilde{J}$  is a dimensionless number depending on the stiffness of the star defined in [60] as

$$\tilde{J} = \frac{1}{M R^4} \int_0^R \rho_{\text{avg}} r^6 dr. \quad (3.12)$$

For values of  $M = 1.4M_{\odot}$  and  $R = 12.5$  km,  $\tilde{J}$  is of the order of  $\sim 10^{-2}$ .

To have an estimate of the value of  $\tau_{\text{GRR}}$ , equation 3.11 is expressed in terms of  $f_{\text{star}} = 100$  Hz, which gives

$$\tau_{\text{GRR}} = -2.47 \times 10^7 \text{s} \left( \frac{100 \text{Hz}}{f_{\text{star}}} \right)^6 \frac{1}{M_{1.4} R_{11.7}^4}. \quad (3.13)$$

The timescale associated with dissipation processes,  $\tau_{\text{dissipation}}$ , is a sum of many contributions such as NS internal viscous layers, bulk viscosity, magnetic boundary layers and mutual friction. A model that might give an explanation for this timescale is the one proposed by Levin and Ushomirsky [50] in 2001. They proposed that the energy dissipation is due to the existence of a *viscous*

*boundary layer* between the crust and the core in a NS. This effect has a characteristic damping time  $\tau_{vbl}$  given by

$$\frac{1}{\tau_{vbl}} \simeq 0.01 s^{-1} \frac{R_6^2 F^{1/2}}{M_{1.4} T_8} \frac{\rho_b}{\rho} \left( \frac{f_{\text{star}}}{\text{kHz}} \right)^{1/2} \left( \frac{\delta u}{u} \right)^2. \quad (3.14)$$

Equation 3.14, considers an internal temperature of  $10^8$  K in a NS with a radius  $R_6 = 11.7 \times 10^6$  cm, a mass  $M_{1.4}$  of  $1.4M_\odot$ , a density  $\rho$  at the crust-core interface, an estimate of this density  $\rho_b = 1.5 \times 10^{14}$  g cm $^{-3}$  at the base of the crust and a NS spin frequency  $f_{\text{star}}$  in units of kHz. Also, there are two parameters that need to be described in detail. The first parameter is  $F$ , a fitting parameter for the shear viscosity that takes different values depending on the superfluidity of the layer. If the viscosity is mediated by neutron-neutron scattering,  $F = (\rho/\rho_b)^{5/4}$ ; if it is mediated by electron-proton scattering,  $F = 1/15$  and if the predominant scatters are electrons,  $F = 5(\rho/\rho_b)$  [61]. The other parameter is  $\delta u/u$ , which is the fractional velocity mismatch between the crust and the core. For slow rotating NS, that rotate at frequencies much less than the Keplerian frequency  $\Omega_k^1$ ,  $\delta u/u$  takes the value of unity, taking a not relevant role in the timescale. With rapid rotating stars where  $\Omega > 0.1\Omega_k$ , this slippage parameter could take values within an interval of [ $\sim 0.06 - 1$ ], as shown in figure 3.2. This assumption considers a thin-crust model in which  $r_c/R = 0.9$  where  $r_c$  and  $R$  are the thickness of the NS crust and the NS radius, respectively, as shown in figure 3.2.

The value of  $\delta u/u$  that depends on the  $f_{\text{star}}$  is also strongly related to the spin frequency at which a star will be stable. This stability is ruled by the duration of the total timescale  $\tau$  of the mode in equation 3.10, that has to be  $> 0$  in

---

<sup>1</sup>Keplerian rotational frequency is the condition of balance between a centrifugal force and the Newtonian gravity; the maximum (cyclic) frequency at which the star can rotate without breaking up. Its value lies in the range of  $2\pi(1000 - 2000)$  Hz.

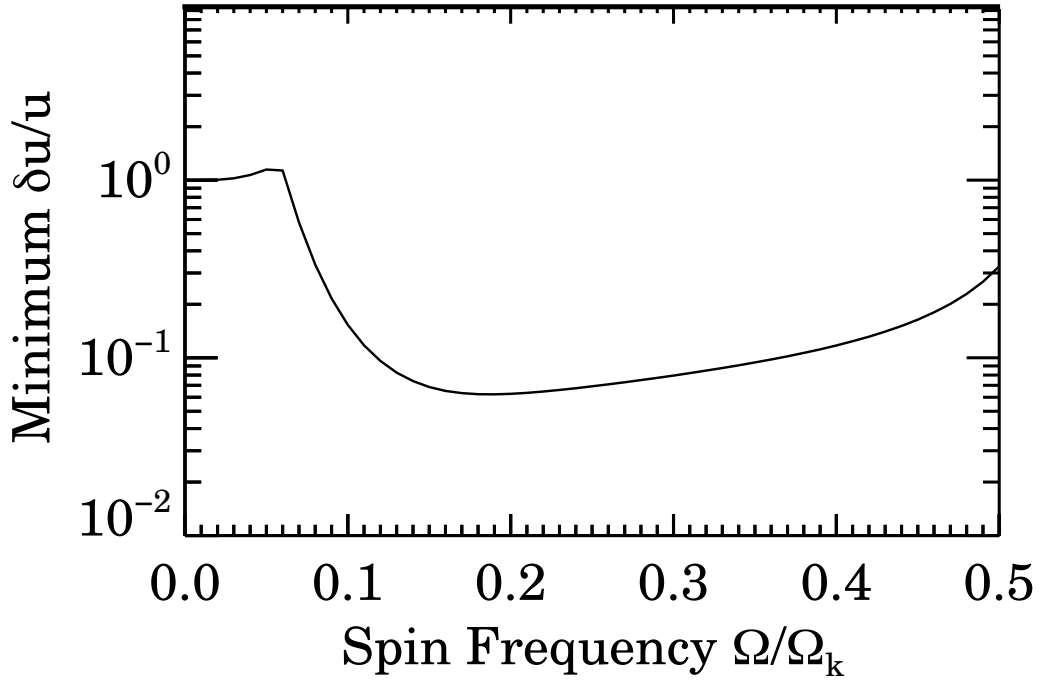


Figure 3.2: **Core-Crust mismatch velocity parameter  $\delta u/u$  according to Levin and Ushomirsky.** This plot, extracted from figure 1 in [50], shows the variation of the slippage parameter  $\delta u/u$  of equation 3.14 for a thin crust model of  $\sim 10\%$  of the NS radius. For slow rotating stars this mismatch has practically no contribution to the damping timescale, as opposed to faster spinning stars in which the timescale tends to increase.

order for the mode to be stable. This means that the contribution of the dissipation processes to the total timescale will be smaller than the contribution of the  $GRR$  timescale. The critical spin frequency in which the star is balanced between the  $GRR$  driven growth timescale and the timescales due to dissipation processes is denoted as  $f_{\text{critical}}$ . This frequency is a function of many factors such as  $\delta u/u$  and temperature, and hence  $f_{\text{critical}} = f_{\text{critical}}(T, \delta u/u\dots)$ . This means that the optimal value of the frequency can be chosen based on these parameters (tuning). Firstly, the tuning with respect to the  $\delta u/u$  parameter is presented, and later a tuning of the critical spin frequency based on temperature will be discussed.

$f_{\text{critical}}$  **tuning with respect to**  $\delta u/u$ 

The tuning of this frequency based on  $\delta u/u$  is plausible with the Levin & Ushomirsky model dissipation timescale shown in equation 3.14. This frequency also leads to a relation between the dissipation timescale and the  $GRR$  timescale given by

$$\tau(f_{\text{critical}}) = 0 \Rightarrow \tau_{\text{dissipation}}(f_{\text{critical}}) = |\tau_{\text{GRR}}(f_{\text{critical}})| \quad (3.15)$$

In this context, three different regimes can be distinguished:

1. For slowly spinning stars, so that  $f_{\text{star}}$  is significantly less than  $f_{\text{critical}}$ ,

$$\tau_{\text{dissipation}} \ll |\tau_{\text{GRR}}| \Rightarrow \tau \approx \tau_{\text{dissipation}} \quad (3.16)$$

All of the young glitching pulsars and some MSP are in this regime. This region corresponds to the left non-shaded region in figure 3.3.

2. For more rapidly spinning stars with spin frequencies just below  $f_{\text{critical}}$ , there will be a near cancellation between  $\tau_{\text{dissipation}}$  and  $|\tau_{\text{GRR}}|$ , leaving a long (positive) decay time  $\tau$ . This has the nice feature that it can lead to significant GW emissions that decay on longer timescales. This possibility, shown as the red-shaded region in figure 3.3, could be considered for the glitching millisecond pulsar (section 2.4.1).
3. For stars with  $f_{\text{star}} > f_{\text{critical}}$ ,  $\tau < 0$ , (right dark-shaded region in figure 3.3) the mode is CFS unstable and grows in time. No NS has been observed to be CFS-unstable, so this last scenario is not under consideration.

In the regime when  $\tau_{\text{dissipation}} \ll |\tau_{\text{GRR}}| \Rightarrow \tau \approx \tau_{\text{dissipation}}$ , one can approximate  $\tau_{\text{dissipation}} = \tau_{\text{vbl}}$  and get:

$$\frac{\tau_{\text{vbl}}}{\tau_{\text{GRR}}} \approx k \frac{T_8}{F^{1/2}} f_{\text{star}}^{11/2} \left( \frac{\delta u}{u} \right)^{-2} M_{1.4}^2 R_{11.7}^2, \quad (3.17)$$

Note the very steep scaling of  $f_{\text{star}}$ .

The balance between  $\tau_{\text{dissipation}}$  and  $\tau_{\text{GRR}}$ , in the second regime, is modulated by  $\delta u/u$ . The interval from which  $f_{\text{critical}}$  takes values depends on the  $\delta u/u$  interval, leading to  $f_{\text{critical}}$  between 300 Hz and 820 Hz, as shown in figure 3.3.

These values are useful to associate a timescale due to dissipation to a specific value of  $f_{\text{star}}$ . An example of this approximation is provided below:

Consider the fastest spinning pulsar observed, PSR J1748–2446ad, that has a

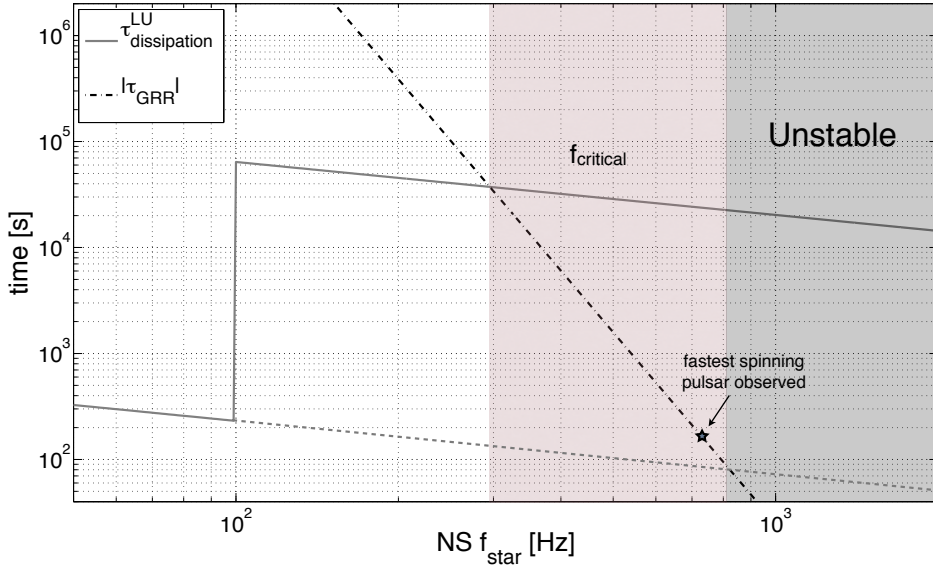


Figure 3.3:  **$r$ -mode timescales.** The relation between growing timescales and damping timescales for the mode is shown. The dissipation timescale  $\tau_{\text{dissipation}}^{\text{LU}}$  was calculated assuming the viscous boundary layer model (solid line in the plot), in equation 3.14. In this case, a ‘slippage’ parameter  $\delta u/u$  takes a value of 1 for  $f_{\text{star}} < 100$  Hz and 0.06 otherwise. This explains the step in the solid line in this plot. This also sets an interval in which the slippage parameter could take its values, as well as an interval of  $f_{\text{star}}$  in which  $f_{\text{critical}}$  can be set. Within this interval, the fastest spinning pulsar observed, PSR J1748–2446ad, with a  $f_{\text{star}} = 716$  Hz is shown as a reference. In the dark shaded frequency range, no pulsar has been observed.

$f_{\text{star}} = 716$  Hz. According to the Levin and Ushomirsky model, this frequency lies in the allowed interval for  $f_{\text{critical}}$ . An estimation of  $\tau_{\text{dissipation}}^{\text{LU}}$  using 10 different values of  $\delta u/u$  within an interval of [0.1 - 1] with a step of 0.1 is shown in figure 3.4. These estimations are shown in comparison with the  $\tau_{\text{GRR}}$  curve. The intersection of each of these estimations with the  $\tau_{\text{GRR}}$  curve defines the  $f_{\text{critical}}$  associated to that particular value of  $\delta u/u$ . In the case of PSR J1748–2446ad, the value of  $\delta u/u$  that is associated with the case where  $f_{\text{star}} = f_{\text{critical}}$  lies between [0.6 - 0.7]. A fine tuning of the  $\delta u/u$  parameter is shown in figure 3.5 with the interval of  $\delta u/u = [0.681 - 0.69]$ , revealing a more precise value of  $\delta u/u \sim 0.685$  for an  $f_{\text{critical}} = 716$  Hz. The value of the timescale due to viscosity dissipation associated with this  $f_{\text{critical}}$  assuming the Levin and Ushomirsky model  $\tau_{LU}^{\delta u/u} \approx 184$  s. In order for the star to be stable, the total timescale  $\tau < \tau_{LU}^{\delta u/u}$  as described above in the second timescale regime, and in consequence a  $\delta u/u > 0.685$  has to be considered.

### 3.3 Gravitational wave energy and detection statistic

As described in section 1.4, in order to detect gravitational waves, a mechanical displacement between the test masses at the detectors has to be registered. These displacements are proportional to the amount of energy that a gravitational wave signal carries and also depend on the features of the detected signal. In this section, the description of the equations that model the gravitational wave energy carried by the  $r$ -mode signal are presented. Also, the equation used to measure the gravitational wave energy and the corresponding displacements at the interferometer is derived.

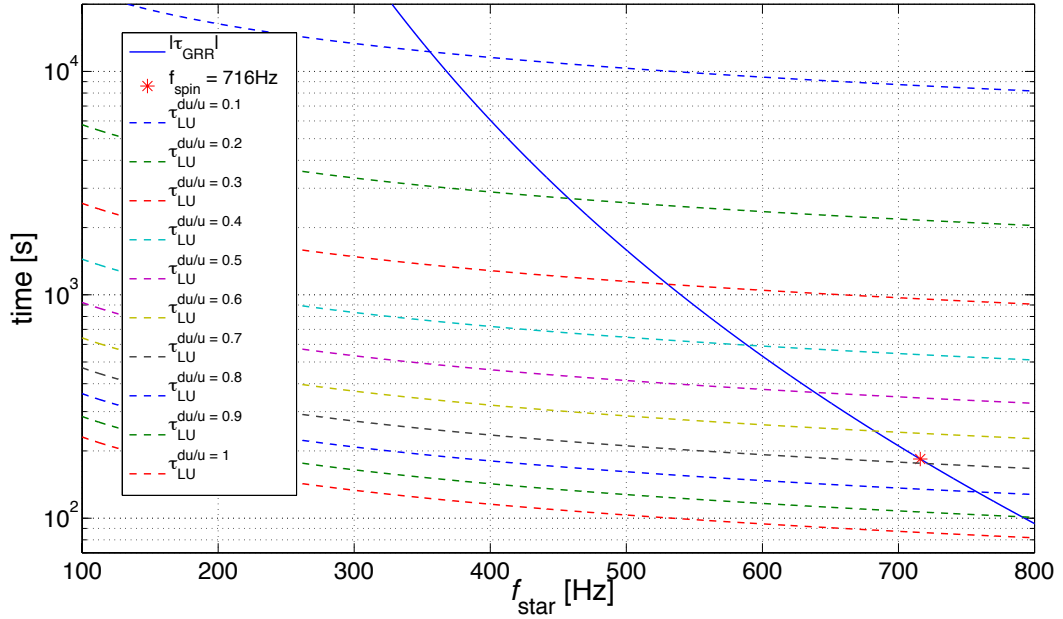


Figure 3.4:  $\delta u/u$  tuning with respect to  $f_{\text{star}}$ . In this figure, a series of estimations of  $\tau_{LU}^{\delta u/u}$  are presented, in comparison to the estimation of  $\tau_{\text{GRR}}$ . A first approximation shows that, for the case of the fastest spinning pulsar, PSR J1748–2446ad, the  $f_{\text{critical}}$  is associated with a  $\delta u/u \sim 0.7$ .

The total emission of the signal, considering the two gravitational wave polarisations shown in equations 3.4 and 3.5, is given in [62] as

$$h_0 := \sqrt{\frac{1}{\tau} \int_{-\infty}^{\infty} (h_+^2(t) + h_\times^2(t)) dt}. \quad (3.18)$$

The gravitational wave luminosity is related to the waveform amplitude in equation 3.18 and, by integrating the gravitational wave flux over a sphere of radius  $r$ , with  $r$  the distance from the source to the Earth,

$$\frac{dE_{\text{GW}}}{dt} = \frac{c^3}{G} \frac{1}{10} r^2 \omega^2 (h_0 e^{-t/\tau})^2, \quad (3.19)$$

which, as well as the waveform, will decay with time. Also, the total energy emitted can be obtained by the integration of equation 3.19 over a time interval

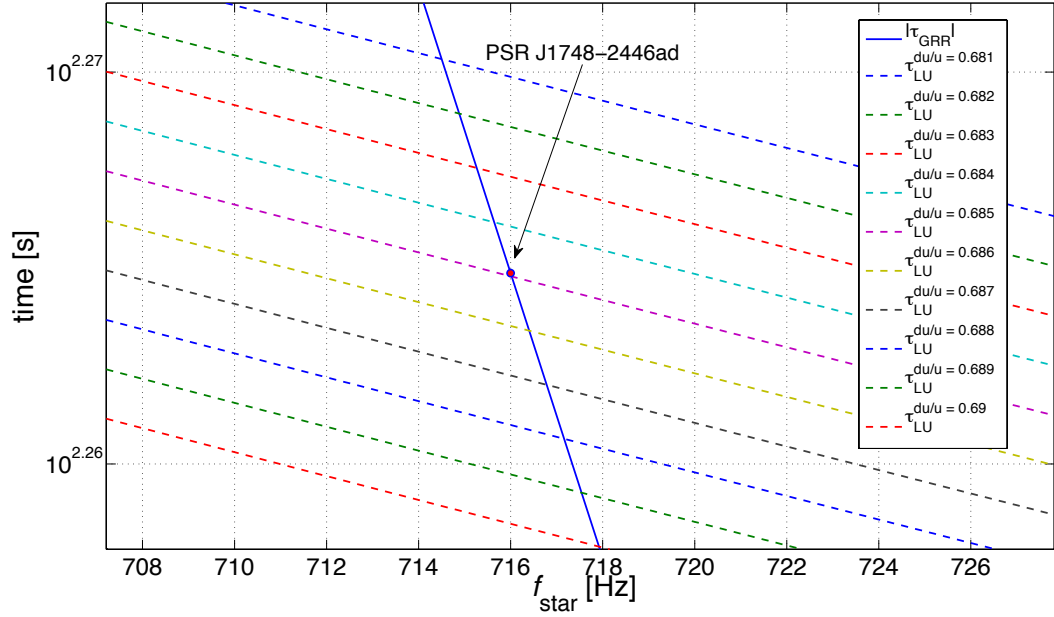


Figure 3.5: **Zoom in to  $\delta u/u$  tuning with respect to  $f_{\text{star}}$ .** A more detailed approximation to figure 3.4 shows that the  $f_{\text{critical}}$  for this pulsar is associated to a  $\delta u/u \sim 0.685$ , which corresponds to a  $\tau_{LU}^{\delta u/u} \approx 184$  s.

$0 < t < \infty$ , giving

$$\Delta E_{\text{GW}} = \frac{c^3}{G} \frac{1}{20} r^2 \omega^2 h_0^2 \tau. \quad (3.20)$$

In 1998, Lindblom et al [60] introduced an arbitrary constant  $\alpha$  to parametrise the amplitude of the  $r$ -modes. With this parametrisation, the relation between the amplitude and energy of the mode in terms of  $\alpha$  are

$$h_0(\alpha) = \sqrt{\frac{8\pi}{5}} \frac{G}{c^5} \alpha \omega^3 M R^3 \tilde{J} \quad (3.21)$$

and

$$E_{\text{mode}} = \frac{1}{2} \alpha^2 \Omega^2 M R^2 \tilde{J}. \quad (3.22)$$

A useful parameter for an arbitrary waveform that involves the total initial amplitude of an emission and its duration is the  $h_{\text{RSS}}$ , *root sum square* [63],

inferred from equation 3.18 as

$$h_{\text{rss}} = h_0 \sqrt{\tau}. \quad (3.23)$$

With equations 3.20 and 3.23, the detectability estimate at the gravitational wave detector of the waveform is defined as

$$h_{\text{rss}} = \frac{1}{r} \left[ \frac{20G}{c^3} \frac{\Delta E_{\text{GW}}}{\omega^2} \right]^{1/2} \quad (3.24)$$

which is valid for any damped oscillation mode at its corresponding frequency. Particularly, for the  $r$ -modes, where  $\omega = 4/3 \Omega$ , equation 3.24 takes the form

$$h_{\text{rss}} = \frac{1}{r} \left[ \frac{45G}{4c^3} \frac{\Delta E_{\text{GW}}}{\Omega^2} \right]^{1/2} \quad (3.25)$$

This is the relation between the detectability parameter  $h_{\text{rss}}$  at the detector and the total energy carried by a gravitational wave. This equation is useful to associate the theoretical models from which the  $r$ -mode signal is based on to a gravitational wave signal detection.

### 3.4 Gravitational wave energy modulation

A convenient way to understand the astrophysics of the events that trigger the gravitational wave emissions is through the association of the gravitational wave energy to the energy released during the event. If equations 3.11, 3.20, 3.21 and 3.22 are combined, the relation of the total gravitational wave energy radiated  $\Delta E_{\text{GW}}$  and the energy of the mode  $E_{\text{mode}}$  will take the form

$$\Delta E_{\text{GW}} = \frac{\tau}{|\tau_{\text{GRR}}|} E_{\text{mode}}, \quad (3.26)$$

that in combination with equation 3.25 gives,

$$h_{\text{rss}} = \frac{1}{r} \left[ \frac{45G}{4c^3} \frac{\tau}{|\tau_{\text{GRR}}|} \frac{E_{\text{mode}}}{\Omega^2} \right]^{1/2}. \quad (3.27)$$

This equation, in contrast with equation 3.25 which is in terms of the gravitational wave energy, is a relation between the detectability parameter  $h_{\text{rss}}$  and the energy released by the mode oscillation.

The ratio between the total timescale of the waveform and the timescale due to the *GRR* in equation 3.26 means that the amount of energy transferred from the mode to the gravitational wave is modulated by this ratio of timescales. Moreover, if the total timescale  $\tau$  is mainly dominated by the dissipation processes in the inner layers of the NS, such as in the Levin and Ushomirsky model, and if this timescale is much smaller than the  $|\tau_{\text{GRR}}|$ , equation 3.26 means that only a small fraction of the energy released by the mode oscillation will be transferred to the gravitational wave. This also means that  $\Delta E_{\text{GW}} \ll E_{\text{mode}}$  and that the remaining energy will be dissipated.

### 3.4.1 The $\beta$ parametrisation

In order to make a model-independent estimate of the amount of energy transferred to the gravitational wave, this energy could be parametrised by a parameter  $\beta$  given by

$$\beta \equiv \frac{\Delta E_{\text{GW}}}{E_{\text{mode}}}, \quad (3.28)$$

which sets the relation between the timescales  $\tau$  and  $-\tau_{\text{GRR}}$

$$\tau = \beta(-\tau_{\text{GRR}}). \quad (3.29)$$

Assuming that the timescale is dominated by dissipation processes  $\tau_{\text{dissipation}}$ , the  $\beta$ -parametrised equation that relates this timescale and  $-\tau_{\text{GRR}}$ , using equation 3.10, is:

$$\tau_{\text{dissipation}} = \frac{\beta}{\beta + 1}(-\tau_{\text{GRR}}). \quad (3.30)$$

In figure 3.6, the result of a calculation of the timescale  $\tau$  as a function of  $\beta$ , with respect to the  $f_{\text{star}}$  of the pulsars in appendix A, is presented. These timescales were constructed with values of  $\beta \in [10^{-10}, 10^{-1}]$  with a step of  $10^{-1}$ . This interval is selected in order to cover a broad range while maintaining the values of  $\beta$  in a realistic physical scenario. For most of the timescale values obtained, the plausibility to be considered in this study is null, either because they are out of the spin frequency range that this work is focused on (100 Hz-1kHz), or because some of these timescales have durations comparable to the age of the Universe ( $\sim 10^{16}$  s) which are not physically possible. Then, from figure 3.6, it can be concluded that the values of  $\tau(\beta)$  to be considered in this thesis should be  $\tau(\beta) < 10^5$  s. This is due to the fact that the goal of this study is to search for long-transient gravitational wave signals with durations up to one week. Also, faster spinning stars lead to more feasible values of the waveform timescale.

Now, using the  $\beta$ -parametrisation, the detectability parameter  $h_{\text{rss}}$  in terms of the energy of the mode, using equation 3.27, is:

$$h_{\text{rss}} = \frac{1}{r} \left[ \frac{45G}{4c^3} \beta \frac{E_{\text{mode}}}{\Omega^2} \right]^{1/2}. \quad (3.31)$$

Considering the first scenario of the waveform timescales as a function of  $f_{\text{star}}$  discussed in section 3.2.3, where  $\tau_{\text{dissipation}} \ll |\tau_{\text{GRR}}|$ , the parameter  $\beta$  should be  $\beta \ll 1$ . In the second scenario, in which  $\tau_{\text{dissipation}} \rightarrow |\tau_{\text{GRR}}|$ , a very large

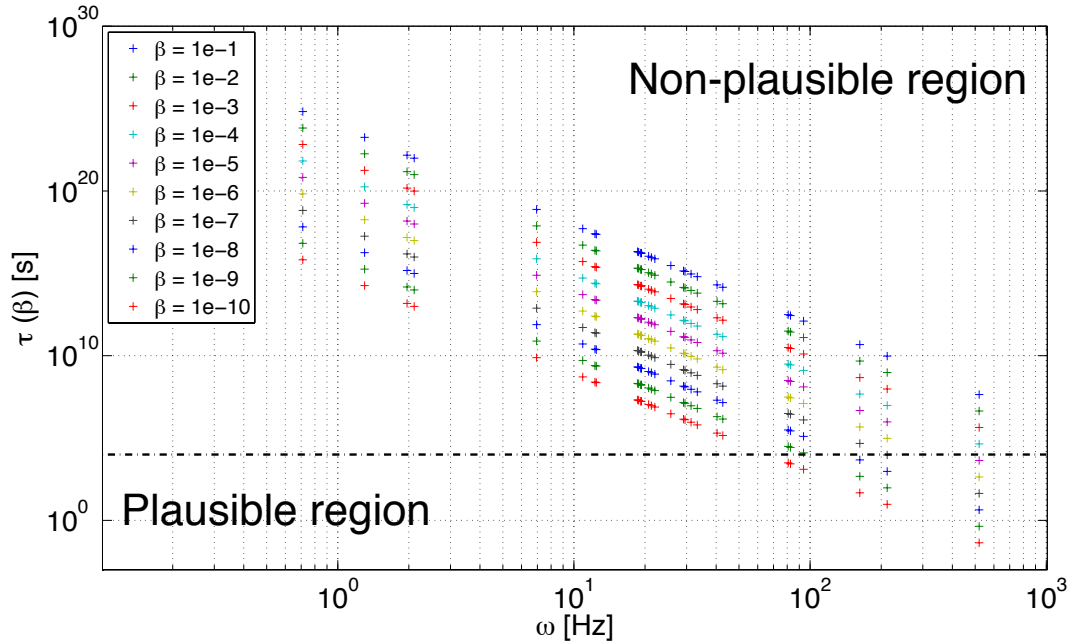


Figure 3.6: **The damping time  $\tau$  as a function of the frequency  $\omega$  for different values of  $\beta$ .** This plot is presented to show the viability of the use of the  $\beta$  parameter to construct the duration of a waveform. This plot considers data from young pulsars only, so no data for the millisecond pulsars are included. The values of  $\beta$  considered in this plot go from  $10^{-10}$  to  $10^{-1}$  in steps of  $10^{-1}$ , so ten values of  $\beta$  per pulsar are shown. The non-plausible region, separated by a dot-dashed line, is where the timescales are out of the scope of this work or physically not viable. This leaves  $\tau(\beta) \leq 10^5$  s for fast spinning frequency pulsars as the only plausible sources to be considered in the present analysis.

amount of gravitational wave energy emitted is implied which translates into values of  $\beta \approx 1$ .

### 3.5 Neutron star transients detection

In the previous section, a series of calculations led to general equations for the  $E_{\text{GW}}$  and  $h_{\text{rSS}}$  considering  $r$ -mode gravitational wave emissions, but not for a particular transient event. The values of the detection parameters associated with these events rely on how the released energy is measured and how much of this energy is considered to be deposited into the gravitational wave energy.

### 3.5.1 Pulsar glitch detection

As was mentioned in chapter 2, pulsar glitches are associated with a transfer of angular momentum  $\mathcal{L} = I\Omega$  within the NS. The principle of the angular momentum conservation implies that small changes in  $\Omega$  will be reflected in changes of the moment of inertia  $I$ , so  $\Delta\Omega \propto \Delta I$ . In order to determine the energy emitted during a pulsar glitch, the assumption of a spherical NS with a moment of inertia  $I$  is considered, where  $I$  is defined as  $I = \tilde{I}MR^2$ . From [60],  $\tilde{I}$  is defined as

$$\tilde{I} = \frac{8\pi}{3MR^2} \int_0^R \rho r^4 dr. \quad (3.32)$$

Some models predict the value of  $\tilde{I}$  between 0.30 and 0.45 for stiffness values of the NS ( $M/R$ ) between 0.1 and 0.2 [36]. For example,  $I = 10^{45} \text{ g cm}^2$  corresponds to values of  $\tilde{I} = 0.4$ ,  $M = 1.4 M_\odot$  and  $R = 10 \text{ km}$ .

The energy released during the glitch, is a relation between the moment of inertia and the magnitude of the glitch

$$E_{\text{glitch}} = I\Omega\Delta\Omega = I\Omega^2 \frac{\Delta\Omega}{\Omega}. \quad (3.33)$$

Switching  $E_{\text{mode}} = E_{\text{glitch}}$ , equation 3.31 takes the form

$$h_{\text{rss}} = \frac{1}{r} \left[ \frac{45G}{4c^3} \beta \frac{E_{\text{glitch}}}{\Omega^2} \right]^{1/2} \quad (3.34)$$

and in terms of  $\Delta\Omega/\Omega$ ,

$$h_{\text{rss}} = \frac{1}{r} \left[ \frac{45G}{4c^3} \beta I \frac{\Delta\Omega}{\Omega} \right]^{1/2}. \quad (3.35)$$

Note that these equations consider the optimistic assumption that the  $E_{\text{glitch}}$  and the  $E_{\text{mode}}$  are the same. The importance of these equations is that they show the detectability parameter at the gravitational wave detector taken as

function of observed parameters of the star. Also, in this case, the modulation of the energy transferred to the gravitational wave is given by  $\beta$ . However, an equation with the timescales ratio modulation can be obtained from equation 3.31.

With the optimistic assumption described by equations 3.34 and 3.35, and using equations 3.22 and 3.33, an expression for the mode amplitude parameter  $\alpha$  is given by,

$$\alpha = \left(\frac{\tilde{I}}{\tilde{J}}\right)^{1/2} \left(\frac{\Delta\Omega}{\Omega}\right)^{1/2}. \quad (3.36)$$

This shows that for small glitches,  $\Delta\Omega/\Omega \sim 10^{-6}$ , the mode amplitude gives small values,  $\alpha < 1$ . To estimate the gravitational wave amplitude,  $\alpha$  can conveniently be inserted into equation 3.21 leading to

$$h_0 = \frac{G}{c^5} \sqrt{\frac{2\pi}{c^5}} \left(\frac{4}{3}\right)^3 \frac{1}{r} \Omega^3 M R^3 (\tilde{I}\tilde{J})^{1/2} \left(\frac{\Delta\Omega}{\Omega}\right)^{1/2} \quad (3.37)$$

that in terms of the glitch energy:

$$h_0 = \frac{G}{c^5} \sqrt{\frac{2\pi}{c^5}} \left(\frac{4}{3}\right)^3 \frac{1}{r} \Omega^2 M^{1/2} R^2 (\tilde{J})^{1/2} E_{\text{glitch}}^{1/2}. \quad (3.38)$$

Finally, the  $h_{\text{rss}}$  detectability parameter in terms of the glitch energy, using equation 3.27 and setting  $E_{\text{glitch}} = E_{\text{mode}}$  is

$$h_{\text{rss}} = \frac{1}{r} \left[ \frac{45G}{4c^3} \frac{\tau}{|\tau_{\text{GRR}}|} \frac{E_{\text{glitch}}}{\Omega^2} \right]^{1/2}. \quad (3.39)$$

A correlation between this detection parameter  $h_{\text{rss}}$  and  $f_{\text{star}}$  is presented on the left panel of figure 3.7. Also in this figure the distinction between pulsars with  $N_{\text{glitches}} < 5$  and  $N_{\text{glitches}} > 5$  is shown in both panels. On the right-hand side panel the relation of the detection parameter and the source's distance is shown.

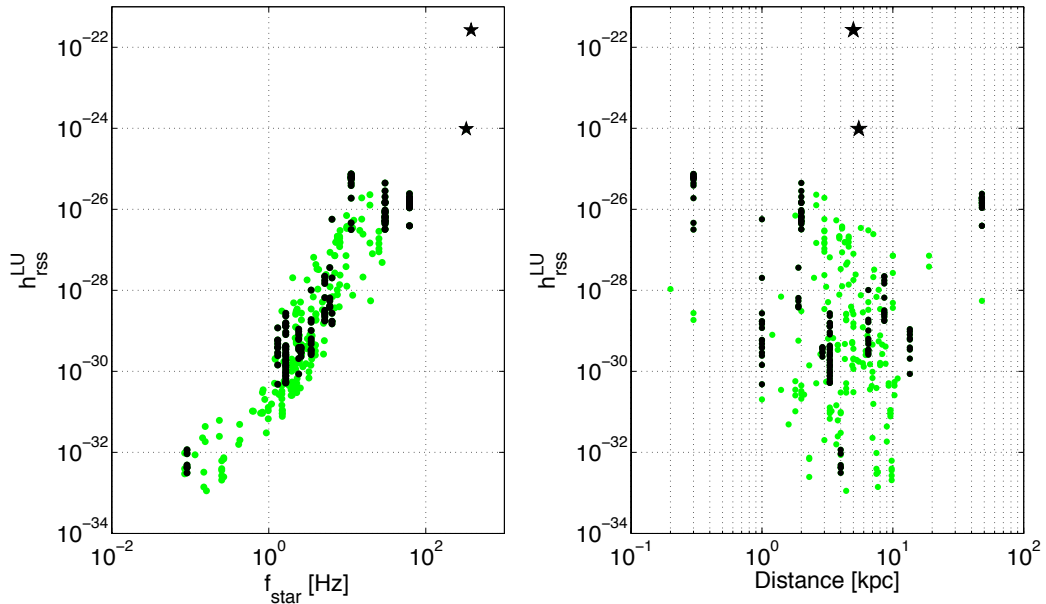


Figure 3.7: **Detection parameter  $h_{\text{rss}}^{\text{LU}}$  for pulsar glitches.** This plot shows in green markers all the glitches considered in this study from appendix A, and in black markers glitches from the frequent glitching pulsars ( $> 5$ ). The left hand side panel shows a big dependence of the parameter  $h_{\text{rss}}^{\text{LU}}$  on the  $f_{\text{star}}$ . The starred markers denote the glitches from the millisecond pulsars, the top star corresponding to HETE J1900.1–2455 and the bottom star to PSR J1824–2452. The difference in the detectability parameter for these last two pulsars is due to the Levin and Ushomirsky model that considers rubbing effects in the crust core interface for rapid rotating stars.

### 3.5.2 Type I X-ray burst transients detection

In table 2.2, extracted from [43], the three main types of Type I X-ray bursts can be seen. In the context of this study, transient events associated with super-bursts will be the ones of interest because of three of their features:

1. The amount of energy released during these events. In super-bursts the EM energy released is  $\sim 10^{41} - 10^{42}$  ergs.
2. A fast and well known  $f_{\text{star}}$  of the NS component of the binary system that could be between 300-620 Hz. In particular, this feature is of major importance in the context of this study if the Levin & Ushomirsky dissipation model is considered. This feature is sometimes measured during a burst.

3. Their duration, which gives the long transient nature, which could be up to the order of days. The duration depends on how deep inside the NS the nuclear burning takes place, which in turn depends on the cooling timescale of the burning layer.

Another important and useful feature of these sources that is of interest for this study is that these sources have estimated distances of a few kpc.

There is a description in [43] of these different types of Type I X-ray bursts as well as the observed energy released by these bursts from ten sources.

For this case, an assumption in terms of the energy has to be done, this is that

$$E_{\text{mode}} = E_{\text{burst}}. \quad (3.40)$$

This optimistic assumption means that the total EM energy detected during a burst goes into the  $r$ -mode. With this in mind, and with equation 3.22, an equation for the mode amplitude  $\alpha$  can be set as

$$\alpha = \left( \frac{E_{\text{burst}}}{\Omega^2 M R^2 \tilde{J}} \right)^{1/2} \quad (3.41)$$

In combination with equation 3.21, the initial amplitude of the gravitational wave can be expressed as

$$h_0 = \left[ \frac{8\pi G}{5} \frac{E_{\text{burst}} M \tilde{J}}{c^5 r^2} \omega^4 R^4 \right]^{1/2}. \quad (3.42)$$

And also, an expression for the detectability statistic  $h_{\text{rss}}$ , using equation 3.42

$$h_{\text{rss}} = \frac{1}{r} \left[ \frac{45G}{4c^3} \frac{\tau}{|\tau_{\text{GRR}}|} \frac{E_{\text{burst}}}{\Omega^2} \right]^{1/2}. \quad (3.43)$$

### 3.5.3 Refinement of the Levin & Ushomirsky model

In their figure 2, Ho et al [64] did a similar  $\Omega$ - $T$  plot to figure 2 in the Levin & Ushomirsky [50] paper, but with the actual locations of the **Low Mass X-ray Binaries** (LMXBs) marked. This plot reveals that there might be problems for this type of objects with the Levin & Ushomirsky model because it leaves many LMXBs in an unstable regime due to the value of  $\delta u/u \approx 0.1$ . In addition, it shows that a value of  $\delta u/u \approx 1$  would bring these sources back to a stable regime. Particularly, the problem in setting the value of the slippage parameter to 1, is that the NS crust is assumed to be rigid, which is not a completely accepted model. Ho et al, suggest some reasons why  $\delta u/u$  should be close to unity, amongst which are the existence of resonances that could produce ‘spikes of stability’ in the  $\Omega$ - $T$  plane, or the bulk viscosity due to hyperons, or superfluids mutual friction.

As a first approach, one could ask how far from the spinning frequency of a star an  $f_{\text{critical}}$  can be in order for the star to be stable. According to Haskell et al [65], the fastest LMXBs, PSR 4U 1608–522, has a  $f_{\text{star}} = 620$  Hz and a core temperature estimation of  $4.55 \times 10^8$  K. This study listed 22 sources within a  $f_{\text{star}}$  interval from 174 to 620 Hz. This means that, on average, these sources are spread on steps of  $\sim 20$  Hz, which leads to a maximum value for  $f_{\text{critical}}$  of 640 Hz. This will be the first criterium used in this work to estimate the value of  $f_{\text{critical}}$ .

Another argument is supported by Chakrabarty et al [66], in which they performed a statistical analysis of the distribution of the LMXB in order to get an upper limit to a cutoff frequency. They found that this frequency lies at 730 Hz with 95% of confidence. Later, Patruno [67] confirmed these findings incrementing the confidence level to 99%. This is in agreement with the fastest pulsar known with an  $f_{\text{star}} = 716$  Hz mentioned before.

Exploring the timescale equations with these ideas in mind, the balance between  $\tau_{vbl}$  and  $\tau_{GRR}$  is done by setting  $-\tau_{GRR} = \tau_{vbl}$  using equations 3.11 and 3.14. From this, an equation for  $f_{\text{critical}}$  can be written as

$$f_{\text{critical,kHz}} = 0.821 F^{1/11} \left( \frac{\delta u}{u} \right)^{4/11} \frac{1}{T_8^{2/11} M_{1.4}^{4/11} R_{11.7}^{4/11}} \quad (3.44)$$

where  $M_{1.4}$  and  $R_{11.7}$  are the mass of  $1.4 M_\odot$  and the radius of 11.7 km, respectively. Solving this equation for the combination of  $F$  and  $\delta u/u$  and assuming that there is an estimation of the  $T_{\text{core}}$ ,

$$F^{1/2} \left( \frac{\delta u}{u} \right)^2 = \left( \frac{f_{\text{star,critical}}}{f_{\text{star}}} \right)^{11/2} M_{\text{star}}^2 R_{\text{star}}^2 \quad (3.45)$$

where  $M_{\text{star}}$  and  $R_{\text{star}}$  are the mass and the radius of the star from which the  $f_{\text{star,critical}}$  is considered, and  $f_{\text{star,critical}} > f_{\text{star}}$ . Also,  $T_{\text{core}}$  is the temperature estimation of the source at the core. This assumption can be used for all the LMXB and with the help of equation 3.45, the Levin & Ushomirsky damping time could be written in terms of  $f_{\text{critical}}$  as

$$\frac{1}{\tau_{vbl}} = \frac{f_{\text{kHz}}^{1/2}}{T_8} \frac{R_{11.7}^2}{M_{1.4}} \left( \frac{f_{\text{star,critical}}}{f_{\text{star}}} \right)^{11/2} M_{\text{star}}^2 R_{\text{star}}^2 \quad (3.46)$$

and equation 3.44 would take the form

$$f_{\text{critical,Khz}} = \frac{1}{T_8^{2/11} M_{1.4}^{4/11} R_{11.7}^{4/11}} \left( \frac{f_{\text{star,critical}}}{f_{\text{star}}} \right) M_{\text{star}}^{4/11} R_{\text{star}}^{4/11} \quad (3.47)$$

These equations consider that  $M_{\text{star}}$  and  $R_{\text{star}}$  are unknown and they will be the starting point for the numerical estimates for these kind of stars.

### 3.6 Numerical estimates

With the calculations in the previous section, the evaluation of them with NS observed parameters and the corresponding comparisons with gravitational wave detector sensitivities has been done.

In figure 3.8, the estimated value of the detection parameter  $h_{\text{rSS}}$ , calculated with the  $\beta$  parameter and with the Levin & Ushomirsky model for timing glitches from young pulsars and for Type I X-Ray bursts from LMXBs, is presented. A value of  $\beta = 10^{-5}$ , has been used for this calculation. This first set of calculations was done considering the Levin & Ushomirsky model before the reinterpretation of the  $f_{\text{critical}}$  for the case of the LMXB.

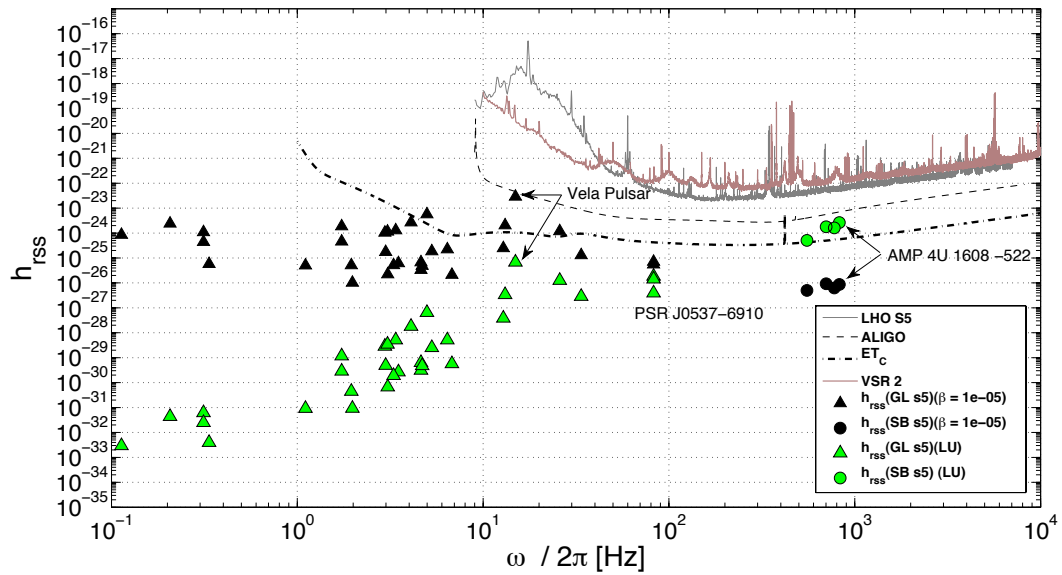


Figure 3.8:  $h_{\text{rSS}}$  of glitches and Type I X-Ray bursts and gravitational wave detectors sensitivity curves. This plot compares the estimation of the detection parameter  $h_{\text{rSS}}$  calculated with the assumption of the Levin & Ushomirsky model (green markers) and using the  $\beta$  parametrisation with  $\beta = 10^{-5}$  (black markers), with the current and future gravitational wave detectors. Current detectors, LIGO in grey and VIRGO in brown are shown, as well as estimated sensitivity lines for ALIGO and ET. Triangle markers correspond to glitches produced by young pulsars and circles represent Type I X-Ray bursts from accreting millisecond pulsars.

From figure 3.8 the contrasting effects in the value of  $h_{\text{rSS}}$  when the timescale of the signal is calculated with the Levin & Ushomirsky model in mind and

with the  $\beta$  parametrisation, can be seen. In this figure, the calculations for glitches that happened during the Science Run 5 of the LIGO detectors are shown in triangles and the Type I X-ray bursts, with no restrictions in their selection, in circles. The detectability parameter  $h_{\text{rss}}$  is presented in comparison with the noise curves of current gravitational wave detectors, LIGO H1 and VIRGO, and with the sensitivity curves of future detectors, like ALIGO and ET. With the  $\beta$  parametrisation  $h_{\text{rss}}$  tends to increase proportionally to the  $f_{\text{star}}$ , while on the other hand using the Levin & Ushomirsky model the relation is inversely proportional. This suggests that for young pulsars the  $\beta$  parametrisation gives more plausible numbers for a detection. For faster rotators the Levin & Ushomirsky model gives better estimates of  $h_{\text{rss}}$ , which is in agreement with the value of the slippage parameter  $\delta u/u$  in this model which, for faster spinning stars with  $f_{\text{star}} \geq 100$  Hz, plays a significant role in the calculation of the timescale.

For the millisecond pulsars that have presented a glitch, described in section 2.4.1, a calculation of  $h_{\text{rss}}$  with the  $\beta$  parametrisation and the Levin & Ushomirsky model is presented in figure 3.9. In this figure, the equivalence for the  $\beta$  parametrisation of the amount of energy transferred from the glitch to the mode using the Levin & Ushomirsky model is presented. This equivalence leads to a value of  $\beta \sim 1$ , which means that almost all the energy released by the glitch is transferred to the gravitational wave.

With the information obtained from figures 3.8 and 3.9, an initial selection of sources that can be used in this work is presented, with their main characteristics, in table 3.1.

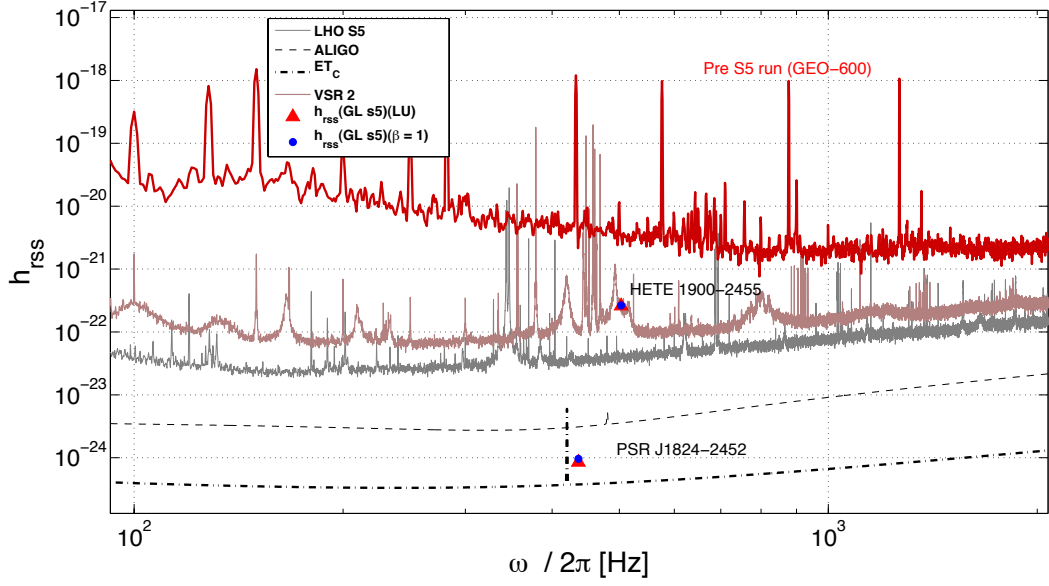


Figure 3.9:  $h_{\text{rss}}$  of glitches from MSP. This plot shows the comparison of noise curves of current gravitational wave detectors and sensitivity curves of future gravitational wave detectors with the estimated  $h_{\text{rss}}$  of the two millisecond pulsars that have presented a timing glitch (see section 2.4.1). In this plot the sensitivity curve of the Pre S5 run performed by the GEO-600 detector is included. This corresponds to the day in which the HETE 1900–2555 event happened (MJD 53,559). This plot is important to illustrate that the comparison between the  $\beta$  parametrisation method and the Levin & Ushomirsky model leads to the interpretation that  $E_{\text{glitch}} = E_{\text{GW}}$ .

Table 3.1: **Representative sources for the analysis.** This table shows the main characteristics of the sources that are considered in the analysis, based on the criteria shown in this chapter with the Levin & Ushomirsky timescale model before the reinterpretation based on  $f_{\text{critical}}$ . The observational parameters were collected from [25], [41], [42], [68] and [69]. Pulsar \*, is the only millisecond pulsar that has produced a  $\mu$  glitch, and pulsar \*\* had a  $f_{\text{star}}$  spin up event but was not considered as a glitch by the observers.

Source	$r$ (kpc)	$f_{\text{star}}$ (Hz)	$\alpha$	$\tau_{\text{LU}}$ (s)	$E_{\text{burst}}^{\text{glitch}} / \text{ergs}$	$h_{\text{rss}}^{\text{LU}} (10^{-25})$
PSR J0835–4510	0.3	11.19	$3.98 \times 10^{-3}$	690.6	$4.94 \times 10^{42}$	0.421
PSR J0537–6910	48	62.02	$2.82 \times 10^{-3}$	293.4	$7.6 \times 10^{43}$	0.206
PSR J1824–2452*	5.6	327.40	$1.23 \times 10^{-5}$	20456	$4.02 \times 10^{40}$	9.669
HETE J1900.1–2455**	4.7	377.26	$3.10 \times 10^{-3}$	8687	$3.37 \times 10^{45}$	2662
4U 1608 -522 (burst)	3.2	620	$3.1 \times 10^{-5}$	402.7	$4 \times 10^{41}$	26.33

For example, the estimated  $E_{\text{glitch}}$  of the Vela pulsar, PSR J0835–4510, the most prolific amongst timing glitch-producers, is set using equation 3.33 as

$$E_{\text{glitch}} \sim 4.95 \times 10^{42} \text{ergs} \left( \frac{f_{\text{star}}}{11.2 \text{ Hz}} \right)^2 \left( \frac{\Delta\Omega/\Omega}{10^{-6}} \right), \quad (3.48)$$

and for the fastest spinning young NS in the database in appendix A, PSR J0537–6910,

$$E_{\text{glitch}} \sim 7.59 \times 10^{43} \text{ergs} \left( \frac{f_{\text{star}}}{62 \text{ Hz}} \right)^2 \left( \frac{\Delta\Omega/\Omega}{5 \times 10^{-7}} \right). \quad (3.49)$$

Also, for these two same stars, the values of the amplitude of the mode  $\alpha$ , following [60] and using  $\tilde{I} = 0.261$  and  $\tilde{J} = 1.64 \times 10^{-2}$  are, respectively

$$\alpha = 3.99 \times 10^{-3} \left( \frac{\Delta\Omega/\Omega}{10^{-6}} \right) \quad \alpha = 2.82 \times 10^{-3} \left( \frac{\Delta\Omega/\Omega}{5 \times 10^{-7}} \right) \quad (3.50)$$

and for a hypothetical Type I X-Ray burst, from equation 3.22

$$\alpha = 6.7 \times 10^{-5} \left( \frac{E_{\text{burst}}}{10^{42} \text{ergs}} \right)^{1/2} \left( \frac{300 \text{ Hz}}{f_{\text{spin}}} \right). \quad (3.51)$$

To get an estimate of the gravitational wave amplitude, the use of equation 3.37 for the Vela pulsar gives

$$h_0 = 1.68 \times 10^{-27} \left( \frac{287 \text{ pc}}{r} \right) \left( \frac{f_{\text{star}}}{11.2 \text{ Hz}} \right)^3 \left( \frac{\Delta\Omega/\Omega}{10^{-6}} \right)^{1/2} \quad (3.52)$$

and for PSR J0537–6910

$$h_0 = 1.20 \times 10^{-27} \left( \frac{48.1 \text{ kpc}}{r} \right) \left( \frac{f_{\text{star}}}{62 \text{ Hz}} \right)^3 \left( \frac{\Delta\Omega/\Omega}{5 \times 10^{-7}} \right)^{1/2}. \quad (3.53)$$

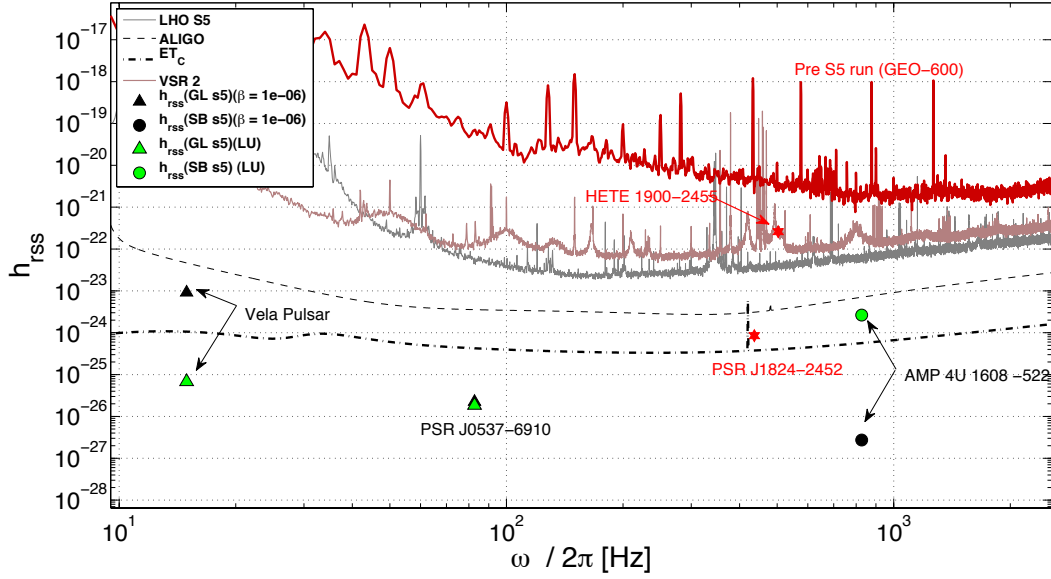


Figure 3.10:  $h_{\text{rss}}$  for selected sources with gravitational wave detector sensitivity curves. In this plot the sources from table 3.1 with respect to the current gravitational wave detectors noise and future gravitational wave sensitivity curves, are shown. For each source the estimated detection parameter  $h_{\text{rss}}$  is plotted with the assumption of the Levin & Ushomirsky model (green markers) and using the  $\beta$  parametrisation with  $\beta = 10^{-6}$  (black markers). This value of  $\beta$  was used to show that a millionth of the energy of the glitch/burst is transferred to the gravitational wave. In the case of PSR J0537–6910, the two statistics coincide. Also in this plot, the sensitivity curve of GEO 600 during the Pre-S5 run, is included. This is because during this period (MJD 53,559), the spin up event in HETE J1900.1–2455 happened.

In the context of the timescales, the dissipation model by Levin & Ushomirsky in equation 3.14 gives for PSR J0537–6910 pulsar

$$\tau_{\text{vbl}} = \tau_{\text{dissipation}}^{\text{LU}} = 293.4 \text{ s} \frac{T_8}{F^{1/2}} \left( \frac{62 \text{ Hz}}{f_{\text{star}}} \right)^{1/2} \left( \frac{\delta u}{u} \right)^{-2} \quad (3.54)$$

where  $T_8$ ,  $F$  and  $\delta u/u$  are factors of order unity. Combining this equation with equation 3.11, the regime where  $\tau_{\text{dissipation}} \ll |\tau_{\text{GRR}}|$  can be seen and so can be approximated to  $\tau \approx \tau_{\text{dissipation}} = \tau_{\text{dissipation}}^{\text{LU}}$  as

$$\frac{\tau_{\text{LU}}}{\tau_{\text{GRR}}} \approx \frac{\Delta E_{\text{GW}}}{E_{\text{glitch}}} = 6.76 \times 10^{-7} \frac{T_8}{F^{1/2}} \left( \frac{f_{\text{star}}}{62 \text{ Hz}} \right)^{11/2} \left( \frac{\delta u}{u} \right)^{-2} \quad (3.55)$$

From this equation a very steep scaling with  $f_{\text{star}}$  is noticeable. Also, for the

PSR J0537–6910, only  $\sim$  one-millionth of the glitch energy ( $\beta \sim 10^{-6}$ ) is transferred to gravitational waves, as seen in figure 3.10. If this scheme is considered, equation (3.43) becomes

$$h_{\text{rss}}^{\text{LU}} = \frac{1}{r} \left[ \frac{45G}{4c^3} \frac{E_{\text{glitch}}}{\Omega^2} \frac{\tau_{\text{LU}}}{\tau_{\text{GRR}}} \right]^{1/2} \quad (3.56)$$

and from equations (3.55) and (3.56)

$$h_{\text{rss}}^{\text{LU}} = 2.06 \times 10^{-26} \left( \frac{48.1 \text{ kpc}}{r} \right) \left[ \frac{T_8}{F^{1/2}} \left( \frac{\delta u}{u} \right)^{-2} \left( \frac{f_{\text{spin}}}{62 \text{ Hz}} \right)^{7/2} \left( \frac{E_{\text{glitch}}}{7.6 \times 10^{43} \text{ erg}} \right) \right]^{1/2}, \quad (3.57)$$

that in terms of the amplitude of the glitch

$$h_{\text{rss}}^{\text{LU}} = 2.06 \times 10^{-26} \left( \frac{48.1 \text{ kpc}}{r} \right) \left[ \frac{T_8}{F^{1/2}} \left( \frac{\delta u}{u} \right)^{-2} \left( \frac{f_{\text{spin}}}{62 \text{ Hz}} \right)^{11/2} \left( \frac{\Delta\Omega/\Omega}{5 \times 10^{-7}} \right) \right]^{1/2}. \quad (3.58)$$

If the  $\beta$  parametrisation is considered in the regime where  $\tau_{\text{viscosity}} \ll |\tau_{\text{GRR}}|$ , then in the context of young pulsars,  $\beta \ll 1$ . Given that  $\tau_{\text{GRR}}$  is a known function of frequency, this also gives the time on which the mode decays, and with equation (3.29)

$$\tau = \beta |\tau_{\text{GRR}}| = 4.34 \times 10^6 \text{ s} \left( \frac{\beta}{10^{-2}} \right) \left( \frac{62 \text{ Hz}}{f_{\text{spin}}} \right)^6 \quad (3.59)$$

that leads, for the PSR J0537–6910, to

$$h_{\text{rss}}(\beta) = 2.51 \times 10^{-24} \left( \frac{48.1 \text{ kpc}}{r} \right) \left( \frac{62 \text{ Hz}}{f_{\text{spin}}} \right) \left( \frac{\beta}{10^{-2}} \right)^{1/2} \left( \frac{E_{\text{glitch}}}{7.6 \times 10^{43} \text{ erg}} \right)^{1/2} \quad (3.60)$$

and from equation 3.35

$$h_{\text{rss}}(\beta) = 2.51 \times 10^{-24} \left( \frac{48.1 \text{ kpc}}{r} \right) \left( \frac{\beta}{10^{-2}} \right)^{1/2} \left( \frac{\Delta\Omega/\Omega}{5 \times 10^{-7}} \right)^{1/2} \quad (3.61)$$

### 3.6.1 Stabilised LMXBs

The reinterpretation of the Levin & Ushomirsky dissipation model in terms of the  $f_{\text{critical}}$ , discussed in section 3.5.3, leads to the construction of an instability curve. Lets consider, for example, the source PSR 4U1608–522 with  $f_{\text{star}} = 620 \text{ Hz}$  and  $T = 4.55 \times 10^8 \text{ K}$  reported in [65]. With these data, equations 3.45, 3.46 and 3.47 will take the form

$$F^{1/2} \left( \frac{\delta u}{u} \right)^2 = 0.968 \left( \frac{f_{\text{critical},4\text{U}1608}}{f_{\text{star}}} \right)^{11/2} M_{4\text{U}1608}^2 R_{4\text{U}1608}^2 \quad (3.62)$$

$$\tau_{\text{vbl}} = 0.0133 \text{ s}^{-1} \frac{f_{\text{kHz}}^{1/2}}{T_8} \frac{R_{11.7}^2}{M_{1.4}} \left( \frac{f_{\text{critical},4\text{U}1608}}{f_{\text{star}}} \right)^{11/2} M_{4\text{U}1608}^2 R_{4\text{U}1608}^2 \quad (3.63)$$

and equation 3.44 could take the form

$$f_{\text{critical,kHz}} = 0.817 \frac{1}{T_8^{2/11} M_{1.4}^{4/11} R_{11.7}^{4/11}} \left( \frac{f_{\text{critical},4\text{U}1608}}{f_{\text{star}}} \right)^{11/2} M_{4\text{U}1608}^2 R_{4\text{U}1608}^2 \quad (3.64)$$

In order to get a gravitational wave detectability statistic  $h_{\text{rss}}$  of these sources using equations 3.23 and 3.42, the energy released by Type I X-ray bursts, the  $f_{\text{star}}$ , their distance to the solar system baricentre and the estimation of the internal temperature are needed.

Table 3.2 shows these observed parameters and the calculations of the detectability statistic  $h_{\text{rss}}$  and the duration of the signals. Figure 3.11, is the corresponding plot of these calculations with respect to the sensitivity curves.

Table 3.2: **Type I X-Ray sources tested for detectability.** These calculations are based on an  $f_{\text{critical}} = 640$  Hz and  $f_{\text{critical}} = 730$  Hz.

name PSR	Dist [Kpc]	Energy $\times 10^{41}$ [erg] <sup>†</sup>	$f_{\text{star}}$ [Hz] **	$T^*$ [ $10^8$ K]	$h_0$ $\times 10^{-25}$	$\tau$	$h_{\text{rss}}$	$\tau$	$h_{\text{rss}}$
						[s]	$\times 10^{-25}$	[s]	$\times 10^{-25}$
						$f_{\text{critical}} = 640$ Hz	$f_{\text{critical}} = 730$ Hz		
4U 1608–522	3.2	4.0	620.0	4.55 <sup>‡</sup>	1.968	2309	94.60	300.7	34.13
4U 0614+091	3.2	0.66	415.0	1.00	0.227	100.6	2.28	48.3	1.58
KS 1731–260	5.6	10	526.3	1.00	0.854	94.6	8.31	44.1	5.67
4U 1636–536	6.0	6.5	582.0	1.00	0.786	95.7	7.69	43.1	5.16
4U 1820–303	6.4	14	275.5	1.00	0.242	121.3	2.67	58.8	1.86
4U 1735–44	6.5	5.0	249.0	1.00	0.116	127.4	1.31	61.8	0.91
GX 17+2	9.8	3.0	272.0	1.00	0.071	122.0	0.78	59.1	0.55

<sup>†</sup> Keek et al 2008 [43]

<sup>‡</sup> Haskell et al 2012 [65]

\* All the sources of which an estimate of  $T_{\text{core}}$  is not available were set to  $10^8$  K

\*\* Strohmayer et al 2008 [70], Strohmayer et al 2002 [71], Smale et al 1997 [72], Wijnands et al 1998 [73], Migliari et al 2011 [74].

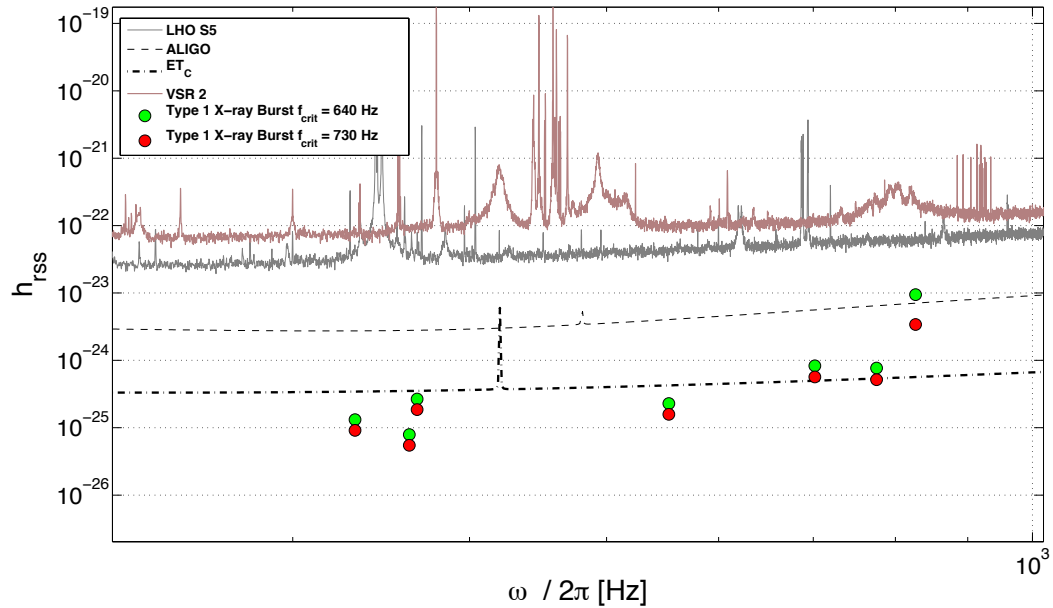


Figure 3.11:  $h_{\text{rss}}$  of LMXBs in the stable regime and gravitational wave detectors sensitivity curves. The position of the detectability statistic  $h_{\text{rss}}$  with respect to the current detectors shows that it is not possible to detect gravitational waves with these detectors. Nevertheless, the detection with future detectors of 2nd and 3rd generations is more plausible.

### 3.6.2 Summary

From the numerical estimations done in this chapter, as well as the expected values of the parameter  $h_{\text{RSS}}$ , the potential detection by future gravitational wave detectors of a gravitational wave emitted during a glitch produced by a millisecond pulsar or during a Type I X-ray burst, is considered.

For the case of the detection of gravitational waves from pulsar glitches, most of the sources have detectability estimations even below the third generation curves. In this case the  $\beta$  parametrisation gives more optimistic results. On the other hand, Type I X-Ray bursts from LMXBs have better detectability estimations with respect to future gravitational wave detectors, if the Levin & Ushomirsky parametrisation is considered. These sources are going to be of special interest in the next chapter.

# Chapter 4

## Search for long transient gravitational waves from *r*-modes

In this chapter, a detailed description of the method used for the search for long transient gravitational wave signals associated with transient events in NS is presented, as well as the application of this method to long transient signals injected in white simulated noise. Firstly, a description of several tools to be used in the analysis, such as the signal-to-noise ratio SNR, is given. Also, a detailed description of heterodyning, a method that is used to make long signals easier to compute, is shown. Then, a matched filtering method called  $\mathcal{F}$ -statistic, proposed by Jaranowski, Królak and Schutz in 1998 [75] and originally used for the search of continuous gravitational wave signals, is described. Following this, a method proposed by Prix, Giampanis and Messenger [1] which is an adaptation of the  $\mathcal{F}$ -statistic search for transient gravitational waves is described. Then, for the first time, this method is put into practice by injecting transient signals in white noise of gravitational wave

data at the sensitivity level of the ET. Finally, the results obtained from these searches are shown.

## 4.1 Gravitational wave data

The data recorded by the gravitational wave detectors are stored as time-series data. They are the primary component of the Data Frame Format files which are the standard way the **LIGO** and **Virgo Scientific Collaboration (LVC)** stores data. The timing of the data is based on the GPS time which has a resolution of  $10^{-9}$  s. With this timing, the uniqueness of data is guaranteed, for either real or simulated data. The amplitude, frequency and phase of the data are some of the key elements for the association of gravitational wave signals with astrophysical events. A convention for the analysis of these data in the frequency domain has been adopted without ruling out any important information that can be obtained from the time-series, such as the variation over time of the frequency. In order to achieve this goal, the original gravitational wave data are transformed using the so-called **Short-time Fourier Transform (SFT)** which, in a very simplified way, can be understood as ‘snap-shots’ of the data during a specific time. This SFT is defined as:

$$\mathbf{SFT}\{x(t)\} \equiv X(\tau_{\omega_s}, \omega_s) = \int_{-\infty}^{\infty} x(t)\omega_s(t - \tau_{\omega_s})e^{-j\omega_s t} dt \quad (4.1)$$

where  $\omega_s$  is a window function that is non-zero for a period of time defined by the time-range  $\tau_{\omega_s}$ . With these SFTs, the main challenge to deal with is obtaining a signal that could be associated with gravitational radiation. In other words, a detection is associated with the possibility of distinguishing a signal ‘buried’ in noisy data. This detectable signal will be the one that exceeds a certain threshold that depends on the properties of the noise in

which the signal is buried and also on some prior knowledge of the signal.

## 4.2 Matched Filtering

Matched filtering is a technique in data analysis that looks for correlations between a template generated with features of a particular signal and patterns in noisy data in order to detect the presence of such a signal that fits the template. To construct an accurate template, prior knowledge of the signal is essential. In the context of gravitational wave detection, this knowledge involves not only intrinsic features of a signal, but also characteristics of this signal that depend on the detectors, such as the position on the Earth where the detection is done, called the *antenna patterns*, and the sky position of the sources. In this study, the template is constructed using the signal criteria shown in chapters 2 and 3, and the selection of an appropriate correlation between the template and a signal.

### 4.2.1 Signal-to-noise ratio of transient signals

In the frequency domain, a threshold that is useful to validate the detectability of a signal is related to the ratio between the signal amplitude and the noise amplitude at the signal frequency. This threshold parameter is called the signal-to-noise ratio (SNR) and is defined as the ratio of the signal power to the noise power. This principle is often used in the frequency domain in order to visualise the power of a signal through its power spectral density (PSD), which describes how the power in the time-series is distributed along the frequency range. This relationship is also the starting point of many of the tools that are commonly used to validate the recovery of a signal. A typical

way to estimate the SNR is through the so-called *optimal SNR*,  $\rho_{\text{opt}}$ , given by

$$\rho_{\text{opt}}^2 = 4 \int_0^\infty \frac{|\tilde{h}(f)|^2}{S_h(f)} df, \quad (4.2)$$

where  $\tilde{h}(f)$  is the Fourier transform of the signal  $h(t)$ , and  $S_h(f)$  is the single-sided PSD of some noise  $S_h(t)$ . With the use of the equations in chapter 3, the necessary parameters to model  $h(t)$  can be calculated. The estimate of  $S_h$  depends on either the noise floor of current detectors at a specific frequency or on the estimate of the sensitivity curves for future detectors like ET (figure 1.3(b)).

### 4.2.2 $\mathcal{F}$ -statistic in long transient gravitational wave searches

In [75], Jaranowski, Królak and Schutz proposed the use of a parameter called the  $\mathcal{F}$ -statistic that uses the principle of maximum likelihood probability to reach the detection goal, through the knowing of the parameters of the data. This method, originally conceived for the search of continuous gravitational waves, uses the matched filtering technique to estimate this probability taking into account several variables of which a gravitational wave signal depends on. Amongst these variables two kinds can be distinguished. First, the position of the detectors on the Earth and their relative positions to a source in the sky, called the *doppler parameters* and denoted in this work with  $\lambda$ . These parameters determine the time evolution of the gravitational wave phase and are expressed as  $\lambda \equiv \{\hat{n}, f^{(s)}(\tau_{ref})\}$ , where  $\hat{n}$  is the source sky position and  $f^{(s)}(\tau_{ref})$  is the evolution of the signal frequency with time with respect to a reference time  $\tau_{ref}$ , where  $^{(s)}$  denotes the time derivatives. Second, the intrinsic characteristics of the gravitational wave signal such as the polarisa-

tion, the frequency and the amplitude, called the *amplitude parameters* and denoted as  $\mathcal{A}^\mu \equiv \{h_0, \iota, \psi, \phi_0\}$  ( $\mu = 1, \dots, 4$ ), where  $h_0$ ,  $\iota$ , and  $\psi_0$  are the initial amplitude of the signal, the inclination angle and the polarisation angle, respectively, which were discussed in detail in chapter 3, and  $\phi_0$  is the initial phase of the gravitational wave signal. In [1], Prix, Giampanis and Messenger extended the use of the  $\mathcal{F}$ -statistic by proposing a method for transient signals. The parameters for these type of signals, called the *transient parameters* and denoted with  $\mathcal{T}$ , are related to the duration of the signal and the way the signal evolves with time. Thus, the transient parameters are expressed as  $\mathcal{T} \equiv \{\bar{\omega}, \tau, t_0\}$ . Together, these three new parameters model a window function in which  $\bar{\omega}$  rules how the signal decays with time,  $\tau$  is the damping time of the signal and  $t_0$  is the initial time.

In summary, the transient gravitational wave signal is expressed as

$$h^X(t; \mathcal{A}, \lambda, \mathcal{T}) = g_{\bar{\omega}}(t; t_0, \tau) \mathcal{A}^\mu h_\mu^X(t; \lambda) \quad (4.3)$$

which is based on the form of a CW, but with the extra transient parameters included. Here, the summation over the four amplitudes is implicit and  $\mu = 1, \dots, 4$ ,  $X$  is an index over the different gravitational wave detectors and  $g_{\bar{\omega}}$  is the transient window function. Also, the set of parameters that model the signal can be expressed as  $\theta \equiv \{\mathcal{A}, \lambda, \mathcal{T}\}$ .

Under the data analysis algorithm library tools of the LVC, there is a set of codes called the LAL/LALApps. Amongst these codes, there are some that calculate the  $\mathcal{F}$ -statistic, each one focused on different types of gravitational wave sources and detection methods. One of the versions of these codes, `lalapps.ComputeFStatistic_v2` (CFSv2), differs from other versions in mainly two aspects: the possibility of making an analysis considering more than one gravitational wave detector and the inclusion of the transient pa-

rameters. The description of the code in this thesis is focused on the second aspect, and the searches are performed considering only one detector. The code follows the same logic as the method proposed by Prix et al, in which the already existing analysis for CW signals is restricted in time by the inclusion of a transient window. A more detailed explanation of how transient gravitational wave signals are simulated and analysed is presented in this chapter in section 4.4.

### 4.3 Heterodyning

Long transient signals might carry some difficulties to be computed due to the amount of data needed to model them accurately. Heterodyning is a method to reduce the amount of data needed to model a long signal without compromising its accuracy. The name comes from the greek *hethero* (different) and *dyn* (power). In general terms, it is the generation of new signals by combining two oscillating wave forms. Nowadays it has many applications. For example, an electromagnetic wave that carries information of a signal (amplitude, frequency and phase) can transfer this signal, with all its information, to a new carrier by mixing the original signal with a sinusoidal wave at a different frequency (the heterodyne signal). This resultant signal will have a new frequency called ‘*beat frequency*’<sup>1</sup> that is the result of the difference between the original signal frequency and the sinusoidal one.

In the context of this work, heterodyning is used to simplify the computation of long duration transient gravitational wave signals. These simplifications can be seen as a reduction of the signal frequency and, according to the

---

<sup>1</sup>This name is given because of the similarity with the acoustic phenomenon of the same name in which an interference between two sounds of different frequencies causes a variation in volume.

Nyquist theorem, a reduction in the sampling frequency. This new signal will still carry all the information of the non-heterodyned signal and will need less computing power to be created or analysed. On the other hand, from the perspective of the frequency domain this process allows to focus an analysis of this new signal to a narrow frequency band around the beat frequency, reducing computing costs as well.

Generally, the steps to follow in an heterodyning process of a signal are:

- Get a simulated or real signal (figure 4.1 a).
- ‘Mix’ this signal with the *heterodyne* signal (figure 4.1 b, c).
- Filter the mixed signal and resample (figure 4.1 d).

### Simulation of the signal

There are many ways to simulate a signal. The main elements that are needed to construct a signal are the frequency and the duration. When a long signal is considered, in addition to the heterodyning process, a segmentation of this signal is advised in order to make the process more efficient. The challenge that comes with this segmentation is that, after an heterodyning process, these pieces must be attached back to the original signal without losing information. Also, when these pieces are put back together an overlapping must take place in order to avoid border effects due to filtering implementations.

### Mixing

The mixing is done by multiplying, in the time domain, the function that defines the signal with an oscillating signal with heterodyning frequency  $\omega_h$ . The exponential representation of the heterodyning function can be written

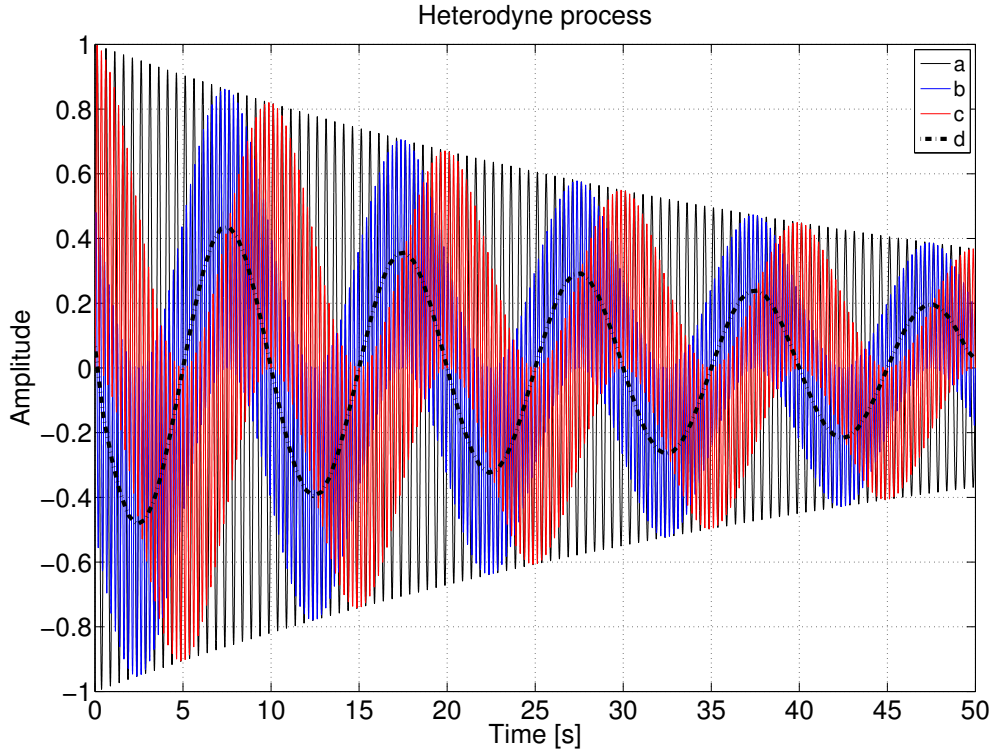


Figure 4.1: **Heterodyning process in the time domain.** This figure shows a comparison of the steps during a heterodyning process applied to a ring down simulated signal with an initial amplitude  $h_0 = 1$ , a damping time  $\tau = 50$  s and a signal frequency  $\omega = 1$  Hz. a) is the original signal, b) and c) are the real and imaginary parts of the signal after the mixing process, and d) is the resulting signal after a low pass filter is applied and a resampling takes place.

as

$$x_{re} = \frac{e^{i\omega_h} - e^{-i\omega_h}}{2}, \quad x_{im} = \frac{e^{i\omega_h} - e^{-i\omega_h}}{2i} \quad (4.4)$$

where  $x_{re}$  and  $x_{im}$  are the real (figure 4.1 b) and imaginary (figure 4.1 c) parts, respectively. It is important to use this function with these two parts separated because the result of this heterodyning process is a complex function. Then, as described above, the resulting frequency of the mixed signal  $\omega_{mix}$  is the difference between the signal frequency  $\omega$  and  $\omega_h$ . This new signal,  $x_{mix}$ , has to be completely equivalent to the original signal. An aspect shown with these multiplications is that the resulting functions have an attenuation of half the original amplitude and the real part is out of phase by  $\pi/2$ .

These functions are expressed as:

$$x_{mix} = \frac{A}{2} x \cos[t(\omega_h - \omega + \pi/2)] e^{-t/\tau}, \quad x_{mix} = \frac{A}{2} x \cos[t(\omega_h - \omega)] e^{-t/\tau} \quad (4.5)$$

The attenuation is more evident after the filter implementation.

### Filtering and Resampling

The mixed signal  $x_{mix}$  has implicit two frequencies,  $\omega$  and  $\omega_h$ . The first one is always greater than the second one. The filter commonly used is a low pass filter (LPF) with an appropriate cutoff frequency. For example, in figure 4.1 a Butterworth filter was applied. The main issue to consider when designing a filter is to select an adequate cutoff frequency. This is the frequency at which the magnitude of the response of the filter is  $\sqrt{1/2}$ . In other words, this cutoff frequency has to be the one that lets through only the information to build the signal without aliasing it and is constructed as

$$f_{\text{cutoff}} = \frac{f_s^0}{0.5 \times r_s} \quad (4.6)$$

where  $f_s^0$  is the original sampling frequency and the resampling factor  $r_s$  is the number of samples in the original sampling frequency which are discarded. After the implementation of the filter, and before the resampling, the real and imaginary parts have to be joined. After the resampling the overlapping sections (if the signal was fragmented in pieces) have to be eliminated.

### Frequency domain

So far, the heterodyning process has been described as it is in the time domain. Gravitational wave data are generally analysed in the frequency domain, and so it is more convenient to show the output of this technique in the same

form. In order to verify that no aliasing happened during the process, the heterodyned signal needs to be compared to a *template* which is obtained by applying a transformation to the time domain function. This transformation is the **F**ast **F**ourier **T**ransform (FFT) and it is applied to the heterodyned data. An example of a template, taken from [76], is of the form:

$$s = \frac{A^2\tau^2}{1 + (\Delta\omega - \omega_0)^2\tau^2} \quad (4.7)$$

where  $\Delta\omega$  is the frequency range of the data in which the signal is going to be searched for and  $\omega_0$  is the central frequency of the signal. Once this template fits with the final product of the heterodyning process, a signal can be validated (figure 4.2). In the context of the frequency domain, the most important consequence of applying an heterodyning process is that the parameter space in which a match filtering (or match template) search is performed is significantly reduced. This is because this parameter space is a function of the sampling frequency of the signal which is reduced.

## 4.4 Search for long transient gravitational waves in simulated data

Two steps can be distinguished in the search for long transient gravitational waves. The generation of data, that could be either simulated or real, and the analysis of these data in which the aim is to obtain information buried in noise. In this section, the generation of gaussian noise and the strategy followed to do the analysis centred on long transient gravitational waves is presented. Posterior to this, what was learnt with this method is applied to non-gaussian simulated data. This second analysis is presented in chapter 5.

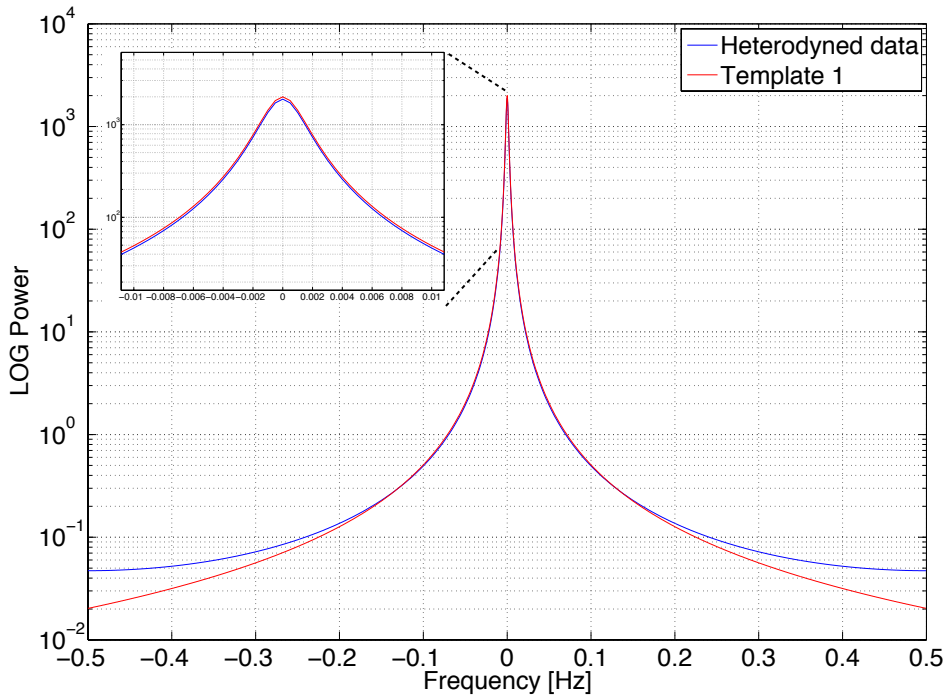


Figure 4.2: **Heterodyning result in the frequency domain.** This plot shows how heterodyned data should fit a template, in order to be reliable in an analysis.

#### 4.4.1 Data generation and signal injections

In data analysis, the simulation of data is the act of joining together signals and noises. A strategy to solve the problem of recovering a signal buried in noise using a specific tool is to know well, prior to the analysis, both the noise and the signal in order to obtain the expected results. The most used type of noise, due to its simplicity, is the Gaussian noise which has a mean  $\mu = 0$  and variance  $\sigma^2 = 1$ . The probability density function (PDF) of this distribution is given by

$$\text{PDF} = \frac{1}{\sigma\sqrt{2\pi}} e^{-\frac{(x-\mu)^2}{2\sigma^2}} \quad (4.8)$$

in which  $\mu$  is the mean of the distribution,  $\sigma$  is the standard deviation and  $x$  are the data.

### Signal injections

The first part of the analysis was done with simulated data generated using existing tools in the LAL/LALApps algorithm libraries.

`lalapps_Makefakedata_v4` (Mfdv4) is a code that was originally created for continuous waves analyses of gravitational wave signals from pulsars. In table 4.1, the commands used to do the injections, as well as their description, are shown. This information could be useful for the reproduction of the data and results presented in this thesis. For example, the `startTime` of the signal, which sets the beginning of the data, and the `refTime`, which is the starting point of the analysis, were selected to be the same and were set up based on the antenna patterns of the detector. The intention is to match the largest value of `h0` to the GPS time that attenuates it the least.

The main difference with respect to previous versions of this code is the addition of  $\mathcal{T}$  parameters such as `transientWindowType`, `transientStartTime`, and `transientTauDays`, which refer, respectively, to the type of window  $g_{\bar{\omega}}$ , the initial GPS time of the window and the duration  $\tau$  of the window. Currently there are three options defined to select the window type: `none`, `rect` and `exp`. The trivial option `none`, avoids the inclusion of a window  $g_{\bar{\omega}}$  in the data generation process. The other options are modelled as

$$g_r(t; t_0, \tau) \equiv \begin{cases} 1, & \text{if } t \in [t_0, t_0 + \tau]. \\ 0, & \text{otherwise.} \end{cases} \quad (4.9)$$

if the rectangular window (`rect`) is considered, and

$$g_e(t; t_0, \tau) \equiv \begin{cases} e^{-(t-t_0)/\tau}, & \text{if } t \in [t_0, t_0 + 3\tau]. \\ 0, & \text{otherwise.} \end{cases} \quad (4.10)$$

which models the exponential decay window (`exp`). The arbitrary truncation of the duration of  $g_{\omega}$  is set at a point in which the attenuation of the initial amplitude  $h_0$  due to the exponential function is around 5% and, in consequence, does not contribute to a loss of the SNR. A comparison of these windows is shown in figure 4.3.

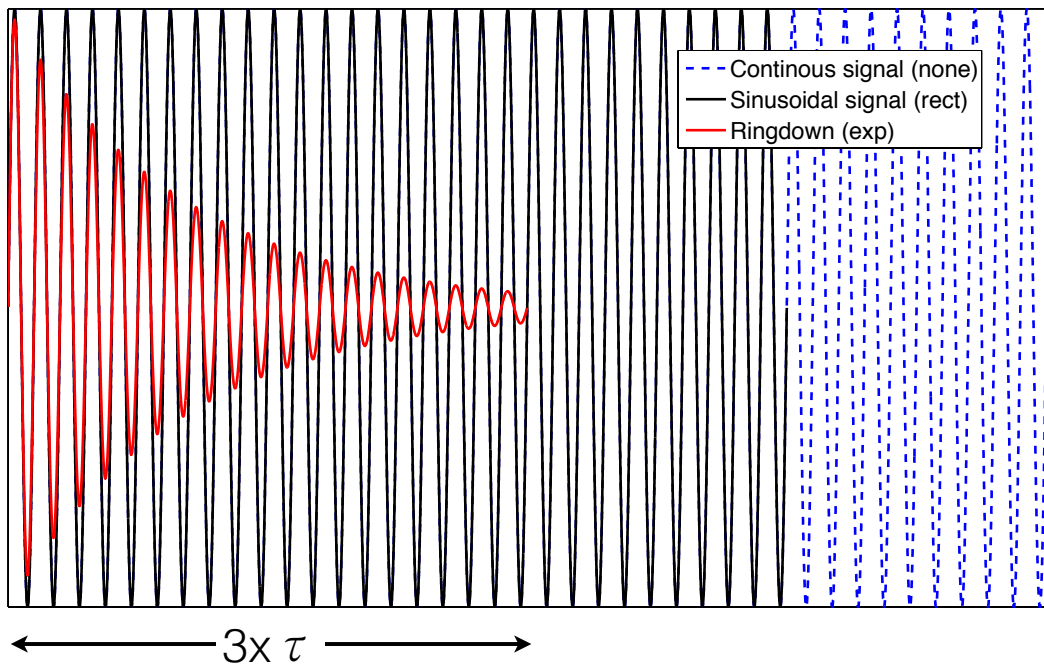


Figure 4.3: **Transient windows with Mfdv4.** The three different window options provided by the `Mfdv4` code to construct a transient signal are shown in this figure. The trivial option `none` is shown in dashed lines in comparison with the `rect` window (black) that does not depend on  $\tau$  and the `exp` window (red) which is truncated at  $3\tau$ .

Table 4.1: **Commands of the `lalapps.Makefakedata.v4` code used in this work.** The usage of `Tsft` is very important to model an appropriate transient signal to be analysed correctly. The discussion about this command is presented in this section. \*Refer to figure 3.1(a).

Mfdv4 command	Description
IFO	GW Detector
ephemDir ephemYear	Utilities to set up the ephemerides to be used
startTime	Signal's start time in GPS time. Selected to maximise $h_0$ with respect to antenna patterns.
duration	Duration of the signal in seconds. This should not be confused with <b>transientTauDays</b>
fmin	SFT's lowest frequency (= heterodyning frequency)
Band	SFT's Bandwidth (half the sampling frequency)
Tsft	SFT's time baseline
refTime	This time should be within the interval of the signal. For simplicity, in this work, it has been set to be the same as the <b>startTime</b>
Alpha	Right Ascension of the star (radians)
Delta	Declination of the star (radians)
h0	Signal's initial amplitude
cosi	cos of inclination angle $\iota$ (Set to zero to maximise $h_0$ )*
psi	polarisation angle $\psi$ (Set to zero to maximise $h_0$ )*
f1dot f2dot f3dot	Time derivatives of the frequency. Not used in this work due to unavailability of data
orbit	Parameters used for long duration signals in binary systems
noiseSqrtSh	square root of (Sh) (noise level)
transient	Parameters that refer to the transient window, duration and initial time
generationMode	To generate separate SFT files or all in one
randSeed	To generate seeded noise that could be reproduced

As mentioned earlier, `Mfdv4` is an adaptation from other codes to inject continuous gravitational wave signals (CW). In those codes, a decay in the amplitude of the signal was not considered and the analysis done by the  $\mathcal{F}$ -statistic estimator codes assumed that the initial amplitude  $h_0$  is constant (see section 4.4.2). Since this is not the case for ring down signals, an adaptation to the CW analysis of these signals when `transientWindowType = exp` has to be done. If small enough pieces of a ring down signal are analysed separately, a good approximation of this analysis to a CW analysis can be done. This approximation is shown in figure 4.4. In terms of the `Mfdv4` code there is a command, `Tsft`, that sets the length of data in time used when the SFTs are performed. In other words, the time-range defined by the  $\tau_\omega$  in equation 4.1 is set as small as it is convenient. The integration of the output of the analysis all over the signal, in the time domain, is done by integrating the combining all SFTs which are function of time.

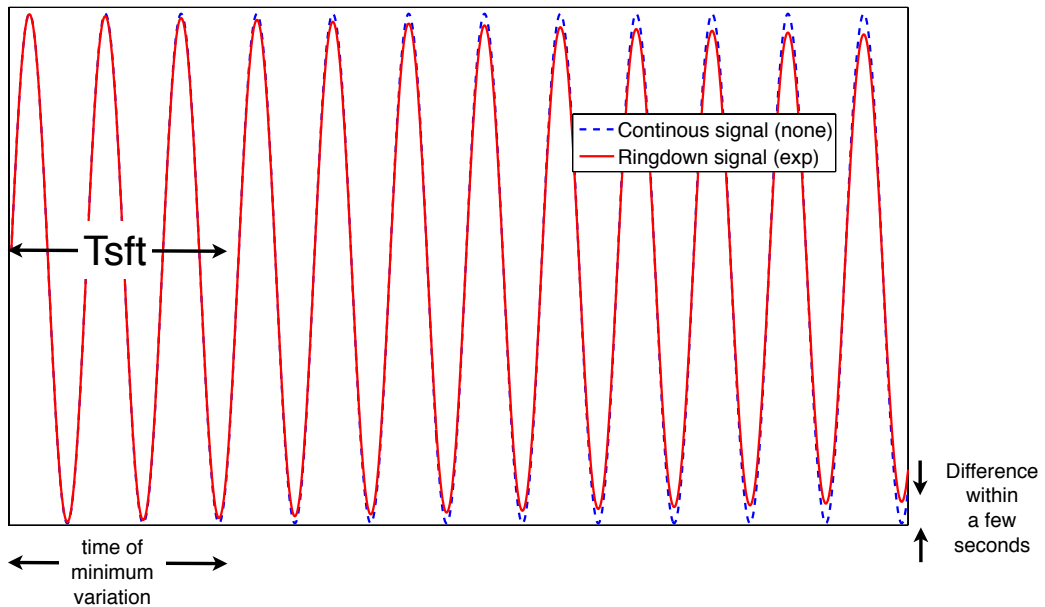
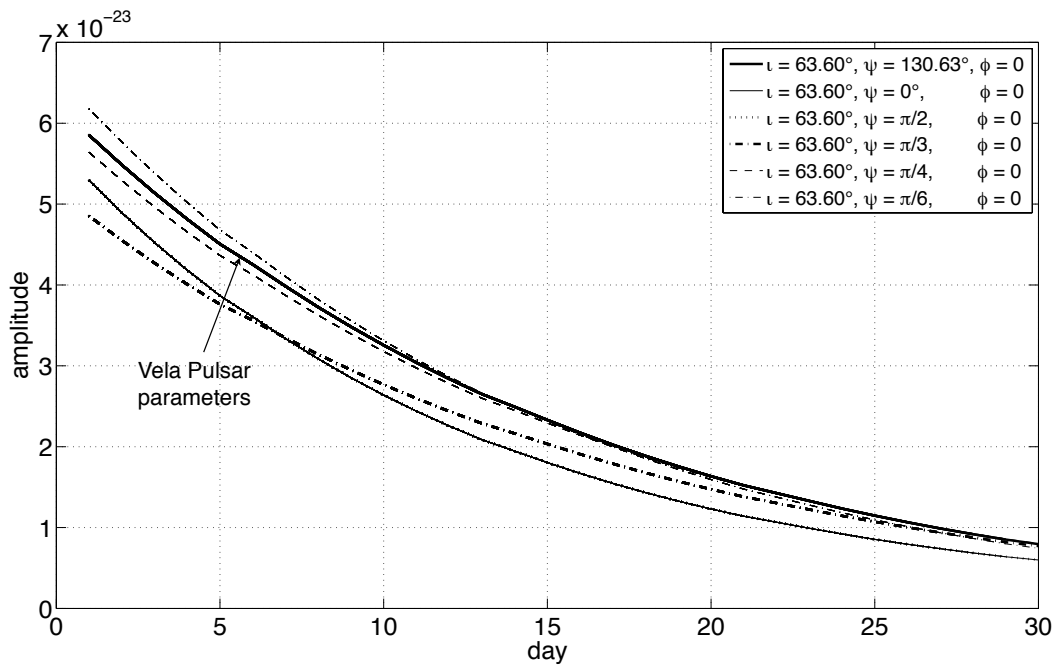


Figure 4.4: **Transient signal adaptation of the CW analysis.** In order to use the infrastructure developed for the analysis of CW, the command `Tsft` is used to split the signal data in small pieces so they can be analysed separately as CW signals. This separation is done by simulating many short SFTs of a specific time `Tsft`.

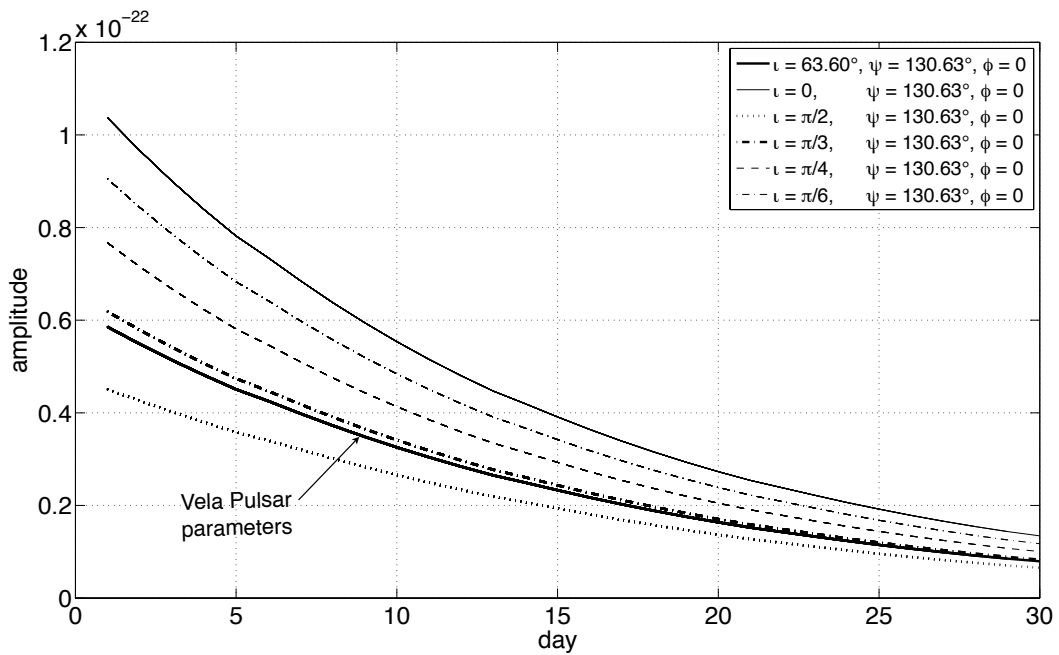
In addition to the  $\mathcal{T}$  parameters, `Mfdv4` also takes into account  $\lambda$  and  $\mathcal{A}^\mu$  parameters. In the context of this work, the  $\lambda$  parameters are known from electromagnetic observations of pulsars. The time evolution of the frequency, when known, is very small and could cause a change in the modelling of the signal. When a long duration signal is injected, the orbital parameters of the star have to be considered if the duration of the signal is comparatively large with respect to the orbital period in a binary system.

On the other hand, the amplitude parameters  $\mathcal{A}^\mu$  have a more significant effect on the signal, particularly the orientation angles  $\iota$  and  $\psi$ , described in chapter 3, and the phase  $\phi$ . Depending on the values of these angles, the time evolution of the signal changes. A study to show this variation was done using different values of these angles in long duration transient signals that decay exponentially. As a reference, the parameters of the Vela Pulsar  $\iota \approx 63.60^\circ$  and  $\psi \approx 130.63^\circ$  were used [25].

As shown in figure 4.5, the evolution of the signal in the time domain over 30 days varies differently when the angle  $\iota$  is fixed than when the angle  $\psi$  is fixed. From this study, the fact that the variation in the polarisation angle  $\psi$  is less significant to the variation of the amplitude of the signal than the variation of the inclination angle  $\iota$ , was learnt. And also, the effect of the variation of  $\iota$  is more significant at the beginning of the exponentially decaying signal than at the end.



(a)



(b)

Figure 4.5: **The effect of the polarisation angle  $\psi$  and the inclination angle  $\iota$  on a signal simulated with Mfdv4.** As a reference, the values of the Vela Pulsar of these two angles are presented. (a) The variation of  $\psi$  with  $\iota$  fixed and  $\phi = 0$ . (b) The variation of  $\iota$  with  $\psi$  fixed and  $\phi = 0$ . In this case  $\phi = 0$  means that there is no variation on the phase of the signal frequency.

### 4.4.2 Gravitational wave search methodology

Following the methodology proposed by Prix et al in [1], a detection of a long transient signal in some noisy data can be expressed mathematically as the ratio of two likelihoods. The first likelihood refers to some hypothesis  $\mathcal{H}_G$  in which the data contains only (gaussian) noise and the second likelihood  $\mathcal{H}_S$  of some data composed of noise and an injected signal. The likelihood for some data  $x$  in the noise only case is written as

$$P(x|\mathcal{H}_G) = \kappa e^{-(1/2)(x|x)} \quad (4.11)$$

with a normalisation constant  $\kappa$  and where

$$(x|x) \equiv 2 \sum_X S_X^{-1}(f) \int x^X(t) x^X(t) dt \quad (4.12)$$

in which  $S_X(f)$  is a stationary single-sided noise PSD in a particular detector  $X$ . Now, if a signal  $h(t;\theta)$  is injected, the likelihood is written as

$$P(x|\mathcal{H}_S, \theta) = \kappa e^{-(1/2)(x-h(\theta)|x-h(\theta))} \quad (4.13)$$

given the fact that the noise can be expressed as  $n = x - h(\theta)$ . Then, the likelihood ratio of these is

$$\mathcal{L}(x; \theta) \equiv \frac{P(x|\mathcal{H}_S, \theta)}{P(x|\mathcal{H}_G)} = e^{(x|h(\theta)) - (1/2)(h(\theta)|h(\theta))} \quad (4.14)$$

After inserting the transient gravitational wave signal model in equation 4.3, it takes the form of

$$\log \mathcal{L}(x, \theta) = \mathcal{A}^\mu x'^\mu - \frac{1}{2} \mathcal{A}^\mu \mathcal{M}'_{\mu\nu} \mathcal{A}^\nu \quad (4.15)$$

where

$$x'_\mu(\lambda, \mathcal{T}) \equiv (x|h'_\mu) \quad (4.16)$$

and

$$\mathcal{M}'_{\mu\nu}(\lambda, \mathcal{T}) \equiv (h'_\mu|h'_\nu), \quad (4.17)$$

define the template to be used in the search. If a maximisation over the likelihood ratio is done, the maximum likelihood statistic could be expressed as

$$\ln \mathcal{L}_{\text{ML}}(x) = \max_{\lambda, \mathcal{T}} \mathcal{F}(x; \lambda, \mathcal{T}) \quad (4.18)$$

where  $\mathcal{F}$  is the  $\mathcal{F}$ -statistic. The long transient  $\mathcal{F}$ -statistic then is expressed explicitly as

$$2\mathcal{F}(x; \lambda, \mathcal{T}) \equiv x'_\mu \mathcal{M}'^{\mu\nu} x'_\nu \quad (4.19)$$

This  $2\mathcal{F}$  follows a  $\chi^2$  distribution with four degrees of freedom and non-centrality parameter  $\rho_{\text{opt}}^2$ , i.e.,

$$E[2\mathcal{F}] = 4 + \rho_{\text{opt}}^2 \quad (4.20)$$

### 4.4.3 Performing a search for long transient gravitational waves

Once the signal is modelled and injected in noise, the analysis is performed. In the first part of this work, `Mfdv4` is used to inject long transient signals in white gaussian noise. As for the injection code, `lalapps-ComputeFStatistic.v2` (`CFSv2`) is an adaptation from previous versions for long transient gravitational wave signal analyses which is based on the methodology described on section 4.4.2. A description of the commands of this code used in this work is presented in table 4.2. An important aspect of performing gravitational wave

searches using `CFSv2` is that the parameters used in the command line should be consistent between both the injection and the analysis code. This consistency is not only important in terms of the location or physical parameters of the source, but also in the search bands in which the analyses are performed. They should be set up within the region where a signal is available in the data. Also, when these search bands are performed, it is important to consider that they are related to the uncertainty in finding the parameter under study. If during an analysis, a search band, either in frequency or in time, is not defined in the command line of the `CFSv2` code but the initial value of this parameter is, the analysis is performed only for that individual value.

The adaptations of `CFSv2` are focused on the transient parameters  $\mathcal{T}$ . Particularly, the command `transient_WindowType` is set to let `CFSv2` know the type of window used to construct the signal, using `Mfdv4` for example, and in consequence the type of window that has to be used to create the template. Prix et al showed in [1] that the variation in the output of the code, using either a `rect` or an `exp` window, is small. On the other hand, the computing efficiency is better if a `rect` window is used in the analysis regardless if the evolution of the signal is rectangular or decays exponentially. This is consistent with the discussion of `Tsft` given in section 4.4.1, because the analysis could be performed in small pieces of data in the same way as in a CW analysis. The other commands related with the  $\mathcal{T}$  parameters in `CFSv2` are `transient_t0Days`, the initial time of the transient signal, `transient_t0DaysBand`, that sets a search interval based on the uncertainty of the transient initial time, `transient_tauDays`, the smallest value of the search band of the transient signal duration, and `transient_tauDaysBand`, which sets the length of the search interval around  $\tau$  and, in consequence, the uncertainty in finding this number.

Table 4.2: **Commands of the `lalapps_ComputeFStatistic.v2` code used in this work.**

CFSv2 command	Description
Alpha	Right Ascension of the star (radians)
Delta	Declination of the star (radians)
AlphaBand	Band in Alpha (radians)
DeltaBand	Band in Delta (radians)
Freq	Starting search frequency in Hz.
FreqBand	Frequency search band Hz.
f1dot f2dot f3dot	Time derivatives of the frequency. Not used in this work due to unavailability of data
f1dotBand f2dotBand f3dotBand	Band in time derivatives of the frequency. Not used in this work due to unavailability of data
orbit	Parameters used for long duration signals in binary systems
IFO	GW Detector
ephemDir ephemYear	Utilities to set up the ephemerides to be used
TwoFthreshold	Threshold to calculate 2F Useful to optimise time of analyses
refTime	This time should be within the interval of the signal. For simplicity, in this work, it has been set to be the same as the <code>startTime</code>
minStartTime	Earliest SFT time to include in the search.
maxEndTime	Latest SFT time to include in the search.
transient_WindowType	Type of transient signal window to use.
transient_t0Days	Start-time for transient window search, as offset in days from <code>dataStartGPS</code>
transient_t0DaysBand	Range of GPS start-times to search in transient search, in days
transient_dt0	Step-size for search/marginalization over transient-window start-time, in seconds [Default:Tsft]
transient_tauDays	Shortest transient-window timescale, in days
transient_tauDaysBand	Range of transient-window timescales to search, in days
transient_dttau	Step-size for search/marginalization over transient-window timescale, in seconds [Default:Tsft]

The outputs of CFSv2 in which this work is focused on, are the  $\mathcal{F}$ -statistic, which is calculated per frequency bin and that is called  $2\mathcal{F}$ , and the maximum value of the calculation of the  $\mathcal{F}$ -statistic over a  $\tau$  search band per frequency bin, which is called  $\max 2\mathcal{F}$ . In other words, the inclusion of the duration of the signal gives a new element to maximise, within the search interval in time, the  $\mathcal{F}$ -statistic. To illustrate this search method, a schematic representation of the functionalities of the code are shown in figure 4.6.

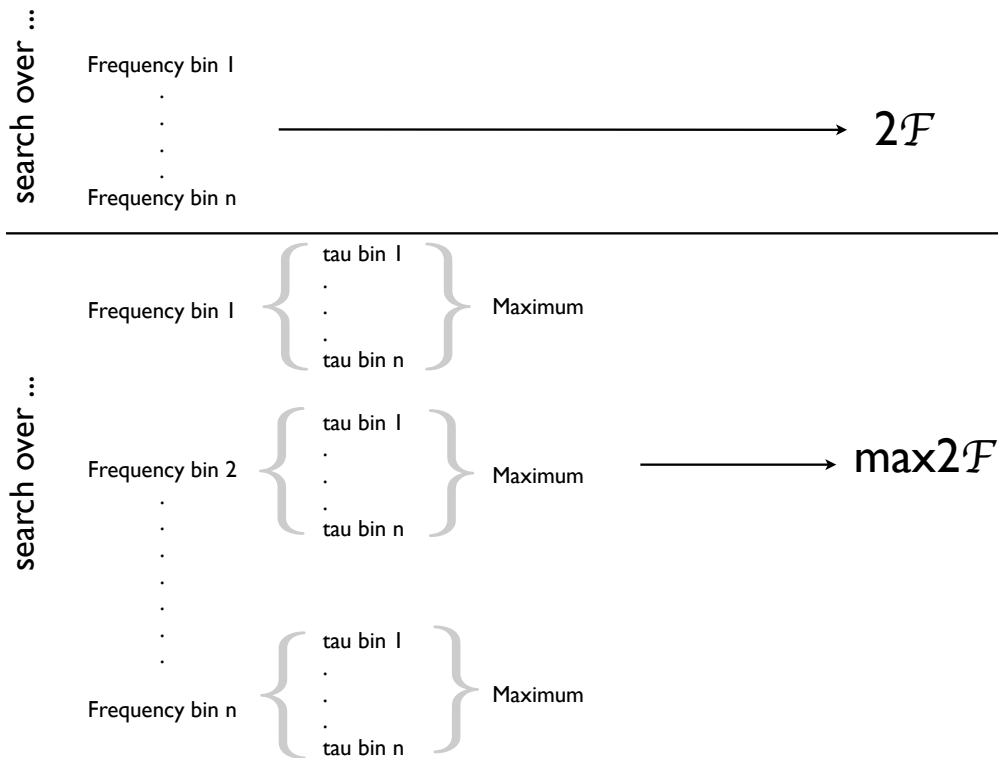


Figure 4.6: **Search method of CFSv2.** This figure illustrates the difference between the calculation of  $2\mathcal{F}$  and  $\max 2\mathcal{F}$ . When calculating  $2\mathcal{F}$ , the search method is done only over a frequency search band which is defined from the command line. On the other hand, for  $\max 2\mathcal{F}$  the code performs a search over a time interval around the estimated duration of the signal in each frequency bin on the frequency search band. When each time-related search is done at a specific frequency bin, the maximum value of this search is selected as the best estimate of  $2\mathcal{F}$  of the frequency bin in question.

#### 4.4.4 Results

With all this prior knowledge of the signal detection statistics which are the output of CFSv4, a series of experiments to characterise this output were done. A first experiment had the aim of comparing  $2\mathcal{F}$  with  $\max 2\mathcal{F}$  given different search bandwidths of  $\tau$  and in frequency. The resulting plots of this experiment are shown in figure 4.7. From there, the increment on the amplitude of the statistic at the signal frequency when  $\max 2\mathcal{F}$  is used, is shown.

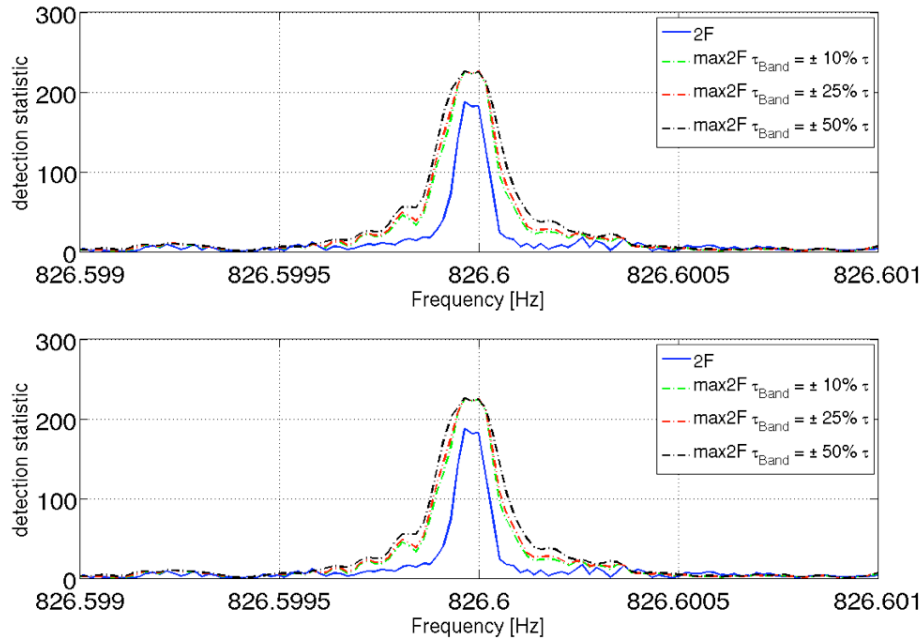


Figure 4.7: Comparison of CFSv2 output  $2\mathcal{F}$  and  $\max 2\mathcal{F}$  in a frequency band of 0.1 Hz (top) and 1Hz (bottom). This is a zoom in an image into the CFSv2 spectrum around the injected signal frequency.

Also, despite the fact that the bottom panel is the result of a 10 times longer frequency search band than the top panel, it is important to notice that the statistic is almost identical. This suggests that, in terms of recovering the injected signal frequency, this method is efficient. The parameters of the signal used in this experiment were initial estimates for the source PSR 4U1608–522, where an unmodified  $\tau_{vbl}$  was considered. This is, using similar equations to

the ones described in section 3.5.1 assuming that the energy transferred to the gravitational waves came from Type I X-Ray Bursts. These estimates give values for  $\tau_{vbl}$  of  $9.27 \times 10^3$  s, an  $h_0 = 1.31 \times 10^{-25}$  from equation 3.37, and a frequency of 826.6 Hz calculated with equation 3.8. In order to get an entire signal for the analysis, the total length of the data processed was 28,800 s getting a signal a few seconds larger than  $3 \times \tau$ . Finally, the noise floor of  $5.65 \times 10^{-25} \text{ Hz}^{-1/2}$  was estimated using the predicted sensitivity of ET at the mentioned frequency.

As a second experiment, and in order to model the output of the signal detection, the distribution of the signal detection of several injections at different white noise realisations has to be done. The parameters of the signal used in this experiment are the ones associated with the source AMP 4U1608 -522 in table 3.2 of chapter 3. They are shown in table 4.3:

Table 4.3: **Parameters of the source used in the analysis.**

name PSR	Dist [Kpc]	Energy $\times 10^{41}$ [erg]	$f_{\text{star}}$ [Hz]	T [ $10^8$ K]	h0 $\times 10^{-25}$	$\tau$	$h_{\text{rss}}$	$\tau$	$h_{\text{rss}}$
						[s]	$\times 10^{-25}$	[s]	$\times 10^{-25}$
						$f_{\text{critical}} = 640 \text{ Hz}$		$f_{\text{critical}} = 730 \text{ Hz}$	
4U 1608-522	3.2	4.0	620.0	4.55	1.968	2309	94.60	300.7	34.13

In addition to the parameters shown in table 4.3, it is important to mention that the total duration of the signals is  $3 \times \tau$  and the signal frequency is estimated with equation 3.8. Also, these tests are done with a noise floor of  $5.65 \times 10^{-25} \text{ Hz}^{-1/2}$  which is estimated with the predicted sensitivity curve of ET at the signal frequency. These injections are done with the two  $f_{\text{critical}}$  criteria described in detail in section 3.5.3. In consequence, two different analyses for each criterium are presented, one for an  $f_{\text{critical}} = 640 \text{ Hz}$ , in which signals with  $\rho_{\text{opt}}^{f_{\text{crit}}=640} \approx 11.6$  are injected, and another one for an  $f_{\text{critical}} = 730 \text{ Hz}$  that is

done with signals with a  $\rho_{\text{opt}}^{f_{\text{crit}}=730} \approx 4.2$ . There are some aspects to highlight from the results of the analyses of these 500 injections, which are shown in figures 4.8 and 4.9:

- The frequency search band can be reduced to just a few frequency bins.
- The  $\tau$  search band has a very large dispersion and is inverse to the SNR.
- The distribution of the  $\text{max2}\mathcal{F}$  is of the form of a non-central  $\chi^2$  distribution with 4 degrees of freedom and non-centrality parameter  $\rho_{\text{opt}}^{f_{\text{crit}}}$ .
- The construction of the distribution of  $\text{max2}\mathcal{F}$  seems to be more difficult for small SNRs, as can be seen on figure 4.9.
- If the SNR is smaller, a broader frequency search band and  $\tau$  search band are needed.

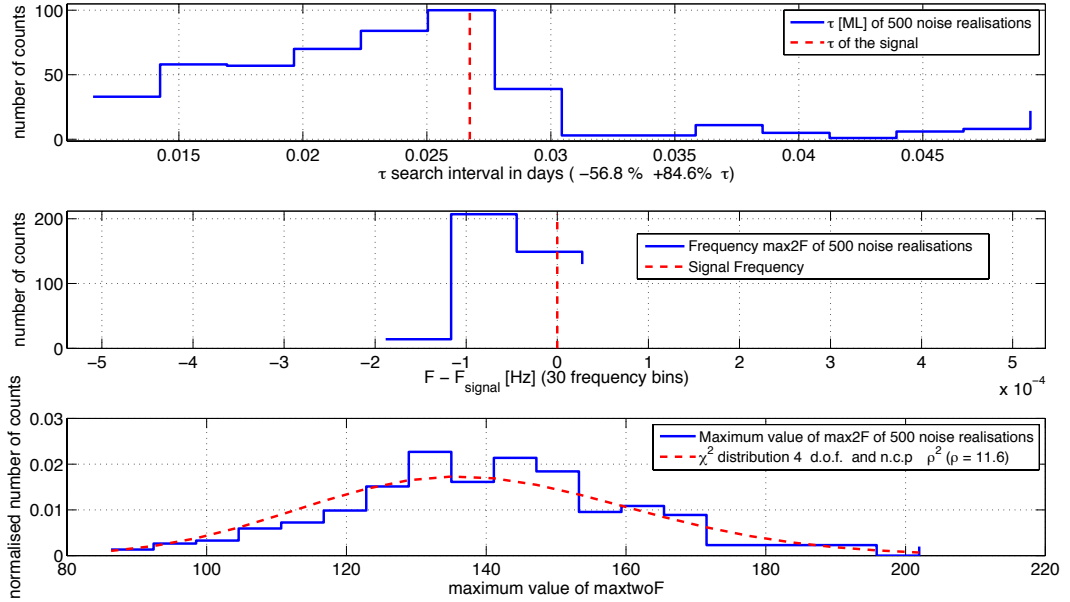


Figure 4.8: **Output distributions of  $\tau$  and  $f_{\text{signal}}$  associated with  $\text{max2}\mathcal{F}$  for signals of  $\rho_{\text{opt}}^{f_{\text{crit}}=640} \approx 11.6$ .** This figure shows the distributions of the signal duration associated with the maximum value of  $\text{max2}\mathcal{F}$  (top panel), the signal frequency associated with the maximum value of  $\text{max2}\mathcal{F}$  (middle panel) and the distribution of the statistic  $\text{max2}\mathcal{F}$  in 500 injections.

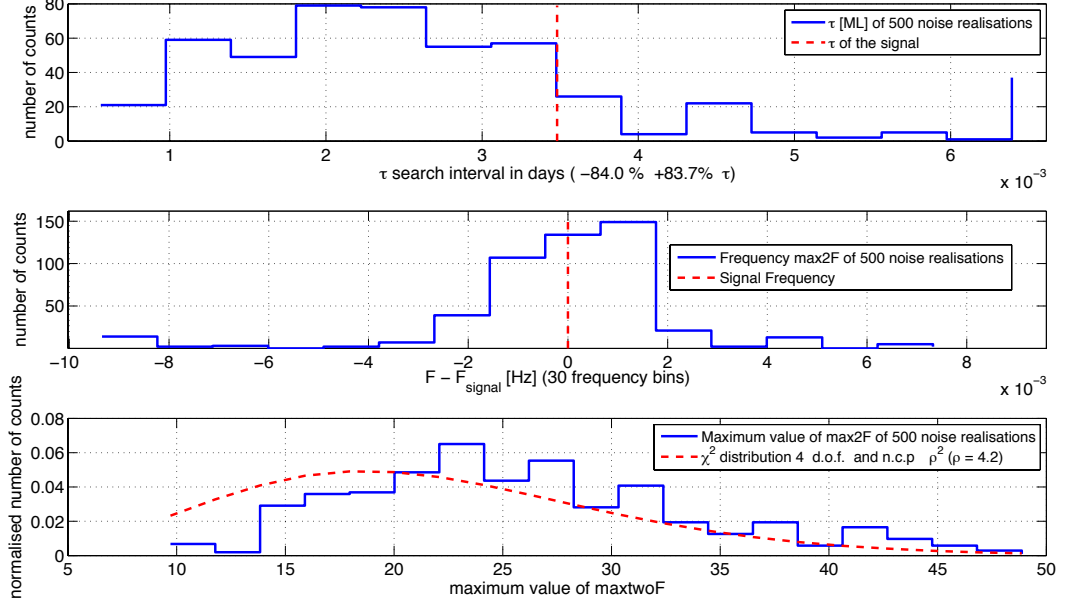


Figure 4.9: **Output distributions of  $\tau$  and  $f_{\text{signal}}$  associated with  $\text{max2}\mathcal{F}$  for signals of  $\rho_{\text{opt}}^{f_{\text{crit}}=730} \approx 4.2$ .** This figure shows the distributions of the signal duration associated with the maximum value of  $\text{max2}\mathcal{F}$  (top panel), the signal frequency associated with the maximum value of  $\text{max2}\mathcal{F}$  (middle panel) and the distribution of the statistic  $\text{max2}\mathcal{F}$  in 500 injections.

In order to test these aspects, other sets of 500 injections for each of the  $f_{\text{critical}}$  criterium were done, keeping all the parameters but the initial amplitude fixed. With this variation, the SNR of the signal is modified and the distributions are expected to change as well. The increment selection was set to be  $5 \times h_0$ . Figures 4.10 and 4.11 show the results of these signal injections with a  $5 \times$  larger  $h_0$  and in consequence a  $5 \times$  larger SNR. This brings to new values for the non-centrality parameter of  $5 \times \rho_{\text{opt}}^{f_{\text{crit}}=640} \approx 56.5$  and  $5 \times \rho_{\text{opt}}^{f_{\text{crit}}=730} \approx 21$ , respectively. The results of these additional analyses, shown in figures 4.10 and 4.11, have to be compared with the results in figures 4.8 and 4.9, respectively. This comparison shows how the distributions change with the increment of the initial amplitude  $h_0$ . It is particularly interesting to see that when a larger SNR is considered, the recovery of the signal frequency is limited to one frequency bin.

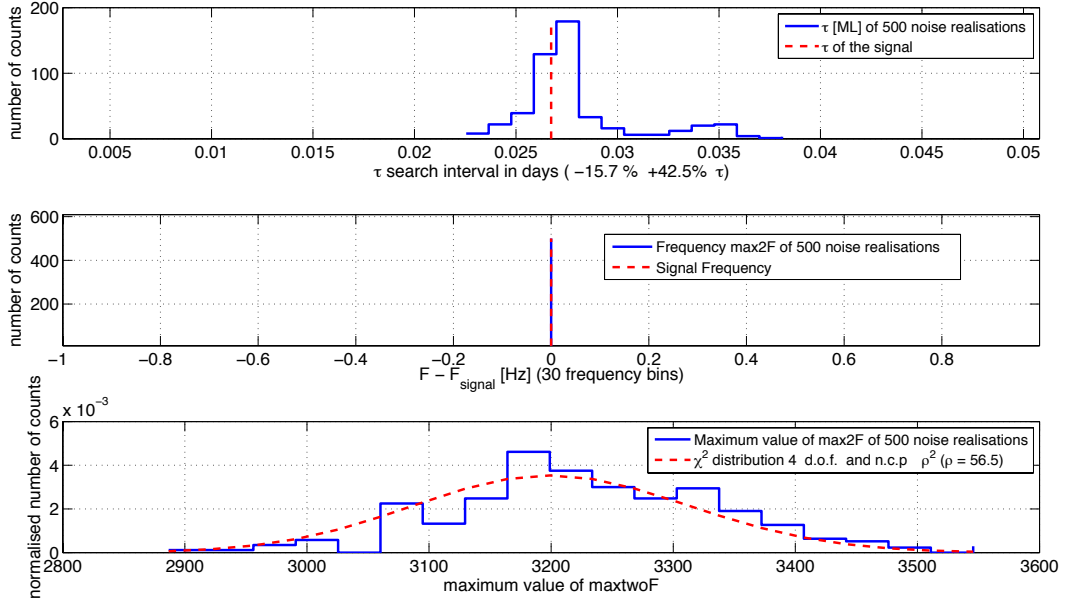


Figure 4.10: **Output distributions of  $\tau$  and  $f_{\text{signal}}$  associated with  $\text{max2}\mathcal{F}$  for signals with  $5 \times \rho_{\text{opt}}^{f_{\text{crit}}=640} \approx 56.5$ .** As in figure 4.8, this figure shows the distributions of the signal duration and the signal frequency associated with the maximum value of  $\text{max2}\mathcal{F}$  at the top panel and middle panel, respectively, and the distribution of the statistic  $\text{max2}\mathcal{F}$  in 500 injections.

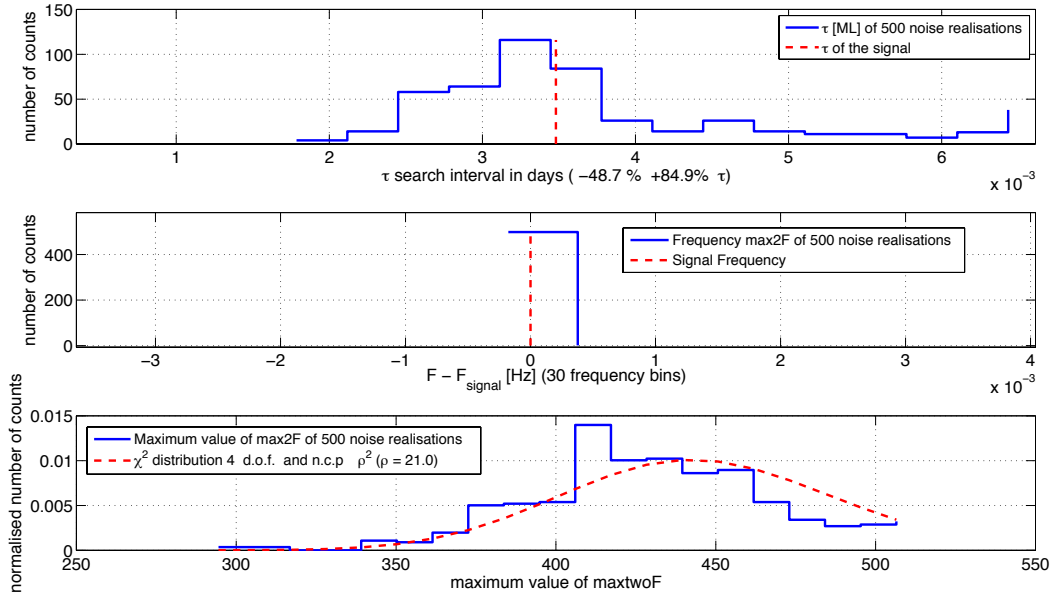


Figure 4.11: **Output distributions of  $\tau$  and  $f_{\text{signal}}$  associated with  $\text{max2}\mathcal{F}$  for signals with  $5 \times \rho_{\text{opt}}^{f_{\text{crit}}=730} \approx 21$ .** As in figure 4.9, this figure shows the distributions of the signal duration and the signal frequency associated with the maximum value of  $\text{max2}\mathcal{F}$  at the top panel and middle panel, respectively, and the distribution of the statistic  $\text{max2}\mathcal{F}$  in 500 injections.

This is, in the context of these 500 injections, all the maximum values of  $\max 2\mathcal{F}$  are at the frequency of the injected signal.

#### 4.4.5 Signal duration uncertainty

The importance of knowing how the duration of the signal associated with the detection statistic  $\max 2\mathcal{F}$  is distributed, can be explained from the Levin & Ushomirsky model equation described in section 3.2.3:

$$\frac{1}{\tau_{vbl}} \simeq 0.01 s^{-1} \frac{R_6^2 F^{1/2}}{M_{1.4} T_8} \frac{\rho_b}{\rho} \left( \frac{f_{\text{star}}}{\text{kHz}} \right)^{1/2} \left( \frac{\delta u}{u} \right)^2. \quad (4.21)$$

In this model the parameters  $(\delta u/u)^2$  and  $F^{1/2}$  are the most interesting because they are associated with rubbing effects in the crust-core interface and particle scattering in the interior of the NS, respectively, that could be related to the transfer of angular momentum from the fluid component to the crust. In addition, a relation of the uncertainty of the duration of the signal and the uncertainty on the physics inside the NS, assuming this model, can be obtained. Pulsar timing glitches can be related to this process.

Setting the rest of the components to be constants, the uncertainty on the product of these two parameters is related to the uncertainty on the duration of the signal. With these assumptions, this uncertainty is given by:

$$d \left( F^{1/2} \left( \frac{\delta u}{u} \right)^2 \right) = \mathcal{K} \frac{d\tau}{\tau^2} \quad (4.22)$$

with  $\mathcal{K}$  the set of all the parameters in the Levin & Ushomirsky model timescale equation but  $(\delta u/u)^2$  and  $F^{1/2}$ . The complete derivation of equation 4.22 is included in this work in appendix B.2.

The uncertainty on the duration of the signal  $d\tau$  for each set of injections is shown in table 4.4. This uncertainty is related with the uncertainty of the

$F^{1/2}$  and  $(\delta u/u)^2$  parameters. Also, the uncertainty of these parameters is related with the uncertainty of physical parameters of the star like the radius or the mass of the NS, since the combination  $F^{1/2}(\delta u/u)^2$  is in units of  $1.4M_\odot$ ,  $R_{11.7\text{Km}}$  and  $10^8\text{K}$ . For the purposes of this work, this uncertainty was calculated with a 90% confidence level. The methodology used for these calculations is detailed in appendix B.1. Also, the uncertainty on  $F^{1/2}(\delta u/u)^2$ , considering the value of  $F^{1/2}(\delta u/u)^2 = 0.968$  calculated in equation 3.62, was calculated using equation B.5.

Table 4.4: **Uncertainties on  $d\tau_{90\%}$  and  $F^{1/2}(\delta u/u)^2$ .** In this table the uncertainties on  $\tau$  have units of seconds. The uncertainties on the combination of  $F^{1/2}$  and  $(\delta u/u)^2$  are in units of  $1.4M_\odot$ ,  $R_{11.7\text{Km}}$  and  $10^8\text{K}$ .

$\rho_{\text{opt}}^{f_{\text{crit}}}$	$\tau_{-d\tau}^{+d\tau}$ [s]	$+d(F^{1/2}(\delta u/u)^2)$	$-d(F^{1/2}(\delta u/u)^2)$
4.2	$300.7^{+369.8}_{-120.1}$	0.0293	0.0095
11.6	$2309.0^{+2100.3}_{-789.7}$	0.1661	0.0624
21.0	$300.7^{+270.4}_{-80.3}$	0.0213	0.0063
56.5	$2309.0^{+710.2}_{-220.3}$	0.0562	0.0174

### 4.4.6 Summary

In this chapter, an analysis with the aim of recovering long-transient signals injected in white noise is presented. This analysis is performed with a code that is based on a detection method called the  $\mathcal{F}$ -statistic. This code was originally designed to detect CW gravitational wave signals and was adapted by Prix et al in [1] to be used in transient signal searches. This type of search is done and reported in this work for the first time. A description of how the code performs the analysis as well as a detailed interpretation of the output are presented. A lesson learnt from this analysis was the need to perform long time-span searches in order to recover the total duration of the signal. Specifically, to model a complete signal distribution of a large set of injections (500) the time search band has to be of the order of  $\pm\tau$ , the duration of the signal. On the other hand, the frequency band needed to recover the signal frequency could be of only a few frequency bins. The latter is useful to optimise the length of a search.

# Chapter 5

## Search for long transient gravitational waves in the Engineering run 3 analysis

In this chapter a detailed description of the analysis of long transient signal injections in coloured noise data is presented. Firstly, a brief overview of the motivation for doing this analysis is presented, as well as the description of the ER3 experiment in which long transient signal injections were done. Then, the description of these injections, providing details of their duration, their GPS times, and the availability of “science data” for these signals, is presented. The generation of the injected signals as well as the methodologies followed for their validation are described in detail. Then, the characterisation of the coloured noise data in which the signals were injected is discussed. This includes the methodology used to eliminate the unwanted noise lines that were removed in order to build the noise distributions. The resultant distributions, as well as a comparison of the expected SNRs with the obtained values, are shown. Finally, a posterior analysis of re-injections of signals that couldn't

be recovered is presented. This new injections were done with signals with a larger initial amplitude. Also, the distribution of a set of 20 injections is presented. A discussion about the plausibility of recovering the parameters of these signals, like the duration or the frequency, is presented.

## 5.1 Data Generation: Engineering Run 3

Once the analysis of long transient gravitational waves in white noise is understood, the application of the method on data similar to what is expected to come from the detectors is necessary in order to compare the results obtained in these two analyses. For this, one can inject signals either in real noise produced by the detectors or in artificial noise generated based on the experience acquired when the characterisation of these noises was done.

Parallel to the upgrade of the gravitational wave detectors towards the new generation, engineering runs (ER) are carried out to test updates in data analysis and computing infrastructure. These runs are used by data analysts to test and develop techniques and novel detection tools such as noise characterisations, detectability methods, signal injection techniques and many other applications. The main aim of the ER is be ready to process the data from the new detectors from the start of their operation. These runs are meant to mimic the operation of the detectors during a science run. The success in the correct simulation of these exercises is related to the good performance of studies involving real data coming from the gravitational wave detectors.

An interesting feature of this ER is that each piece of data is unique, just as the data generated by the detectors, in the sense that they are associated with the real time at which they are created. In addition to the uniqueness of the data, these timing labels make these data more similar to the detector data because they are labeled with the same time resolution. According to

[77], the main aims of the first ER (ER1) were:

- to test important software/computing infrastructure
- to establish run procedures for the advanced detectors era
- to test detector characterisation using real subsystem data
- to measure progress on software for key science goals.

The dates in which these ER happened are shown in table 5.1. At the time of writing this work there have been five ER, and further engineering runs are planned in the future.

Table 5.1: **Engineering Runs dates.** The dates in which the ER happened are presented in this table. \* refers to the transition of the beginning date due to a soft start in ER3 which is the ER of main interest in this work.

ER	Initial date	End date
1	January 18, 2012	February 15, 2012
2	July 11, 2012	August 8, 2012
3	January 23, 2013*	February 25, 2013
4	July 15, 2013	August 30, 2013
5	January 15, 2014	February 28, 2014

ER3 is the main interest of this work because it was selected to be used for the injections of long transient gravitational wave signals. The main reason for this selection is the convenient timescale of this ER with respect to this study. According to the web page containing the main information of this run [78], ER3 main features were:

- The intention to add as few as possible new features to the existing infrastructure from ER2.
- Keep the emphasis on detector characterisations.

- The availability and usage for characterisation and data analysis of the pre-stabilized laser (PSL) subsystem at both LIGO sites. This PSL will provide the final level of power stability that the interferometer requires.

In addition, and given that ER3 was based on the goals set for ER2, some of the goals in both ER were [79]:

- They involve data generated for both Hanford and Livingston LIGO sites as well as Virgo. All of them in their “advanced era” configurations.
- The major improvement in ER2 with respect to ER1 is the inclusion of instrumental influences in the simulated data.
- Data quality information was written directly on the frame files.

On the first days of ER3, less reliable data than expected were obtained. This is called a soft starting. As a consequence of this, ER3 had a transition of the official starting date from this soft start to February 5th, 2013.

### 5.1.1 Coloured noise data analysis

As mentioned before, the main characteristic of a more realistic analysis is the injection of signals in noise that has features similar to what is expected from gravitational wave detectors. Particularly, in the case of ER3 these features correspond to the ones expected when Advance LIGO and Advance VIRGO begin operations. These data has been called then, *coloured noise data* to distinguish them from the gaussian ‘white noise data’, and the addition of simulated features that mimic either environmental noise or detector noise is called *colouring noise data*. With this technique, features such as voltage harmonics and detector glitches are included in the noise. This colouring could be done in noise without any of the features mentioned before or in

noise that already has some of these spurious noise lines. The latter case is called *recolouring*.

ER3 data are recoloured data in which online detector characterisation channels (ODC) and a `gstlal` based calibration pipeline were used for this purpose. The latter produces a channel called FAKE-STRAIN, that recolours and down-samples to 16 kHz an existing 32 kHz channel named PSL-ISS\_PDB\_OUT\_DQ. It is on this channel FAKE-STRAIN where all the injections of this work were performed. ER3 science mode is determined by the segments generated in the data monitoring tool (DMT), which is a computational and human-based project that aims to produce reliable data.

The first element to be considered for these data is their reliability to be used as gravitational wave data. The principle is based on the operation of the detectors. As mentioned in section 1.4.2, the operation of the gravitational wave detectors is based on the interference principle of superimposed laser beams. When all the degrees of freedom of the interferometer are under control, setting the Michelson interferometer to be on a dark fringe, the interferometer is said to be “in lock”. Once the detector is in this stage, it is necessary to let the detector damp down any mechanical resonances in the mirror suspensions that might be triggered during the lock acquisition process. After this, the detector is said to be in “science mode” and the data collected while in this mode are *science data* to be used in gravitational wave searches.

It is on these data that injections and reliable gravitational wave analysis can be performed. Commonly in these data, noise artefacts appear and the data have to be cleaned. In a similar manner as in data coming from gravitational wave detectors, a noise cleaning of spurious data lines can lead to the loss of reliable data, and so it is of great importance to characterise with precision these unwanted lines. Data with spurious noise is available from the ER. In

order to perform injections into these data, firstly the signals to be injected have to be simulated separately in a noise-free environment and added later. The planned strategy of the ER considers these injections, but it could be the case that these injections are not performed as expected. If this happens, injections can be done manually posterior to the date in which the ER data are generated, since the data are available on line. In this work the signals were injected manually into the ER3 noise.

## 5.2 Transient Signal Injections

To do injections in data with spurious noise, firstly one has to select appropriate data segments for these injections. If the injection to be performed has a long duration, as in the long transient signals case, an initial criterium is to select science data segments separated enough between each other in order to avoid overlapping and, in so far as possible, with the appropriate length to contain the entire signal. The signals injected in this work have the parameters shown in table 5.2.

Table 5.2: Parameters of the signals injected in ER3 noise.

<b>Type I X-ray burst from PSR 4U 1608–522</b>	
Parameter	Initial date
RA (J2000)	16:12:43.0
DEC (J2000)	-52:25:23
$h_0$	$1.31 \times 10^{-24}$
$f_{\text{spin}}$ [Hz]	620
$f_{\text{signal}}$ [Hz]	826.6
$\tau$ [s]	$9.27 \times 10^3$

Some of these parameters come from astrophysical observations such as right ascension (RA), declination (DEC) and  $f_{\text{spin}}$ . The others were calculated as

follows:  $h_0$  using equation 3.38 and considering that the energy is equivalent to the total energy emitted by the burst ( $\sim 4 \times 10^{41}$  erg) reported in [43]. The duration of the signal  $\tau$  was calculated with the ratio of equations 3.11, the  $\tau_{GRR}$  and equation 3.14, associated with  $\tau_{vbl}$ . Finally the signal frequency is the  $r$ -mode frequency of equation 3.8. The ER3 data segments chosen to perform the injections are shown in table 5.3.

Table 5.3: **ER3 science segments for long transient signal injections.** This table presents the scientific data available that contains the long transient signal injections in ER3.

GPS time of injection	Detector	Initial GPS time	Final GPS time	Duration
1043712016-1043739920	H1	1043712016	1043713355	2886
		1043713365	1043714469	1104
		1043714479	1043717605	3126
	L1	1043717094	1043718778	1684
		1043719222	1043719622	400
		1043720062	1043720569	507
		1043726794	1043727009	215
		1043737401	1043757713	20312
	V1	1043714625	1043728625	14000
		1043731171	1043741378	10207
1043884816-1043912720	H1	No science data available		
	L1	1043873161	1043891220	18059
		1043893998	1043894025	27
		1043895569	1043895592	23
		1043896217	1043896617	400
		1043897013	1043897305	292
		1043897633	1043897636	3
		1043897965	1043898284	319
		1043898609	1043899549	940
	V1	1043901053	1044023321	122268
		1043714625	1043728625	14000
		1043870193	1043902821	32628
			1043902981	1043929677
1044057616-1044085520	H1	No science data available		
	L1	1044057297	1044076853	19556
		1044077285	1044093552	16267
	V1	1044026978	1044079408	52430
		1044079478	1044116501	37023

Three signals were injected in each of the detectors: LIGO Hanford (H1), LIGO Livingston (L1) and Virgo (V1). The starting times of these signals are separated by two days: 1043712016 or the 1st of February 2013, 1043884816 or the 3rd of February 2013 and 1044057616 or the 5th of February 2013, respectively. The GPS times for the second and third signals on H1 were not available as science data.

Injections in real data, either if the data are produced artificially for ER purposes or come from gravitational wave detectors, have to be done by summing noise free time series signals with the time series data contained in *frame files*. These format files have been adopted by the LIGO collaboration as an initiative of the VIRGO collaboration in order to homogenise the gravitational wave data storage. These files contain a lot of information about the data production such as the available channels, the sampling frequency, etc, as well as the time series of the data. Using these files, the injections in this work were done following the method shown in figure 5.1.

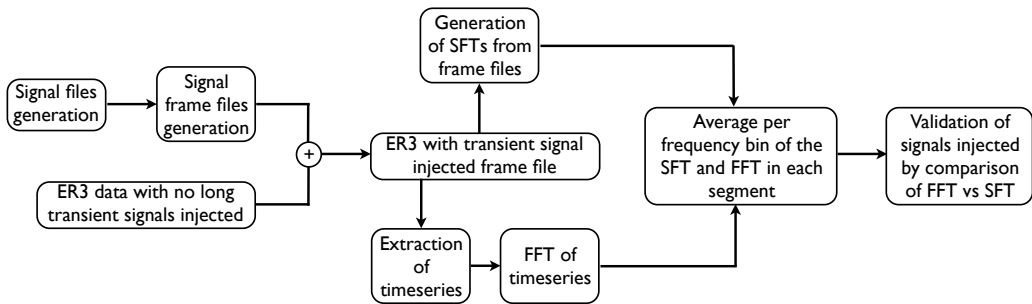


Figure 5.1: **Injection methodology and validation.** This methodology could be divided in three stages: (1) the generation of the frame files, (2) the comparison of the SFTs to be used in the analysis and the FFT of the time series, and (3) the validation of the data by comparing the SFT with the FFT.

As a first step, long transient signals were produced using the same tool (Mfdv4) as in the white noise analysis. Then, the time series files were trans-

formed to the frame format and were added to the frame files time series of the ER3 coloured noise data. With the new frame files containing the injections in coloured noise data, the SFT files useful for the analysis were generated. Also, the extraction of the time series from the frame files and their transformation to the frequency domain with a simple Fast Fourier Transform were done. Then, in order to compare the data, an average per frequency bin in all the segments was done and finally the validation by comparing the averages of the SFT and the FFT was performed. In principle, both sets of data should match. In a similar way, the validation of the only coloured noise data frame files was done following the method shown in figure 5.2. The difference between this method and the previous methodology description is that, once the SFTs are validated, the main aim is to use them to estimate the noise floor to be used for the optimal SNR calculation of the signal. This is the  $S_h(f)$  in equation 4.2. Resulting plots of these methodologies are shown in figures 5.3 and 5.4.

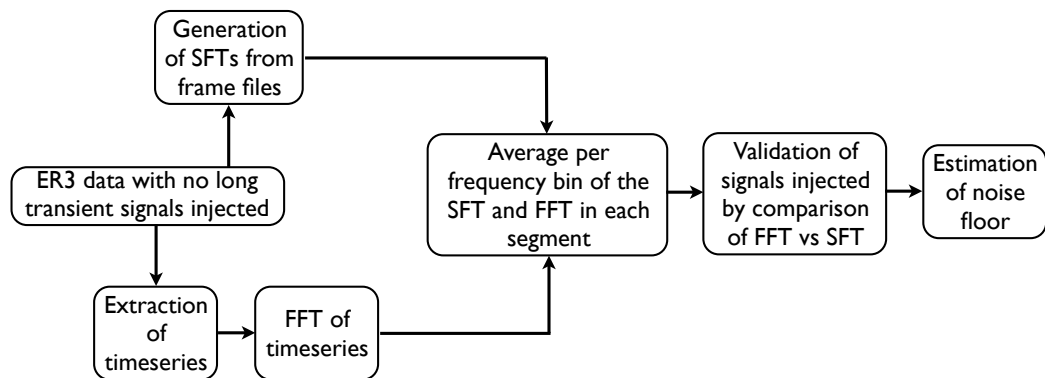


Figure 5.2: **Noise floor methodology and validation.** In this methodology a comparison of the SFTs generated from frame files with the FFTs created from the time series data in the frame files is done. Some resulting plots of this methodology are figures 5.3 and 5.4.

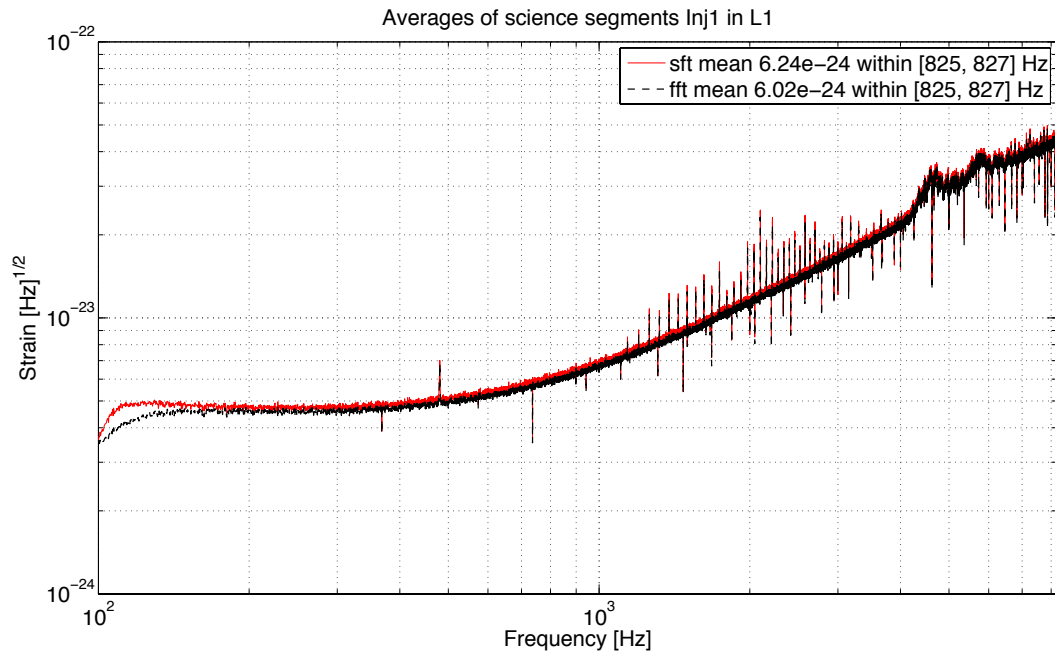


Figure 5.3: **Noise floor for injection 1 in L1**. In this comparison, a difference between the two distributions at frequencies  $\sim 100$  Hz can be seen. The fact that the signal injections are near 800 Hz, makes this discrepancy not significant.

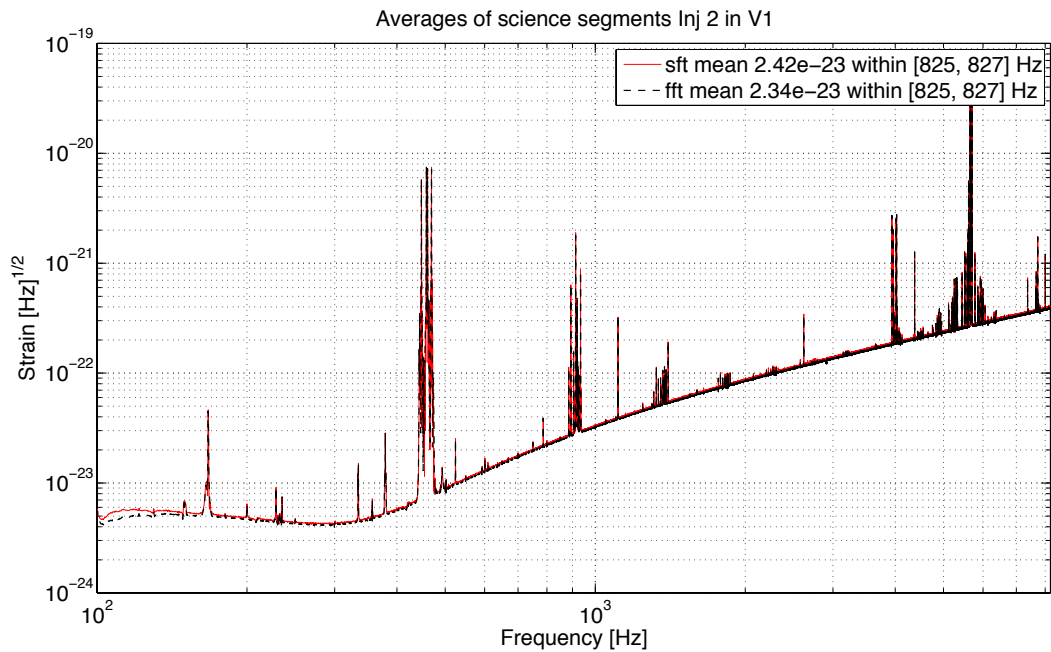


Figure 5.4: **Noise floor for injection 2 in V1**. As in the case of figure 5.3, the variation between the SFTs and the FFTs at lower frequencies is not relevant to the signal injection in the region of  $\sim 800$  Hz. It is of more significance the several noise lines in the region of the injection.

In figures 5.3 and 5.4, the similarities between the average per frequency bin of the SFTs and the FFTs of the science segments of two signals at two different detectors are presented. In figure 5.3 the injection of a signal in L1 data is presented, while figure 5.4 shows how a similar signal injection in the V1 noise realisation would look like. There are some small discrepancies at small frequencies in these plots. Since the frequencies of the injections lie above 800 Hz, the variations at lower frequencies do not represent a problem.

As a further check on the procedure to do the injections, a comparison of the same time span frame files between noise only ER3 data and data containing the injected signal was done. If the signal is strong enough, a very small variation at the signal frequency bin could appear. This is the case shown in figure 5.5, where a small bump represents this feature.

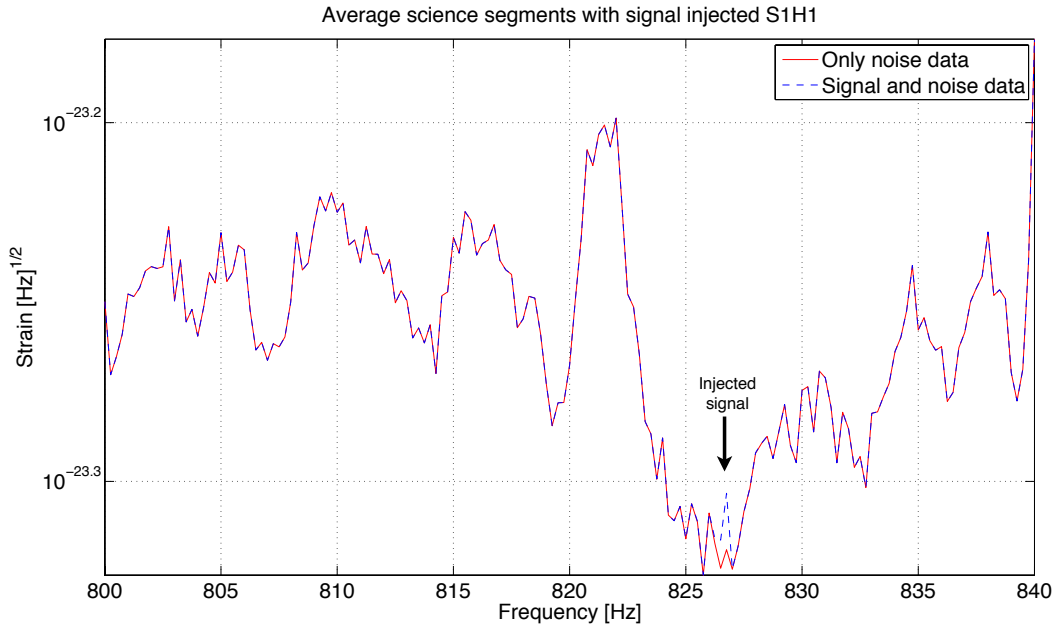


Figure 5.5: **Only noise frame file vs Signal + noise frame file.** The agreement between the noise only data and the signal+noise data is proof that the injection is done correctly. If the signal is strong enough with respect to the noise floor, a small bump can be seen at the signal frequency bin. Particularly, this plot shows a bump of a signal that has an overall SNR  $\sim 13$ .

## 5.3 Science data

In order to get an estimate of the detectability, the availability of science data in which the signals were injected has to be known. This is particularly important with ring down signals because, for the same amount of non-reliable data, there will be a different loss in the SNR depending on the section of the signal affected. In other words, if there is a loss of data in the first seconds of the signal where the amplitude is largest, the SNR will decrease more than if a similar loss of data is located at the end of the same signal where the amplitude is much smaller. To have this information available, the initial time and the duration of the signals have to be known and have to be truncated accordingly with gaps in the available science data. Based on this, a better estimate of the SNR can be obtained, and in consequence the results will be more reliable. From the science data segments provided in table 5.3, table 5.4 is constructed taking into account the percentage of the signal that is useful for analysis regardless of whether the unavailable data is at the beginning or at the end of the signal.

In figure 5.6, a graphical representation of the science segments of each of the injected signals, described in table 5.4, is presented. In these plots a contrasting difference between the useful data in red and the entire signal in blue is shown. These figures are presented to show that the effect of not having data at the beginning of the signal is different to the effect of not having data at the end of the signal, because of the exponential decay. As mentioned before, each of these injections is separated by two days in each detector. With the only useful signal for H1 an estimation of the signal SNR just considering the initial part is possible.

Injections 1 in all three detectors have less useful data than the other injections, probably due to the soft start of the ER3 run. There is also a variation

Table 5.4: **ER3 science segments of transient signals.** This table shows the science data used in these analyses that contains the transient signals injected in the ER3 data. The last column is of particular importance because it shows the percentage of the signal contained in science data. The first injections have less reliable data and the last injections are almost completely injected in reliable data.

GPS time of injection	IFO	Ini GPS time	Fin GPS time	Dur	Useful data <sub>[s]</sub>	total / useful [%]
1043712016-1043739920	H1	1043710469	1043713355	1339	5569	20.0
		1043713365	1043714469	1104		
		1043714479	1043717605	3126		
	L1	1043717120	1043718776	1656	4956	17.8
		1043719224	1043719620	396		
		1043720064	1043720568	504		
		1043737520	1043739920	2400		
	V1	1043714625	1043728625	14000	22749	81.5
		1043731171	1043739920	8749		
1043884816-1043912720	H1	No science data available				
	L1	1043884816	1043891220	6404	20048	71.8
		1043894000	1043894024	24		
		1043895572	1043895592	20		
		1043896220	1043896616	396		
		1043897016	1043897304	288		
		1043897968	1043898284	316		
		1043898612	1043899548	936		
	V1	1043884816	1043902820	18004	27740	99.4
		1043902984	1043912720	9736		
1044057616-1044085520	H1	No science data available				
	L1	1044057616	1044076852	19236	27468	98.4
		1044077288	1044085520	8232		
	V1	1044057616	1044079408	21792	27832	99.7
		1044079480	1044085520	6040		

of the initial amplitude of the signals of the H1 and L1 detectors with the V1 detector, probably due to the orientation of the detector. Fortunately, injections 2 and 3 in the V1 detector and injection 3 in L1 have most of the signal in science data. In consequence, the estimate of the SNR of these signals is expected to be similar to an ideal case in which neither gaps nor unwanted noise lines are present.

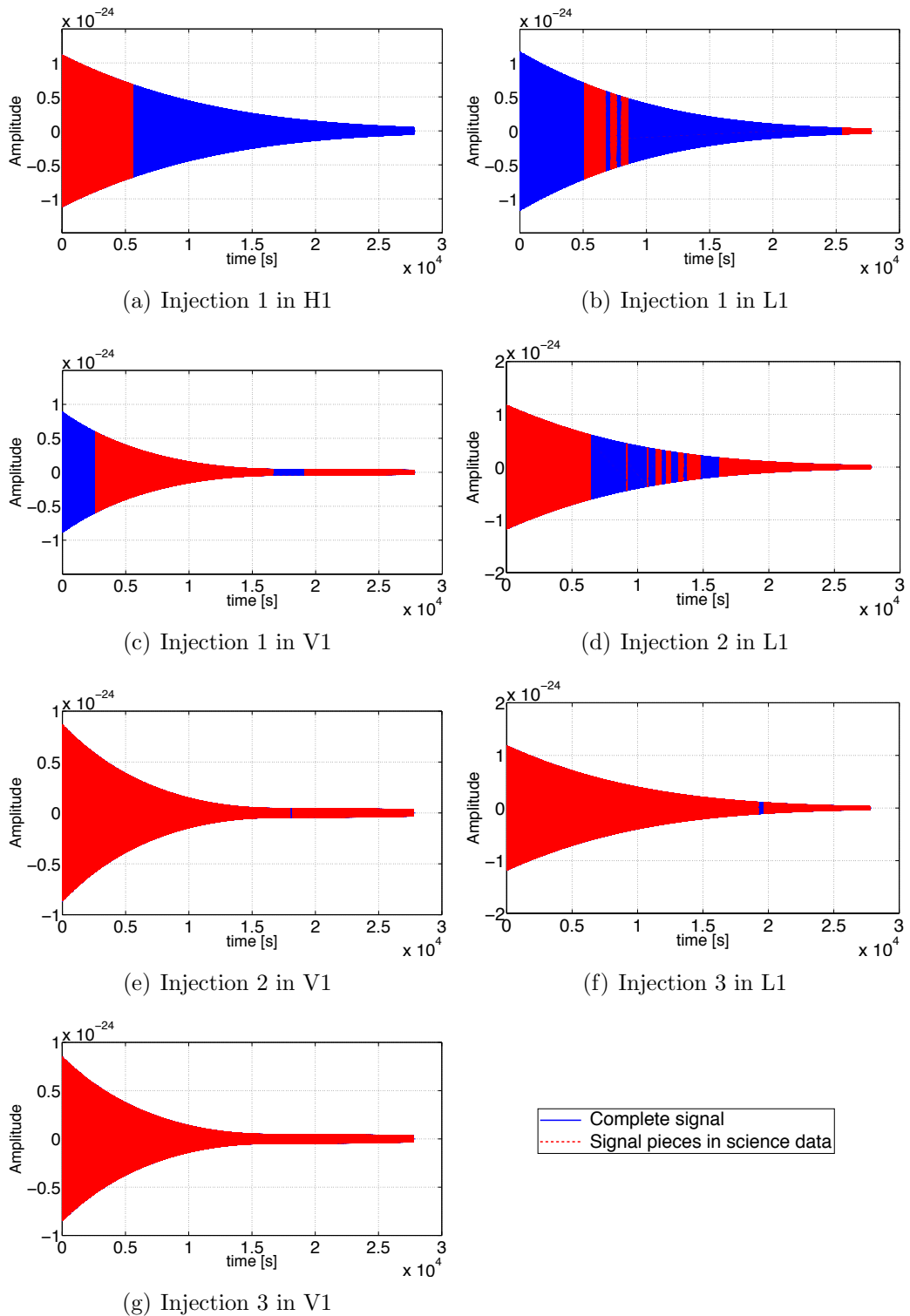


Figure 5.6: **Long transient signal injections in ER3.** This figure shows the long transient signals injected in ER3. The available science data at the time of the injections are plotted in red and they are contrasted with an ideal signal in blue. There was one signal within science data for the H1 detector, and three for L1 and V1, respectively.

As mentioned earlier in this chapter, the motivation for the ER is to compare the results of the analyses done in coloured noise data with the ones in white noise data. A comparison of the estimation of the expected SNR of the signals, calculated with equation 4.2 and assuming that there is no loss of data, with the SNR in the ER3 noise is presented in table 5.5. In addition, a comparison of the calculation of the expectation value following equation 4.20 of  $2\mathcal{F}$  for the complete signal and for the signal in the ER3 noise is shown.

Table 5.5: **Parameters of the signals injected in ER3 noise.** This table shows a comparison of the expectation values  $E[2\mathcal{F}]$ , calculated with equation 4.20, and the SNRs of the signals injected in science data including gaps on them, and ‘ideal’ signals. These ‘ideal’ cases are defined with hypothetical SNRs and  $E[2\mathcal{F}]$  for signals without any gaps on it.

Injection	SNR ideal	$E[2\mathcal{F}]$ ideal	SNR science data	$E[2\mathcal{F}]$ science data
Inj1H1	16.5	277.6	13.5	185.2
Inj1L1	12.9	170.2	4.9	27.8
Inj1V1	2.0	8.2	1.3	5.7
Inj2L1	12.9	169.9	11.6	137.9
Inj2V1	2.0	7.9	2.0	7.9
Inj3L1	13.2	178.5	13.2	178.5
Inj3V1	1.9	7.7	1.9	7.7

Table 5.5 shows a comparison of the SNR and  $E[2\mathcal{F}]$  of the signals injected in the science data with gaps, according to figure 5.6, with similar hypothetical signals without any gaps on them. This comparison is useful to estimate the loss of signal due to the discontinuous nature of the data. For the case of the injections in the V1 detector, even the signals without gaps have small SNRs. This is in agreement to what figures 5.3 and 5.4 show. The noise floor for V1 is higher than for the LIGO detectors. The expected values and SNR values in this table have to be tested against the numbers obtained in the analysis. In principle they should be similar, just as in the case of the white noise analysis.

## 5.4 Noise characterisation

When the corresponding tests show that the injections were done appropriately, the analysis process with the aim of recovering the signals takes place. In order to make a comparison with the white noise analysis, the coloured noise data analysis has to be done taking into account the same considerations described in sections 4.4.2 and 4.4.3. From the  $2\mathcal{F}/\max 2\mathcal{F}$  spectrum it is possible to recover not only an injected signal but also some other noise artefacts. These  $2\mathcal{F}/\max 2\mathcal{F}$  estimations of unwanted noise lines can be eliminated if they are unequivocally identified as detector artefacts or characterised environmental noise, otherwise they have to be kept.

Some examples of how these results look like are shown in figures 5.7 and 5.8. In these figures, the spectrum of the resulting statistics of CFSv2 for the L1 detector coloured noise data are presented. Noise lines that could be interpreted as gravitational wave signals are pointed with red arrows. In addition, in figure 5.8 the signal injected at 826.6 Hz is shown. There are no particular features in these noise lines that would help to distinguish them from an injection. The frequency at which they appear is the element to look at to select the unwanted noise lines. The CFSv2 analysis showed that the frequency of the signal can be recovered within a few frequency bins. In the first approach to the coloured noise data analysis shown in figures 5.7 and 5.8, a wider frequency search band has been used,  $\pm 20\%$  the signal frequency, in order to have a better understanding of the unwanted noise lines.

An investigation of the origin of the noise lines at the L1 detector shown in figures 5.7 and 5.8 was done. They are located at the frequencies 666.6 Hz, 736.34 Hz and 771.12 Hz. No identification of the origin of these lines was found. They were declared as noise lines for the purposes of this work, since they were not expected to be found.

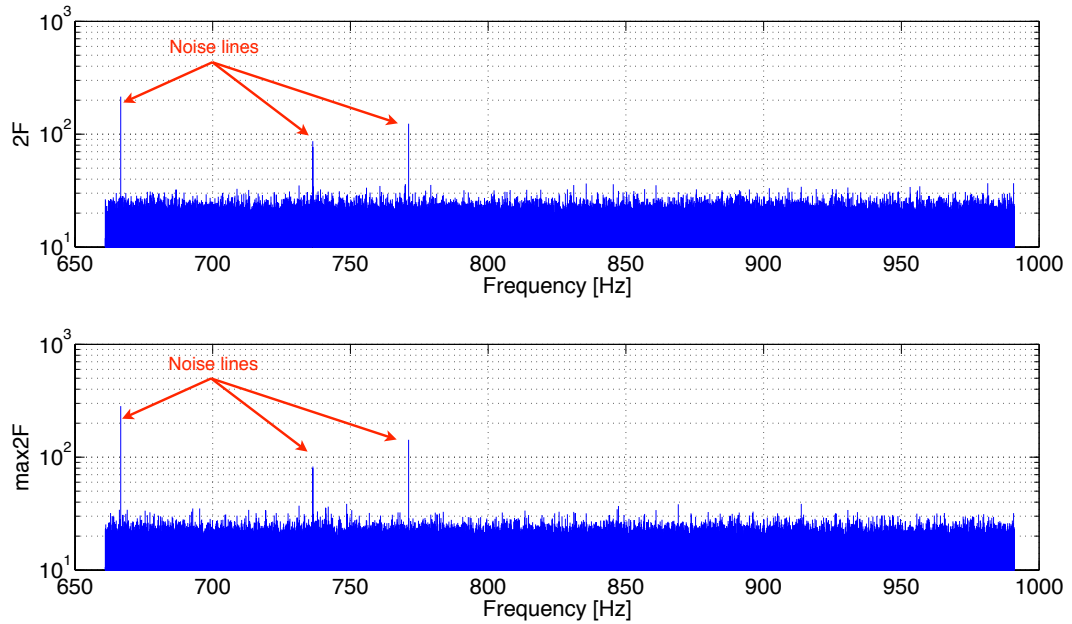


Figure 5.7: CFSv2 **spectrum in coloured noise data**. The difference between a white noise analysis and a coloured noise data analysis is the presence of noise lines that could be confused with signals injected in the noise. In this figure a spectrum of the  $2\mathcal{F}$  statistic in the top panel and  $\max 2\mathcal{F}$  in the bottom panel of a coloured noise data of the L1 detector is shown. With the exception of the lines pointed to by red arrows, the spectrum has a similar shape to the white noise analysis.

### 5.4.1 Unwanted noise lines

The characterisation of identified unwanted noise lines in the ER is based on the association of these artefacts to either environmental aspects around the detector, nearby injections or some other artefacts that have not been classified yet. A common set of unwanted noise lines are those associated with the voltage harmonics, which are the result of non-linear electric loads and affect the laser-based gravitational wave detectors. These harmonics appear in the noise as multiples of 60 Hz in the LIGO detectors and as multiples of 50 Hz in the VIRGO detector. In figure 5.9 a  $2\mathcal{F}/\max 2\mathcal{F}$  spectrum shows the presence of these harmonics with an injected signal between them. If the unwanted noise lines are present, the noise distribution of cannot be compared with a white noise distribution, so they have to be removed from the spectrum.

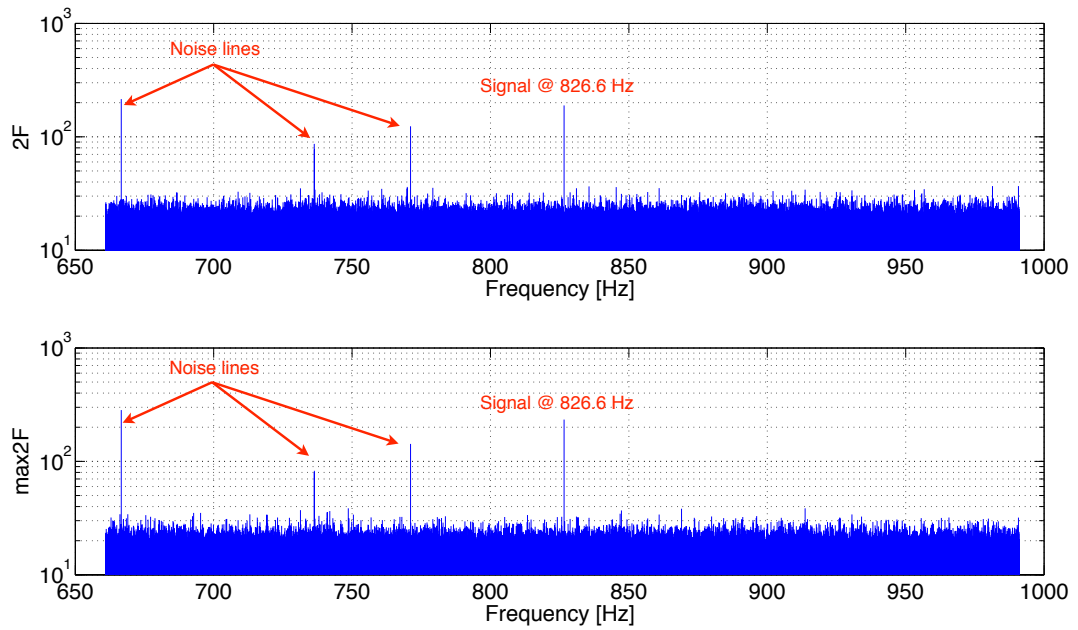


Figure 5.8: CFSv2 **spectrum in coloured noise data with signal injected**. In this figure, the spectrum of  $2\mathcal{F}$  and  $\max 2\mathcal{F}$  of the coloured noise data from the L1 detector containing an injection is shown.

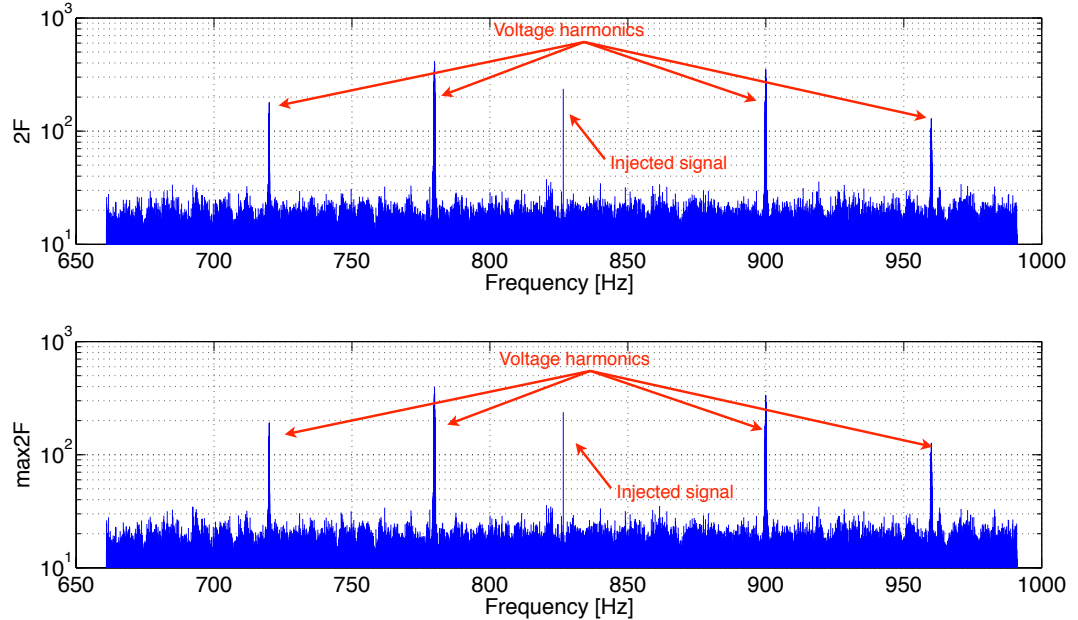


Figure 5.9: CFSv2 **spectrum of voltage harmonics and injected signal**.

In order to be removed, these noise lines have to be inspected in detailed in order to characterise them. Figure 5.10 shows a closer look at the CFSv2 output spectrum to a voltage harmonic near the injected signal. The harmonics are wide noise glitches that can be easily distinguished from the long transient signal injections which are thin peaks on the data.

Knowing this, the removal of the voltage harmonics is done assuming an average width of  $\pm 1$  Hz. In the context of a broad frequency search band, the data loss will not affect significantly the results. Figure 5.11 is presented as an example of the result of the removal of these harmonics on the  $2\mathcal{F}/\max 2\mathcal{F}$  spectrum. The logic consequence of this data removal is the appearance of gaps in the data.

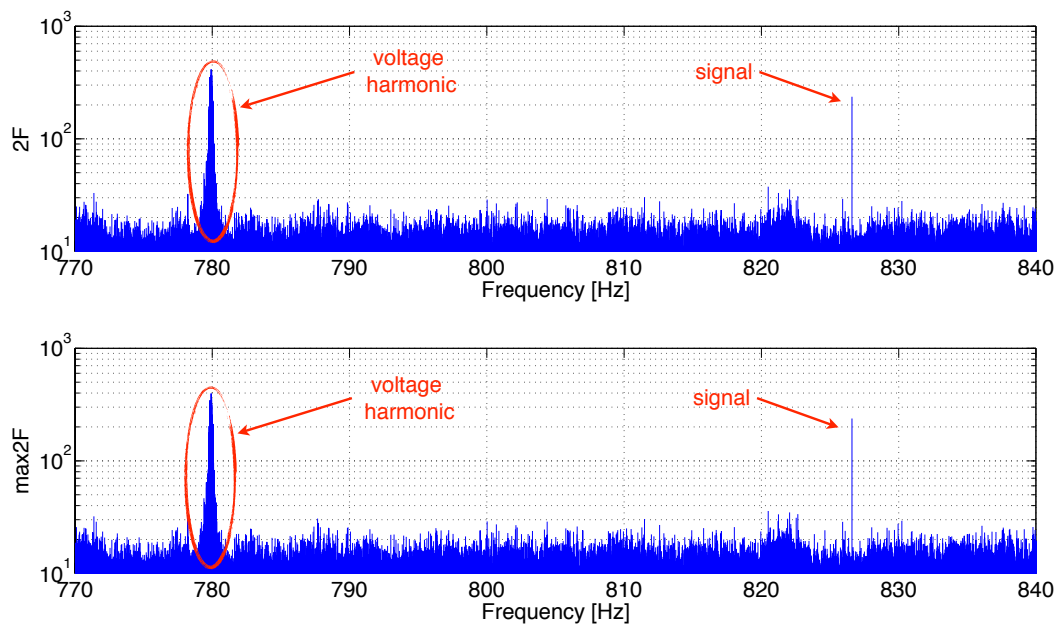


Figure 5.10: **Voltage harmonics data glitches and injected signal peak.** This figure shows how a voltage harmonic could be distinguished from a signal injection by its width.

The  $2\mathcal{F}/\max 2\mathcal{F}$  spectra takes white noise-like spectra containing small gaps as shown in figure 5.12. A comparison between the distributions of the spectra shown in figures 5.9 and 5.12 has to be done. When a noise line is identified,

the same removal process is done. For example, in figure 5.13, unwanted noise lines from different sources can be seen in the  $2\mathcal{F}/\max 2\mathcal{F}$  spectra of the second injection in VIRGO ER3 noise.

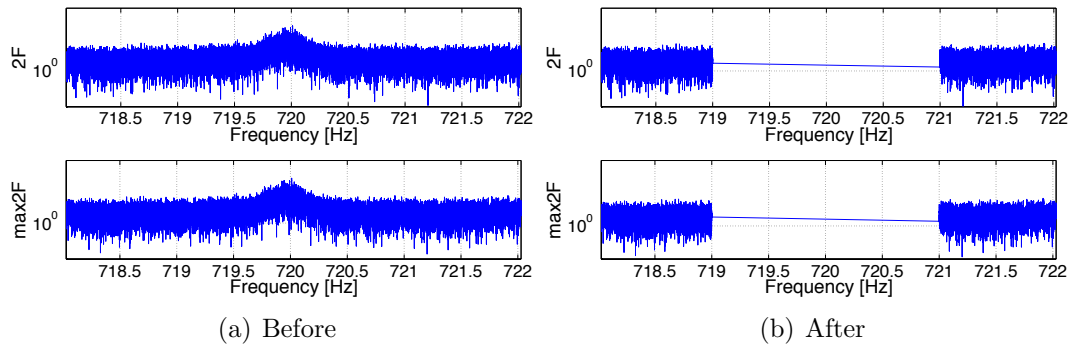


Figure 5.11: Voltage harmonic removal.

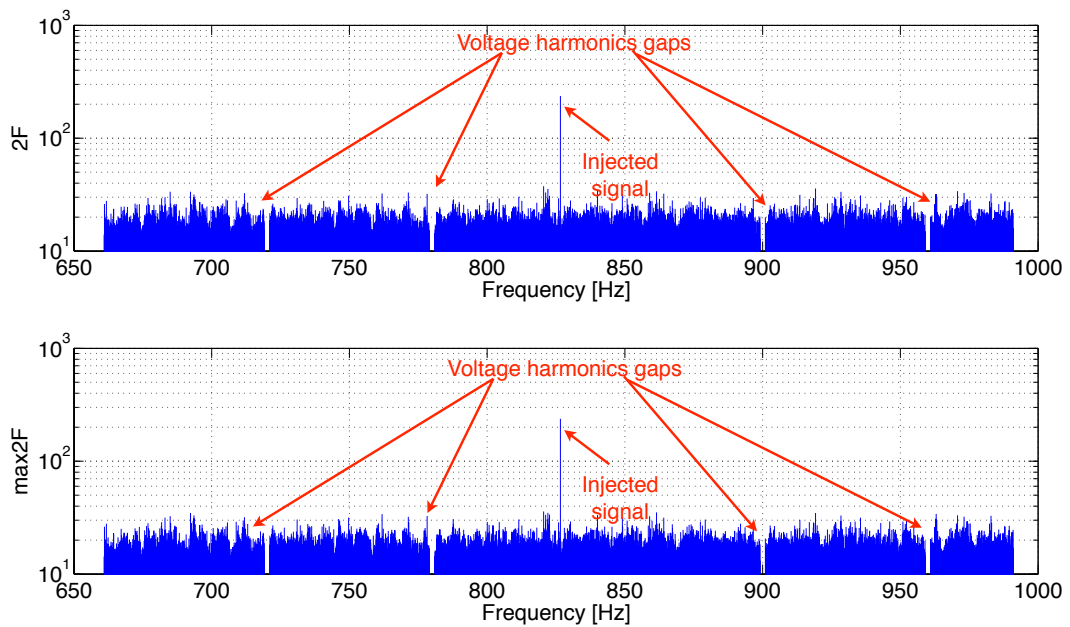


Figure 5.12: CFSv2 spectrum with removed voltage harmonics and injected signal.

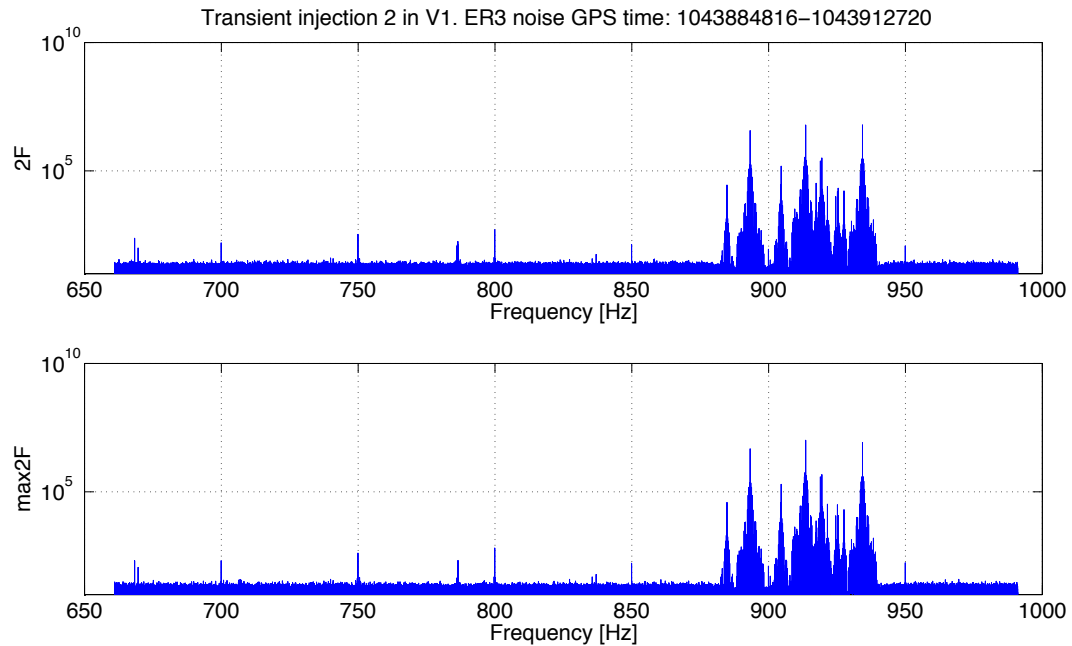


Figure 5.13: CFSv2 spectra of the VIRGO gravitational wave detector around the injected signal frequency of 826.6 Hz. This figure is presented as an example of the variety of unwanted noise lines that could appear when a broad frequency search band is used for an analysis.

Firstly, the voltage harmonics associated with the VIRGO detector at 700 Hz, 750 Hz, 800 Hz, 850, 900 Hz and 950 Hz are identified. Then, after being in communication with the VIRGO site scientists, the lines around 610 Hz were identified as cooling fans at the harmonic corrector unit [80]. The “forest” observed around 900 Hz corresponds to the suspension violin modes. This “forest” is the main cause of data loss ( $\sim 20\%$ ) shown in table 5.6. There was no identification of the noise lines around 786 Hz. The resultant noise distributions after the removal of the unwanted noise lines are shown in section 5.5.

Table 5.6: **Data loss after unwanted noise lines removal.** The percentage of data lost as a consequence of the unwanted noise lines removal is presented in this table. The analysis of injections 1 in the H1 detector as well as injections 1, 2 and 3 in detector L1 are presented in this thesis in section 5.5. Further injections were done in the V1 coloured noise data. These later injection analyses are presented in section 5.5.1.

Injection	% of loss
Inj1H1	2.42
Inj1L1	0.60
Inj2L1	0.60
Inj3L1	0.45
re-Inj2V1 <sub>10×</sub>	23.63
re-Inj3V1 <sub>5×</sub>	22.12

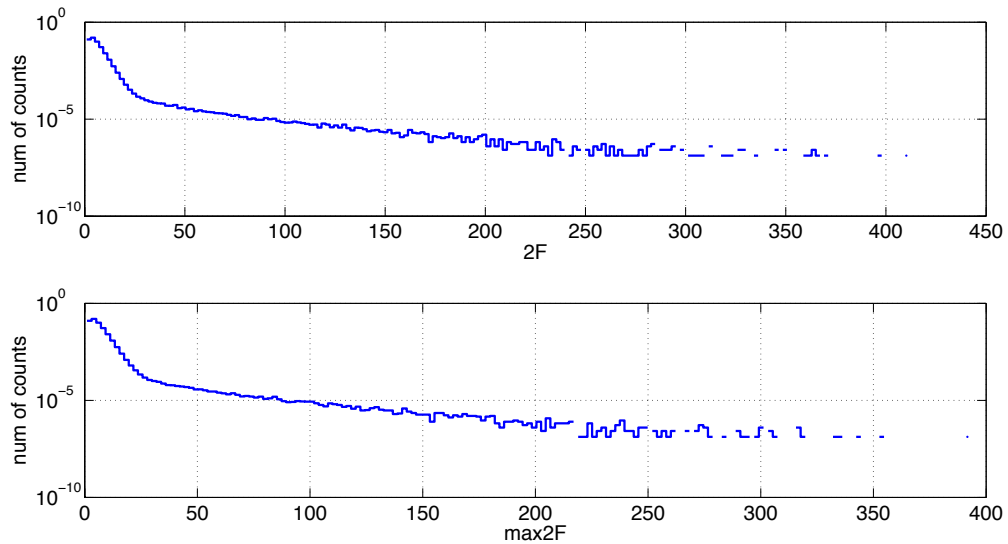
## 5.5 Results

As a consequence of removing data containing the unwanted noise lines, the distribution of the results changes. This is exemplified in figure 5.14.

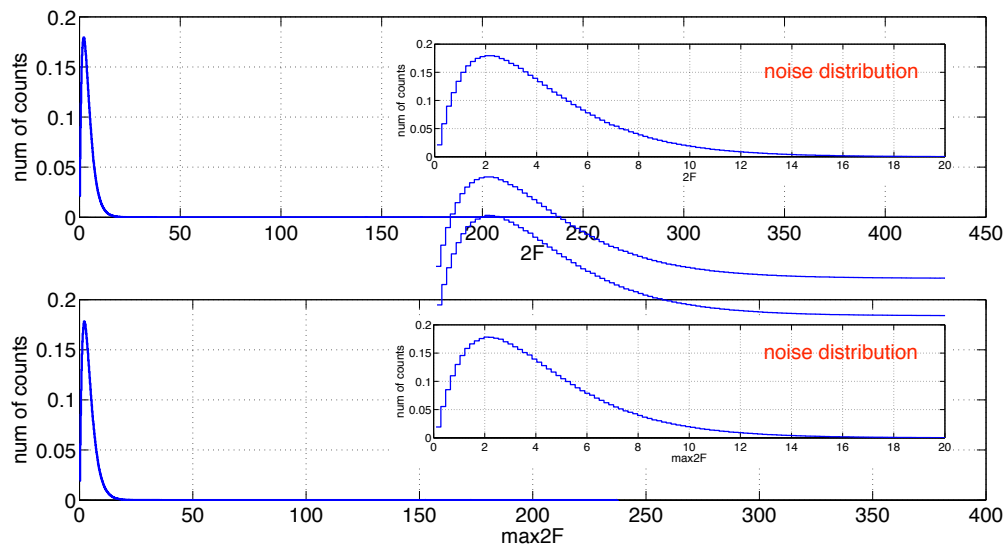
Contrasting figure 5.14(a) and figure 5.14(b) the difference of a noise + signal distribution before and after removing unwanted lines is presented. The latter distribution fits a  $\chi^2$  distribution with four degrees of freedom as expected. It is important to notice that the vertical axis in figure 5.14(a) is presented in a logarithmic scale in order to show the unwanted lines bins in the distribution. The tail of an unmodified distribution is dominated by noise lines and extends to larger values of the statistic. When these noise lines are removed, the tail distribution is expected to be shorter than the unmodified one. This effect can be seen by contrasting figures 5.14(a) and 5.14(b) in which the largest value of the statistic is associated to a higher statistic  $2\mathcal{F}$  and  $\max 2\mathcal{F}$ .

In table 5.7, the results of the CFSv2 analysis of long transient gravitational wave signals injected in ER3 are presented. From this table, it is important to highlight a failure in the recovery of the signals injected in V1 noise. In the case of the injections 2 and 3, the high noise floor in the vicinity of the signal led to small values of  $2\mathcal{F}$ . The case of injection 1 is probably due to

corrupted data. The action taken in all of these cases is described in section 5.5.1.



(a) Before unwanted noise lines removal



(b) After unwanted noise lines removal

Figure 5.14: **Noise + signal distributions of Injection 1 in H1 before and after the unwanted noise lines removal.** In figure (a) a logarithmic scale is used in order to show the effect on the distribution of the presence of the unwanted noise lines. (b) As a result of removing these unwanted noise lines the tail of the distribution gets shorter, having as the maximum value the statistic associated with the injected signal.

Table 5.7:  $2\mathcal{F}/\max 2\mathcal{F}$  values of long transient signals injected in ER3. In this table, the results of the CFSv2 analysis are presented. It is relevant to mention that all the three analyses in V1 data were not successful, because either the data was corrupted or the signals were too small. Further injections were done and are presented in section 5.5.1.

Injection	$2\mathcal{F}$ @ 826.6 Hz	$\text{SNR}_{2\mathcal{F}}$ @ 826.6 Hz	$\max 2\mathcal{F}$ @ 826.6 Hz	$\text{SNR}_{\max 2\mathcal{F}}$ @ 826.6 Hz
Inj1H1	236.5	15.2	237.7	15.3
Inj1L1	65.1	7.8	69.4	8.1
Inj1V1	21230.0	145.7	21420.0	146.3
Inj2L1	118.8	10.7	139.3	11.6
Inj2V1	10.6	2.6	11.1	2.7
Inj3L1	189.2	13.6	233.7	15.2
Inj3V1	12.1	2.8	15.9	3.4

On the other hand, the recovery of Injection 1 in H1, and all three injections in L1 were successful. In these cases, there is a less precise calculation of the SNR in the first injections, probably due to the soft start of ER3. In figures 5.15 and 5.16, the distributions of the noise + injected signal of these last cases are presented. In these figures, the fitting function for the noise is included as a reference. If the plot of the complete data including the signal were shown the distribution of the noise would be less clear. In principle, in data containing noise and signal, the highest value of the distribution is  $2\mathcal{F}$  and  $\max 2\mathcal{F}$  is associated with the signal and corresponds to the  $E[2\mathcal{F}]$  value of the signal. Apart from some variations, the distributions seem to fit the central  $\chi^2$  distribution with 4 degrees of freedom.

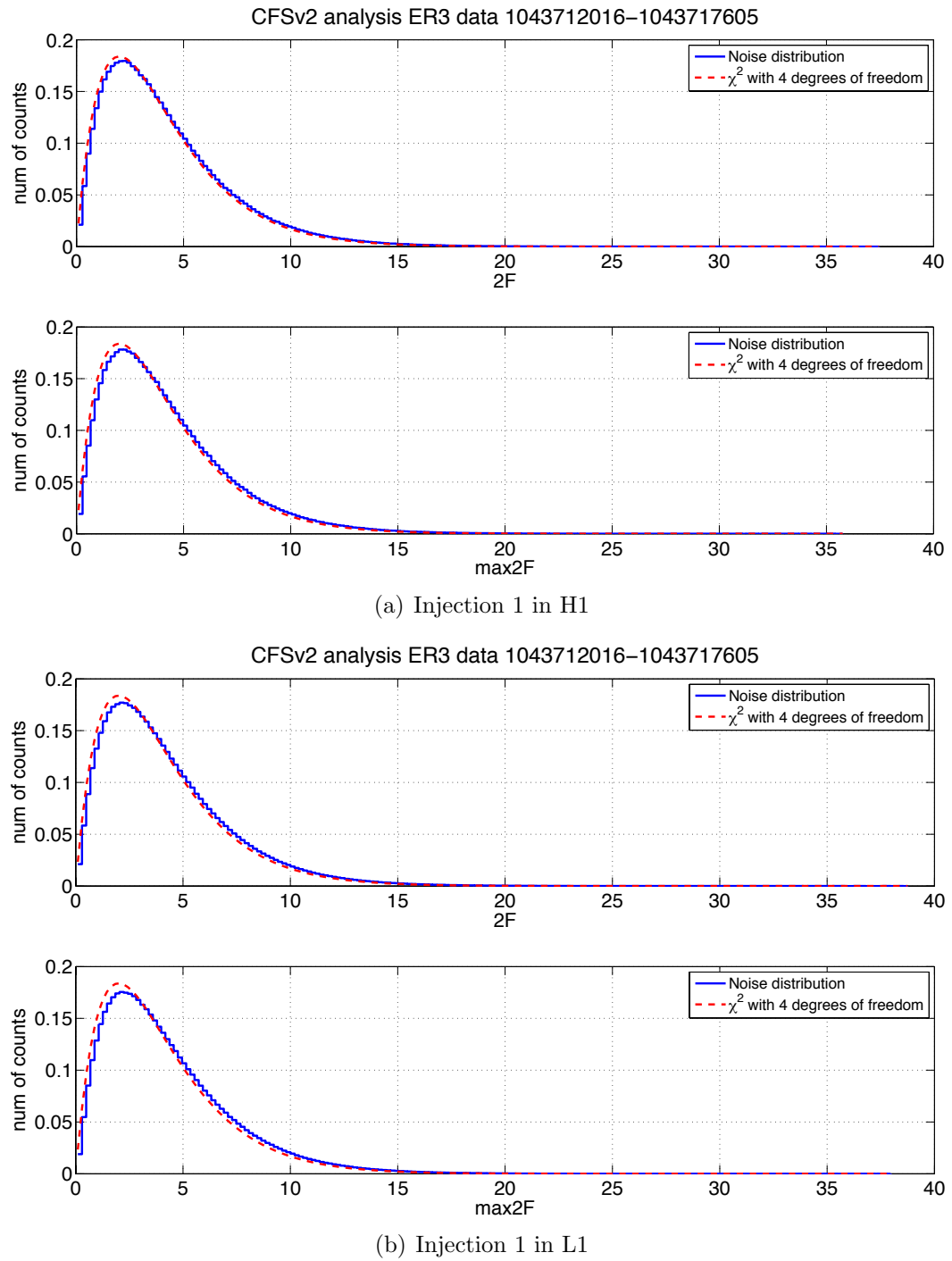
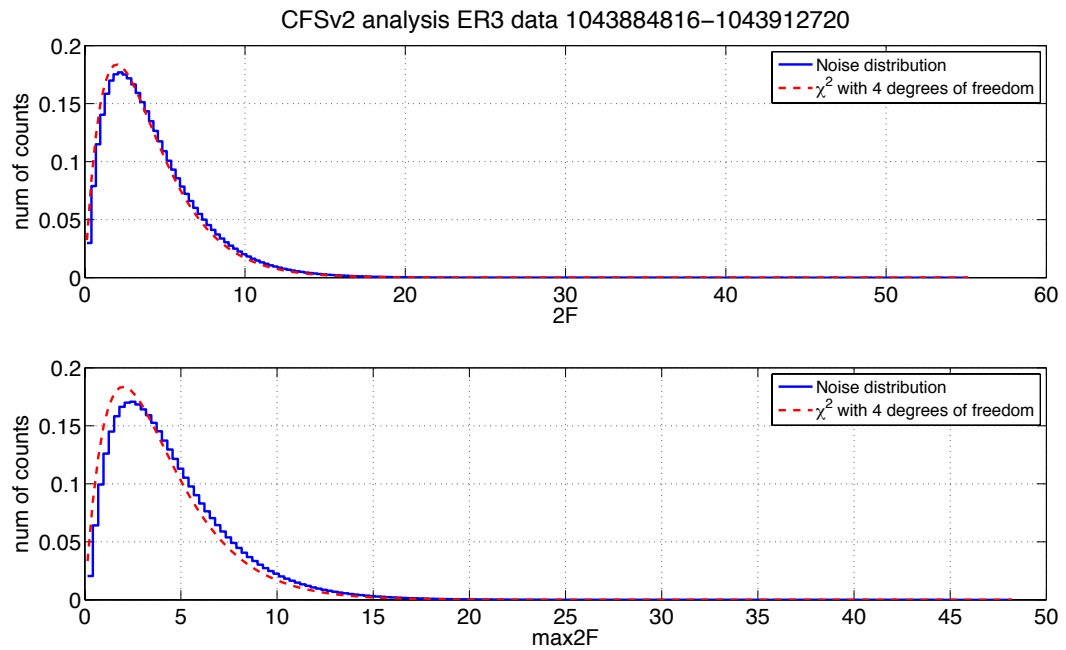
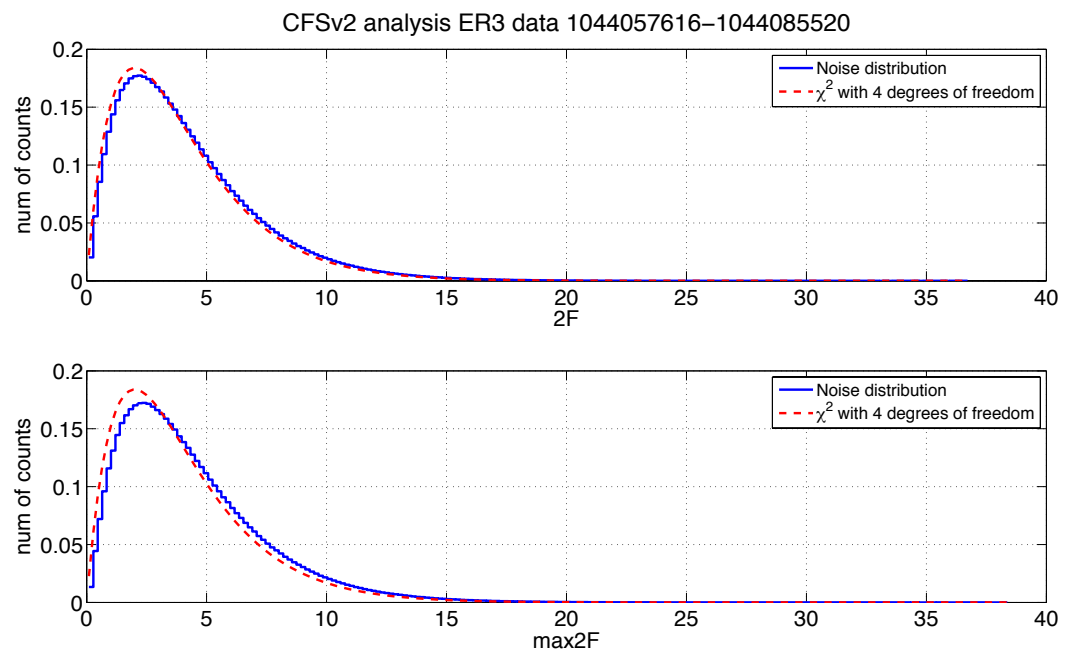


Figure 5.15: **ER3 noise distributions with long transient gravitational wave injections. Recovered injections 1 in H1 and L1.**



(a) Injection 2 in L1



(b) Injection 3 in L1

Figure 5.16: ER3 noise distributions with long transient gravitational wave injections. Injections 2 and 3 in L1.

### 5.5.1 V1 Reinjections

The unsuccessful recovery of injections 2 and 3 in V1 ER3 data brought the opportunity to test the feasibility of recovering larger signals and the capability of predicting the expectation value  $E[2\mathcal{F}]$ , as well as their SNR. In order to make two different tests, a signal  $10\times$  larger than the original injection was made in the Injection 2 V1 data. Another  $5\times$  larger injection than the original was done in the Injection 3 V1 data. The noise floor of both sets of data is fairly similar so a comparison between these new injections can take place. In table 5.8 the results of these injections as well as the comparison with the predicted values of  $E[2\mathcal{F}]$  and the SNRs are presented.

Table 5.8: **Reinjections in V1 ER3 data.**

Injection	$2\mathcal{F}$ @ 826.6 Hz	$\text{SNR}_{2\mathcal{F}}$ @ 826.6 Hz	$\text{max}2\mathcal{F}$ @ 826.6 Hz	$\text{SNR}_{\text{max}2\mathcal{F}}$ @ 826.6 Hz
re-Inj2V1 $_{10\times}$	403.7	20.0	483.2	21.9
re-Inj3V1 $_{5\times}$	116.2	10.6	143.3	11.8

From these results, a similarity with the predictions can be seen. These injections were done in three steps:

1. The original injected signal was removed by subtracting the frame files containing only the signal from the ER3 data.
2. Then, a contrasting process of these new data with the original ER3 V1 is done, in order to guarantee that there would be no overlap between injected signals.
3. Finally, a new injection and validation is done following the methodology described in figure 5.1.

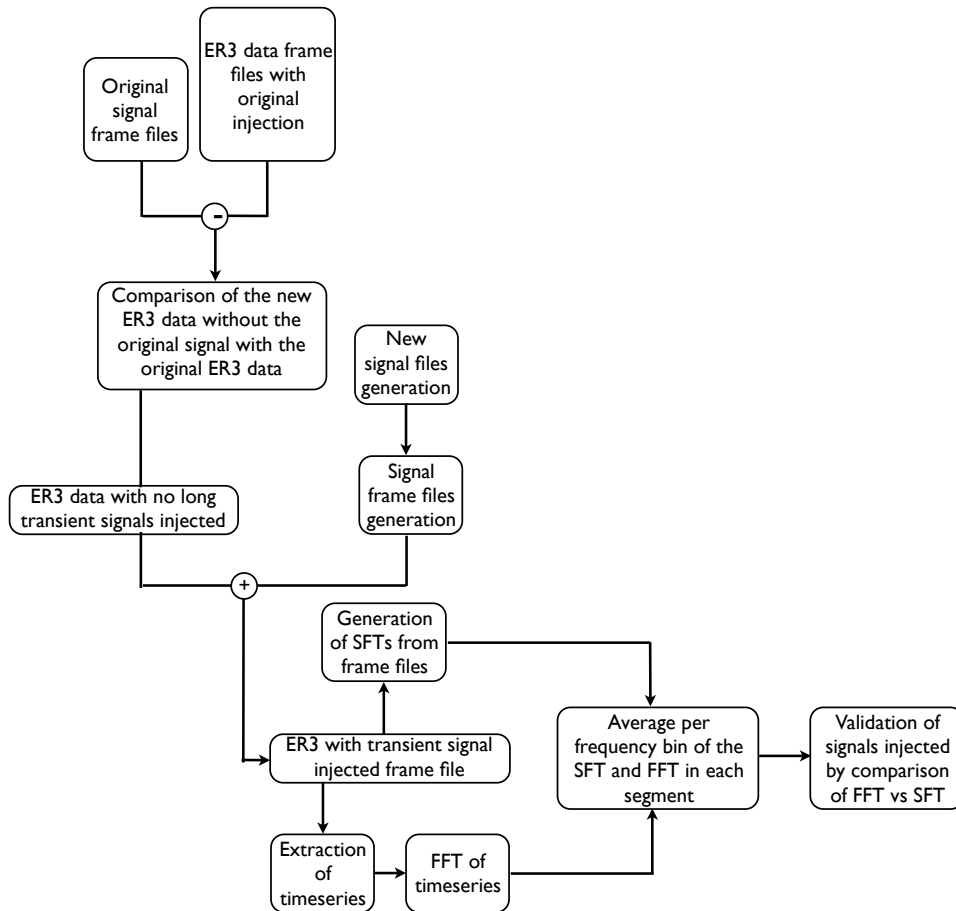
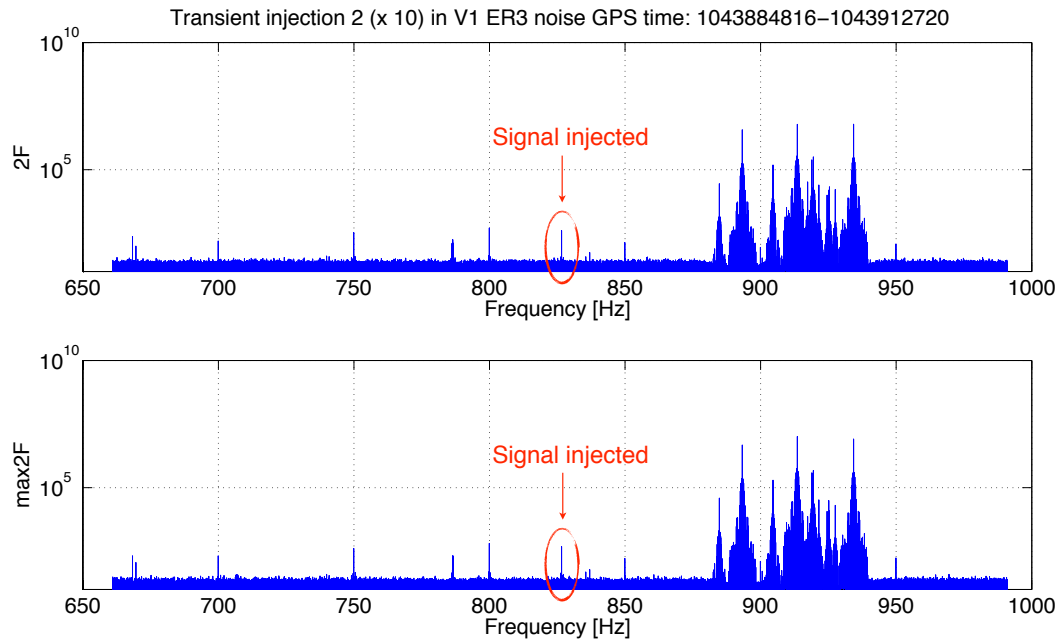
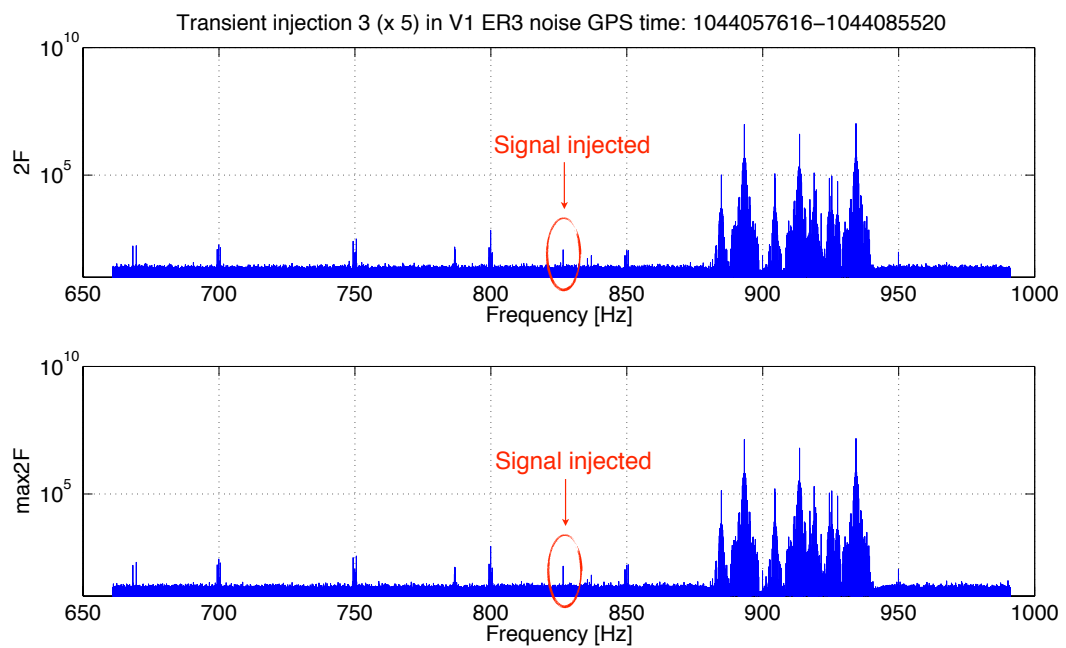


Figure 5.17: **Reinjection methodology and validation.** This methodology could be divided in two stages: (1) The subtraction of the original signal and validation of the data and (2) the injection of the new signal following the methodology in figure 5.1.

This methodology is presented in the form of a diagram in figure 5.17.

Figures 5.18 and 5.19 are presented so that they can be compared with figure 5.13. The difference between the formers and the latter is the new peaks that correspond to the new injections. The origin of the noise lines was discussed previously in section 5.4.1. And the corresponding noise distributions of the CFSv2 analysis done with the reinjections, containing the signal bin at the maximum value of the statistic  $2\mathcal{F}/\max 2\mathcal{F}$  are presented in figures 5.20 and 5.21.

Figure 5.18: Spectrum of the reinjected  $10\times$  the original signal in V1 data.Figure 5.19: Spectrum of the reinjected  $5\times$  the original signal in V1 data.

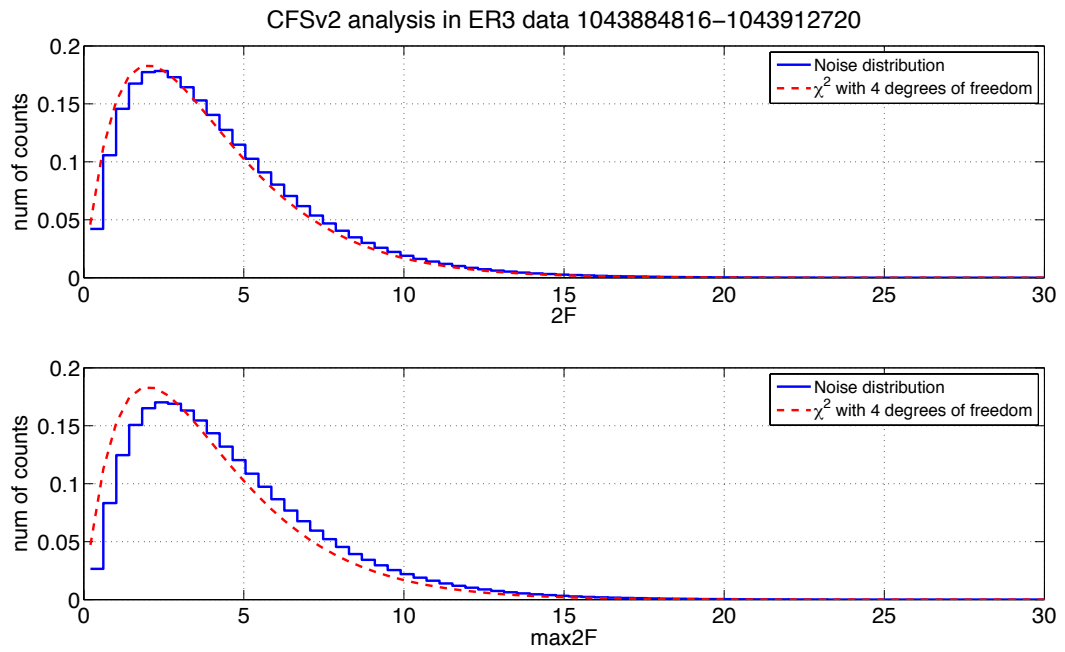


Figure 5.20: Noise distribution of the reinjected  $10\times$  the original signal in V1 data.

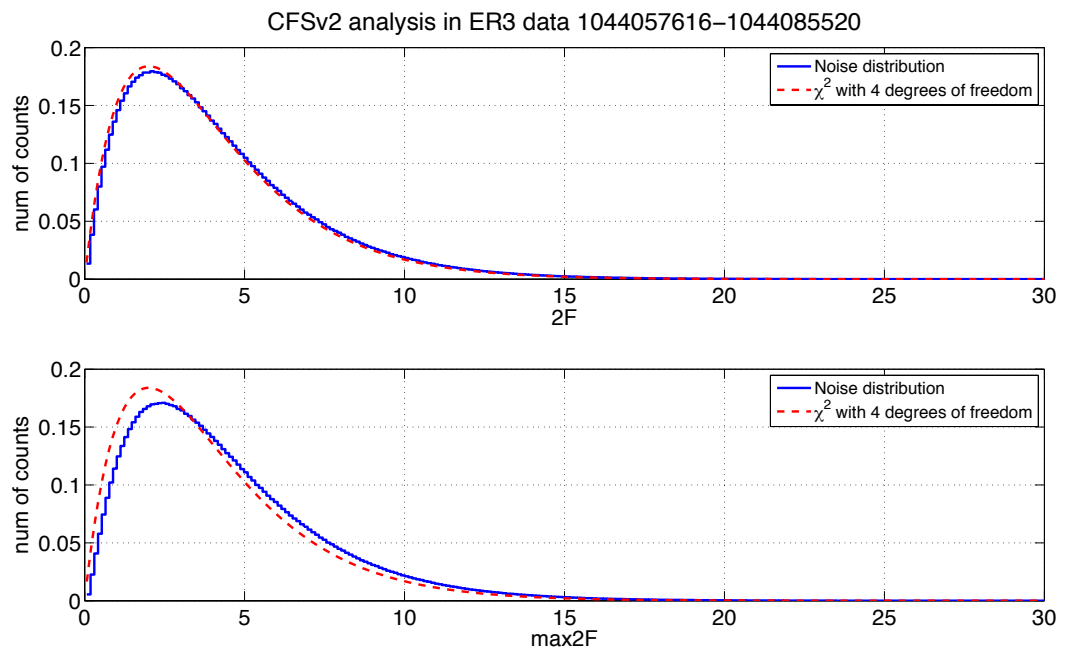


Figure 5.21: Noise distribution of the reinjected  $5\times$  the original signal in V1 data.

### 5.5.2 Signal distribution in ER3 data

As in the white noise analysis, knowing the distribution of the analysis output,  $\max 2\mathcal{F}$ , of several identical injections over different noise realisations will help to associate theoretical predictions to the observations. The challenge here is slightly different than in the white noise case because, in data with spurious noise, it is important to get gap-free data to be able to compare the results with the white noise analysis. Since in this study the injected signals are long transient signals, a very large time span is needed in order to do as many injections as possible. On the other hand, doing injections using the methods described earlier have a high computational cost. This is the reason why a total of 20 injections were done that, in comparison with the 500 injections in the white noise analysis, are too few but it is believed that they still give enough information for the purposes of this study. The expected value for  $2\mathcal{F}$  of these signals was  $\sim 93.8$ .

The timespan chosen was the last 540,662 seconds of the ER3 run at the L1 detector. The GPS time goes from 1045244956 to 1045785616 with an estimated  $S_h \sim 8.5 \times 10^{-24} \text{ Hz}^{-1/2}$ . The signal used for the injections was the same as in Injection 3 in L1 (see table 5.7), since it was the best estimate in the first coloured noise data injections trial. The analysis of these injections is shown in figure 5.22. In this figure, as well as in the white noise analysis, the recovery of the signal frequency is very efficient, so all the maximum values of  $\max 2\mathcal{F}$  of the 20 noise realisations, lies at that frequency. Despite the fact that the  $\tau$  interval is too small to model the distribution completely, a small amount of data seems to accumulate at the signal frequency as the middle panel shows. Unfortunately, the small amount of injections are not enough to build the distribution of the maximum value of  $\max 2\mathcal{F}$ , but the data are around the expectation value  $E[2\mathcal{F}]$ .

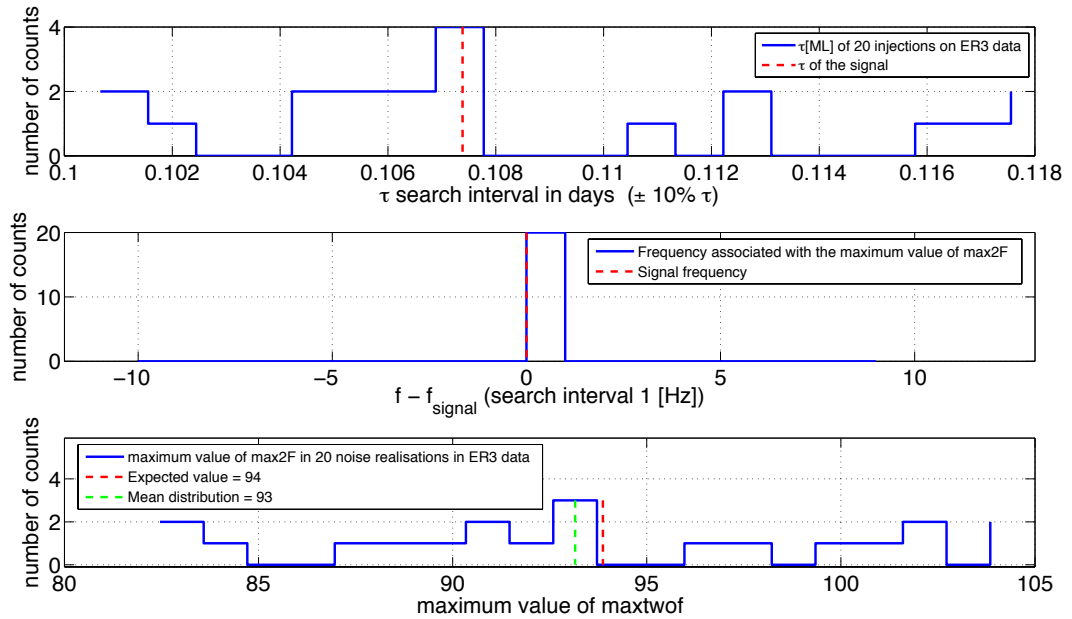


Figure 5.22: CFSv2 **distributions of 20 injections in ER3 data**] This figure shows in the bottom panel the distribution of the maximum value of  $\max 2\mathcal{F}$  of 20 injections in ER3-L1 data at different GPS times. Also, the distribution of the maximum likelihood of the duration of the signal and the signal frequency associated with maximum value of  $\max 2\mathcal{F}$  are presented in the top and middle panels, respectively.

### 5.5.3 Summary

In this chapter an analysis performed on signals injected in gravitational wave detector-like data is presented. The aim of this study is to compare the results obtained in chapter 4 with the ones obtained here. In order to make these results comparable, a characterisation of the detector artefacts and some other causes of non-gaussianity in the data were identified, and when possible removed. As in the Gaussian data analysis, a large time search band in order to model a distribution of the signal duration is needed. Also, just as in chapter 4, the signal frequency can be recovered using a narrow frequency search band. The need to perform an analysis with more than 20 injections is identified.

# Chapter 6

## Conclusions

In this thesis the plausibility of detecting long transient gravitational wave signals by second or third generation gravitational wave detectors was presented. This is of high importance at this time given that the first direct detection of gravitational waves seems to be imminent in the next few years with the construction of the Advanced LIGO and Advanced VIRGO detectors.

One of the contributions of this work lies on the analysis of signals with durations from  $10^2$  to  $10^4$  s that could be associated with gravitational wave emissions. Also, the frequency of these signals are associated with  $r$ -mode oscillations in the fluid interior of neutron stars. From these stars, two kinds of sources were considered in this analysis: pulsar timing glitches and Type I X-Ray bursts. The former from isolated neutron stars and the latter from binary systems in which one of the components is a neutron star.

As for the first one, from a database of 114 pulsars, the feasibility of detection was constrained to the fastest rotators, above  $f_{\text{star}} \geq 100$  Hz. Unfortunately, only one timing pulsar glitch from a millisecond pulsar has been registered, with a relatively small released energy. The observation of more glitches from millisecond pulsars will change the panorama of gravitational wave detection associated with pulsar timing glitches, because the equations that describe

---

these gravitational wave emissions are strongly dependent on the  $f_{\text{star}}$ . Type I X-Ray bursts, in the context of long transient gravitational wave emissions, are more plausible sources to achieve a detectability.

To reach this goal, it is important to be sure that the models considered describe stars under a stable regime. The re-interpretation of a model to assure the stability of the star is presented in this work, and the detection feasibility with future detectors is based on it.

The use of the  $\mathcal{F}$ -statistic based method for long transient gravitational wave analyses, in which the duration of a signal is used to maximise the detectability, is a good methodology to search for these kind of signals. In this work it is shown that there is an improvement on the gravitational wave signals detectability using this method with respect to the traditional  $\mathcal{F}$ -statistic analysis used in previous studies.

In the context of a gaussian white noise environment, simulated gravitational wave signals can be recovered as the method predicts with a relative efficiency. In order to recover the duration of the injected signal, a broad search band that depends on the length of the signals has to be performed. But the recovery of the signal frequency requires a small frequency search range of a few frequency bins. This leaves the uncertainty of the  $r$ -mode frequency as the main consideration to perform a signal frequency search in real data coming from gravitational wave detectors. With an appropriate search methodology that involves parallel computing techniques, the analysis of long signals of  $10^4$  s is possible. In a similar way as in the white noise analysis, the search for these kind of signals in a less ideal case, such as data with spurious noise using this long transient gravitational wave search technique, is plausible to be used. For this, an appropriate characterisation of the data has to be done. The recovery of the signal frequency, as well as in the white noise analysis

case, requires a narrower search band than the one required for the signal duration, provided the above mentioned data characterisation. It is important to mention that in a real search, there is a big limitation in the amount of continuous data that might exist, given that the signals considered in this work are of the order of some hours.

All the searches of long transient gravitational wave signals using the maximisation of the  $\mathcal{F}$ -statistic reported in this work are searches targeted to a specific pre-known signal. A future implementation of this methodology to an all-sky search would be useful to observe neutron stars that are not visible through electromagnetic observations.

# Appendices

# Appendix A

## Pulsar glitches database

Table A.1: Pulsar glitch data base used in this analysis.

PSR	$f_{star}$ [Hz]	Dist [kpc]	$N_{gli}$	$\Delta\Omega/\Omega$ ( $\times 10^9$ )	epoch [MJD]	Ref.
J0146+6145	0.12	3.6	1	650.00	51141	[25]
J0147+5922	5.09	1.91	1	0.06	53682	[28]
J0157+6212	0.43	1.61	1	2.46	48512	[25]
J0205+6449	15.22	3.2	2	340.00	52555	[25]
				3800.00	52920	[25]
J0358+5413	6.39	1.1	6	5.56	46079	[25]
				4376.00	46469	[25]
				0.04	51673	[25]
				0.03	51965	[25]
				0.04	52941	[25]
				0.10	53216	[25]
J0406+6138	1.68	3.05	1	0.62	53041	[28]
J0502+4654	1.57	1.78	1	0.33	52616	[25, 26]
J0528+2200	0.27	2.28	3	1.30	42057	[27]
				1.46	52289	[27]
				0.17	53379	[27]
J0534+2200	30.23	2	26	4.00	40493.4	[25]
				2.20	41163	[27]
				2.00	41250	[27]
				44.00	42448	[25]
				1.10	43023	[27]
				2.80	43768	[27]
				4.10	46664.42	[25]
				85.00	47768.4	[27]
				4.50	48945.5	[25]
				2.70	50020.6	[25]
				22.00	50259.93	[25]
				7.67	50459.1	[25]
				6.67	50489	[25]
				8.67	50812.9	[25]
				9.67	51452.3	[25]
				24.00	51741	[25]
				3.30	51805.03	[27]
				23.60	52083.969	[27]
				8.00	52146.757	[27]
				2.60	52498.22	[27]
				1.10	52587.84	[27]
				210.00	53067.059	[27]
				4.84	53254.039	[27]
				2.80	53331	[26]
				21.80	53463.72	[26]
				4.70	53476.7	[26]
J0537-6910	62.03	48.1	23	681.00	51285	[27]
				449.00	51568	[27]
				315.00	51711	[27]
				140.00	51826	[27]
				141.00	51880	[27]
				456.00	51959	[27]
				185.00	52171	[27]
				427.00	52242	[27]
				168.00	52386	[27]
				217.00	52453	[27]
				421.00	52546	[27]

Table A.1 continued ...

PSR	$f_{star}$ [Hz]	Dist [kpc]	$N_{gli}$	$\Delta\Omega/\Omega$ ( $\times 10^9$ )	epoch [MJD]	Ref.
				144.00	52740	[27]
				256.00	52819	[27]
				234.00	52887	[27]
				338.00	53014	[27]
				18.00	53125	[27]
				392.00	53145	[27]
				395.00	53288	[27]
				259.00	53446	[27]
				322.00	53551	[27]
				402.00	53699	[27]
				236.00	53860	[27]
				18.00	53951	[27]
J0540-6919	19.80	48.1	1	1.90	51325	[27]
J0601-0527	2.53	7.54	1	0.19	51662	[27]
J0631+1036	3.47	6.54	12	5.10	50185.711	[27]
				3.70	50479.74	[27]
				57.90	50608.246	[27]
				1662.80	50730	[27]
				1.33	51911.133	[27]
				17.40	52852.586	[28]
				1.90	53228.387	[28]
				6.60	54129	[28]
				44.00	54632.41	[28]
				1.90	53366	[25, 26]
				1.10	53622.6	[25, 26]
				1.60	54170.4	[25, 26]
J0633+1746	4.22	0.16	1	0.62	50382	[25]
J0659+1414	2.60	0.29	2	0.60	50197	[26]
				1.30	51017	[26]
J0729-1448	3.97	4.37	5	24.80	52010	[26]
				23.00	54317.7	[26]
				13.00	54483.6	[26]
				12.00	54592	[26]
				6676.00	54687	[26]
J0729-1836	1.96	3.25	2	1.00	51421.9	[25, 26]
				4.00	52150	[25, 26]
J0742-2822	6.00	1.89	7	1.20	47625	[26]
				1.20	48331.7	[26]
				1.00	51770	[27]
				2.10	52027	[27]
				2.90	53090.2	[27]
				1.10	53469.7	[27]
J0758-1528	1.47	3.72	1	92.00	55020.469	[26]
J0835-4510	11.19	0.29	17	0.13	49948	[27]
				2340.00	40280	[27]
				2050.00	41192	[27]
				12.00	41312	[27]
				1990.00	42683	[27]
				3060.00	43693	[27]
				1145.00	44888.0707	[27]
				2050.00	45192	[27]
				1601.00	46257.2284	[27]
				1807.10	47519.803	[27]

Table A.1 continued ...

PSR	$f_{star}$ [Hz]	Dist [kpc]	$N_{gli}$	$\Delta\Omega/\Omega$ ( $\times 10^9$ )	epoch [MJD]	Ref.
				2715.00	48457.382	[27]
				5.60	48550	[27]
				835.00	49559.057	[27]
				199.00	49591.158	[27]
				2110.00	50369.345	[27]
				3120.00	51559.345	[27]
				2100.00	53195.09	[27]
				2620.00	53959.93	[27]
J1048-5832	8.09	2.98	3	19.00	48944	[27]
				3000.00	49034	[27]
				769.00	50788	[27]
J1048-5937	0.15	9	2	2910.00	52386	[25]
				16300.00	54185.91	[25]
J1105-6107	15.82	7.07	2	279.70	50417	[27]
				2.10	50610	[27]
J1119-6127	2.45	8.4	2	4.40	51398	[27]
				100.00	53300	[27]
J1123-6259	3.68	7.54	1	749.31	49705.87	[27]
J1141-3322	3.43	3.84	1	0.70	50551	[27]
J1141-6545	2.54	3.2	1	589.00	54277	[25]
J1302-6350	20.94	4.6	1	3.20	50690.7	[27]
J1328-4357	1.88	2.29	1	1.16	43590	[27]
J1341-6220	5.17	8.55	12	1507.00	47989	[27]
				24.20	48453	[27]
				990.00	48645	[27]
				10.00	49134	[27]
				142.00	49363	[27]
				33.00	49523	[27]
				11.00	49766	[27]
				16.00	49904	[27]
				1636.00	50008	[27]
				27.00	50321.7	[27]
				20.00	50528.9	[27]
				703.00	50683	[27]
J1357-6429	6.02	4.09	1	2425.00	52021	[27]
J1401-6357	1.19	2.6	1	2.49	48305	[27]
J1509+5531	1.35	2.13	1	0.22	41732	[27]
J1532+2745	0.89	0.98	1	0.29	49732	[26]
J1539-5626	4.11	4.01	1	2790.80	48165	[27]
J1614-5048	4.32	7.24	1	6460.00	49803	[27]
J1617-5055	14.42	6.46	1	600.00	49960	[27]
J1644-4559	2.20	5.3	3	191.00	43390	[27]
				803.60	46453	[27]
				1.61	47589	[27]
J1645-0317	2.58	2.91	7	0.89	40920	[25]
				1.47	41806	[25]
				1.98	43388	[25]
				2.60	45489	[25]
				2.25	48021	[25]
				1.43	50147	[25]
				2.64	51595	[25]
J1705-1906	3.34	1.18	1	0.44	48888	[27]

Table A.1 continued ...

PSR	$f_{star}$ [Hz]	Dist [kpc]	$N_{gli}$	$\Delta\Omega/\Omega$ ( $\times 10^9$ )	epoch [MJD]	Ref.
J1705-3423	3.92	3.75	2	0.59	51956	[26]
				0.57	54408	[26]
J1708-4009	0.09	3.8	6	561.00	51445	[26]
				4202.00	52016	[26]
				308.00	52990	[26]
				572.00	53366	[26]
				2707.00	53549	[26]
				737.00	53636	[26]
J1709-4429	9.76	1.82	1	2050.00	48780	[27]
J1720-1633	0.64	1.76	1	1.50	51169	[26]
J1721-3532	3.57	6.36	1	8.00	49969.7	[27]
J1730-3350	7.17	4.25	2	3080.00	47990	[27]
				3190.00	52139	[27]
J1731-4744	1.21	4.98	3	139.20	49397.3	[27]
				3.10	50703	[27]
				126.40	52472.7	[26]
J1737-3137	2.22	5.88	3	4.00	51553	[27]
				236.00	53052.8	[27]
				1342.40	54348	[26]
J1739-2903	3.10	3.19	1	3.09	46956	[27]
J1740-3015	1.65	3.28	34	420.00	47003	[27]
				33.00	47281	[27]
				7.00	47332	[27]
				30.00	47458	[27]
				600.90	47670.2	[27]
				4.00	48149	[27]
				642.00	48186	[27]
				48.00	48218	[27]
				15.70	48431	[27]
				9.10	49046	[27]
				169.70	49239	[27]
				9.50	49451.7	[27]
				3.00	49543.9	[27]
				439.30	50574.5497	[27]
				1443.00	50941.6182	[27]
				1.10	51334	[27]
				0.70	51685	[27]
				0.80	51822	[27]
				0.70	52007	[27]
				42.10	52235	[27]
				5.00	52240.2	[27]
				14.30	52266.8	[27]
				444.00	52271	[27]
				220.60	52344	[27]
				1.50	52603	[27]
				1.60	52759	[27]
				17.60	52859	[27]
				22.10	52943.5	[27]
				1850.00	53023.512	[27]
				0.80	53473	[26]
				42.00	54447.41	[28]
				2.20	54694	[28]
				5.20	54810.9	[26]
				2.30	54928.6	[26]

Table A.1 continued ...

PSR	$f_{star}$ [Hz]	Dist [kpc]	$N_{gli}$	$\Delta\Omega/\Omega$ ( $\times 10^9$ )	epoch [MJD]	Ref.
J1740+1000	6.49	1.36	1	1.20	54747.6	[26]
J1743-3150	0.41	3.65	1	1.60	49553	[27]
J1751-3323	1.82	9.27	2	2.30	53004	[28]
				3.00	54435	[28]
J1759-2205	2.17	3.54	1	28.00	51800	[27]
J1801-0357	1.09	7.13	1	2.90	48016	[27]
J1801-2304	2.40	13.49	9	200.00	46907	[27]
				231.20	47855	[27]
				347.68	48454	[27]
				64.00	49709	[27]
				22.60	50055	[27]
				80.60	50363.414	[27]
				4.00	50938	[27]
				651.00	52126	[27]
				499.00	53356	[27]
J1801-2451	8.00	4.61	5	1988.00	49476	[27]
				1247.00	50651	[27]
				3755.80	52054	[26]
				3101.00	54661	[26]
				16.10	53030.51	[27]
J1803-2137	7.48	3.94	4	4075.00	48245	[27]
				5.30	50269.4	[27]
				3185.00	50765	[27]
				3943.00	53429	[27]
J1806-2125	2.08	10.02	1	15615.00	51063	[27]
J1809-1917	12.09	3.71	1	1629.10	53250	[27]
J1812-1718	0.83	4.2	3	1.60	49926	[27]
				14.70	53105.68	[27]
				1.40	54365.8	[26]
J1809-2004	2.30	10.91	1	2.00	54196	[26]
J1814-1744	0.25	9.76	5	9.00	51384	[27]
				5.00	51700	[27]
				27.00	52094.96	[27]
				3.00	52241	[26]
				11.00	53756	[26]
J1818-1422	3.43	8.1	1	0.54	52057	[25]
J1819-1458	0.23	3.81	2	588.30	53924.79	[25]
				96.40	54168	[25]
J1824-1118	2.29	8.03	1	2877.00	54306	[26]
J1824-2452	327.41	4.9	1	0.01	51980	[27]
J1825-0935	1.30	1	10	0.20	49615	[27]
				12.60	49857	[27]
				5.21	49940	[27]
				12.60	50557	[27]
				20.00	51060	[27]
				31.40	51879	[27]
				29.00	52058	[27]
				1.80	52802.6	[27]
				7.20	53805	[28]
				122.00	54115.78	[28]
J1826-1334	9.85	4.12	4	2718.00	46507	[25]
				3049.00	49014	[25]
				3.40	53238.2	[25]
				2416.00	53734	[25]

Table A.1 continued ...

PSR	$f_{star}$ [Hz]	Dist [kpc]	$N_{gli}$	$\Delta\Omega/\Omega$ ( $\times 10^9$ )	epoch [MJD]	Ref.
J1830-1135	0.16	4.36	1	2.10	52367	[26]
J1833-0827	11.73	5.67	2	0.90	47541.3	[26]
				1864.80	48041	[27]
J1834-0731	1.95	4.85	1	4.40	53479	[26]
J1835-1106	6.03	3.08	1	27.00	52265	[27]
J1837-0559	4.97	5.01	1	3.20	53150	[26]
J1838-0453	2.63	8.28	2	26.00	52162	[26]
				9.00	54140	[26]
J1841-0425	5.37	5.17	1	578.50	53356	[27]
J1841-0524	2.24	4.86	3	29.00	53562	[26]
				25.00	54012.88	[26]
				1032.00	54503	[26]
J1841-0456	0.08	7.5	3	15170.00	52464	[26]
				2450.00	52997.05	[26]
				1390.00	53823.97	[26]
J1844+00	2.17	6.65	2	0.30	51435	[26]
				5.20	51722.5	[26]
J1844-0538	3.91	6.18	2	0.80	47438	[27]
				0.50	47955	[27]
J1845-0316	4.82	6.53	2	30.00	52128	[26]
				71.90	54170	[26]
J1846-0258	3.07	5.1	2	2.50	52210	[26]
				6200.00	53883	[26]
J1847-0130	0.15	7.74	2	15.00	53426	[26]
				80.00	54784.449	[26]
J1851-0029	1.93	6.86	1	0.90	54493	[26]
J1853+0545	7.91	4.77	1	1.49	53450	[28]
J1856+0113	3.74	3.3	1	11569.00	54123	[26]
J1901+0156	3.47	2.96	1	42.40	51318	[26]
J1901+0716	1.55	5.49	1	30.00	46859	[27]
J1902+0615	1.48	9.63	5	0.45	48645.11	[27]
				0.23	49441	[27]
				0.31	50311	[27]
				0.47	51165.9	[27]
				0.33	54248	[28]
J1908+0909	2.97	8.81	2	11.80	52240	[27]
				1.70	53340	[27]
J1909+0007	0.98	3.26	3	0.72	49491.9	[27]
				0.20	51224	[26]
				0.50	53546	[26]
J1909+1102	3.53	4.31	2	0.27	52700	[28]
				1.52	54050	[28]
J1910-0309	1.98	10.25	3	0.60	48241	[27]
				1.84	49219.85	[27]
				2.66	53232.75	[27]
J1910+0358	0.43	2.95	1	1.40	52331	[27]
J1913+0446	0.62	3.41	1	6.50	53499.7	[26]
J1913+0832	7.44	7.76	1	38.00	54653.908	[26]
J1913+1011	27.85	4.48	1	0.20	54431	[26]
J1915+1009	2.47	5.32	1	2.55	54162	[28]
J1918+1444	0.85	1.41	1	2.20	52285	[27]
J1919+0021	0.79	3.32	1	1.29	50174	[27]
J1926+0431	0.93	3.95	1	0.08	51495	[26]

Table A.1 continued ...

PSR	$f_{star}$ [Hz]	Dist [kpc]	$N_{gli}$	$\Delta\Omega/\Omega$ ( $\times 10^9$ )	epoch [MJD]	Ref.
J1932+2220	6.92	9.8	5	4450.00	46900	[27]
				629.00	45989	[26]
				4457.00	50264	[27]
				12.00	52210	[27]
				12.00	52394	[27]
J1937+2544	4.98	2.76	1	0.03	52032	[26]
J1946+2611	2.30	7.78	1	70.00	53326	[27]
J1952+3252	25.30	2.5	5	5.20	54103.44	[26]
				2.25	51967	[27]
				0.72	52385	[27]
				1.29	52912	[27]
				0.51	53305	[27]
J1955+5059	1.93	1.8	2	0.04	46964	[26]
				0.02	49038	[26]
J1957+2831	3.25	6.98	3	0.26	52485	[26]
				0.13	52912	[26]
				5.80	54692	[26]
J2021+3651	9.64	18.88	2	2587.00	52630.07	[27]
				745.00	54177	[26]
J2116+1414	2.27	4.43	3	0.20	47972	[27]
				0.07	49950	[27]
				0.11	51357	[27]
J2225+6535	1.47	2	5	1707.00	43072	[27]
				0.14	51900	[27]
				0.08	52950	[27]
				0.19	53434	[27]
J2229+6114	19.37	2.55	3	0.36	54266	[28]
				1133.00	53064	[27]
				327.00	54110	[26]
				4.50	54781.54	[26]
J2257+5909	2.72	6.4	1	0.92	49463.2	[27]
J2301+5852	0.14	7	1	4100.00	52443.9	[27]
J2337+6151	2.02	2.47	1	20000.00	53639	[27]

# Appendix B

## Uncertainties

### B.1 Uncertainties on $d\tau$

Once a distribution of the timescales associated with the detection statistic like `maxtwo $\mathcal{F}$`  is available, the uncertainty of the estimation of  $\tau$  can be performed. In order to get this estimation first the median of the distribution was calculated and then the 90% confidence level interval around the median.

An example of the calculation of this interval is shown in figure B.1

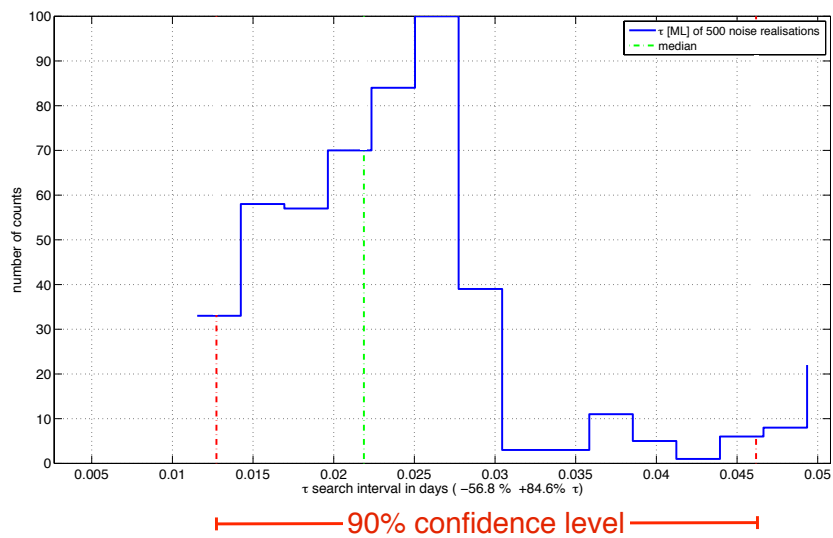


Figure B.1: **90% confidence interval calculation.** This plot shows the calculation of the confidence level using the timescale distribution in figure 4.8.

## B.2 Uncertainties on $F^{1/2} \left( \frac{\delta u}{u} \right)^2$

The timescale equation of Levin & Ushomisky can be written as

$$F^{1/2} \left( \frac{\delta u}{u} \right)^2 = \frac{\mathcal{K}}{\tau_{vbl}} \quad (\text{B.1})$$

where

$$\mathcal{K} = 73 \cdot \frac{M_{1.4} T_8 \rho}{R_{11.7}^2 \rho_b} \left( \frac{\text{kHz}}{f_{\text{star}}} \right)^{1/2},$$

If the right hand side of equation B.1 is called  $z$ , the uncertainty of it,  $dz$ , can be expressed as

$$\frac{dz}{z} = \left( \left( \frac{d\mathcal{K}}{\mathcal{K}} \right)^2 + \left( \frac{d\tau_{vbl}}{\tau_{vbl}} \right)^2 \right)^{1/2} \quad (\text{B.2})$$

that, assuming  $\mathcal{K}$  a constant, using equation B.1 and replacing  $z$  leads to

$$dz = \mathcal{K} \frac{d\tau_{vbl}}{\tau_{vbl}^2} \quad (\text{B.3})$$

When  $\mathcal{K}$  is replaced in equation B.3

$$d \left( F^{1/2} \left( \frac{\delta u}{u} \right)^2 \right) = \frac{73 \cdot \frac{M_{1.4} T_8 \rho}{R_{11.7}^2 \rho_b} \left( \frac{\text{kHz}}{f_{\text{star}}} \right)^{1/2}}{\tau_{vbl}^2} d\tau_{vbl} \quad (\text{B.4})$$

Finally, given that the total duration of the signal  $\tau$  is a function of  $\tau_{vbl}$  and  $\tau_{GRR}$ , the uncertainty of the duration of the signal has to be a function of these timescales. The equation that models  $\tau_{GRR}$  described by equation 3.11 of chapter 3, shows that this timescale is a function of physical parameters of the star, that in this context are set as constants, and so  $\tau_{GRR}$  will not contribute to the measure of the uncertainty of the total duration of the

---

signal. With this in mind, equation B.4 can be written as:

$$d \left( F^{1/2} \left( \frac{\delta u}{u} \right)^2 \right) = \frac{73 \cdot \frac{M_{1.4} T_8}{R_{11.7}^2} \frac{\rho}{\rho_b} \left( \frac{\text{kHz}}{f_{\text{star}}} \right)^{1/2}}{\tau^2} d\tau \quad (\text{B.5})$$

# Bibliography

- [1] R. Prix, S. Giampanis, and C. Messenger, “Search method for long-duration gravitational-wave transients from neutron stars,” *Phys. Rev. D*, vol. 84, p. 023007, Jul 2011.
- [2] Nobelprize.org, “The Nobel Prize in Physics 1921.” [http://www.nobelprize.org/nobel\\_prizes/physics/laureates/1921/](http://www.nobelprize.org/nobel_prizes/physics/laureates/1921/), Aug. 2012.
- [3] B. Schutz, *A First Course in General Relativity*. Cambridge University Press, 1985.
- [4] M. Hendry, “An Introduction to General Relativity, Gravitational Waves and Detection Principles VESF school.” [http://star-www.st-and.ac.uk/~hz4/gr/hendry\\_GRwaves.pdf](http://star-www.st-and.ac.uk/~hz4/gr/hendry_GRwaves.pdf), Aug. 2013.
- [5] D. Blair, *The Detection of Gravitational Waves*. Cambridge University Press, 1991.
- [6] E. E. Flanagan and S. A. Hughes, “The basics of gravitational wave theory,” *New Journal of Physics*, vol. 7, no. 1, p. 204, 2005.
- [7] C. W. Misner, K. S. Thorne, and J. A. Wheeler, *Gravitation*. W H Freeman and Company, 2 ed., 1973.

- 
- [8] The LIGO Scientific Collaboration, “Ligo: the laser interferometer gravitational-wave observatory,” *Reports on Progress in Physics*, vol. 72, no. 7, p. 076901, 2009.
- [9] J. L. Levine, “Early Gravity-Wave Detection Experiments 1960-1975,” *Physics in Perspective (PIP)*, vol. 6, pp. 42–75, 2004. 10.1007/s00016-003-0179-6.
- [10] O. D. Aguiar, “The Past, Present and Future of the Resonant-Mass Gravitational Wave Detectors,” *Res.Astron.Astrophys.*, vol. 11, pp. 1–42, 2011.
- [11] M. Pitkin, S. Reid, S. Rowan, and J. Hough, “Gravitational Wave Detection by Interferometry (Ground and Space),” *Living Reviews in Relativity*, vol. 14, no. 5, 2011.
- [12] S. Hild, “Beyond the second generation of laser-interferometric gravitational wave observatories,” *Classical and Quantum Gravity*, vol. 29, no. 12, p. 124006, 2012.
- [13] G. M. Harry and the LIGO Scientific Collaboration, “Advanced LIGO: the next generation of gravitational wave detectors,” *Classical and Quantum Gravity*, vol. 27, no. 8, p. 084006, 2010.
- [14] LVC, “Best Strain Sensitivities for the LIGO Interferometers - Comparisons Among S1 - S5 Runs LIGO Document G060009-x0,” Feb. 2011.
- [15] G. Hoobs and et al, “The International Pulsar Timing Array project: using pulsars as a gravitational wave detector,” *Classical and Quantum Gravity*, vol. 27, no. 8, p. 084013, 2010.
- [16] A. M. et al, “Einstein Gravitational Wave Telescope Conceptual Design Study,” *Available from European Gravitational Observatory*, no. document number ET-0106A-10, 2011.

- 
- [17] E. N. G. W. O. (NGO), “YellowBook NGO.” [ftp://ftp.rssd.esa.int/pub/ojennric/NGO\\_YB/NGO\\_YB.pdf](ftp://ftp.rssd.esa.int/pub/ojennric/NGO_YB/NGO_YB.pdf), Dec. 2011.
- [18] P. Amaro-Seoane and et al, “e LISA: Astrophysics and cosmology in the millihertz regime.” <http://arxiv.org/abs/1201.3621>, Jan. 2012.
- [19] B. Sathyaprakash and B. F. Schutz, “Physics, Astrophysics and Cosmology with Gravitational Waves,” *Living Reviews in Relativity*, vol. 12, no. 2, 2009.
- [20] K.S.Thorne, “Gravitational waves,” *Proceedings of the Snowmass’94 Summer Study on Particle and Nuclear Astrophysics and Cosmology*, pp. 160–84, 1995.
- [21] J. Abadie *et al.*, “Predictions for the Rates of Compact Binary Coalescences Observable by Ground-based Gravitational-wave Detectors,” *Class.Quant.Grav.*, vol. 27, p. 173001, 2010.
- [22] K. Riles, “Gravitational Waves: Sources, Detectors and Searches,” *Prog.Part.Nucl.Phys.*, vol. 68, pp. 1–54, 2013.
- [23] T. L. S. Collaboration, “Search for gravitational wave bursts from six magnetars,” *The Astrophysical Journal Letters*, vol. 734, no. 2, p. L35, 2011.
- [24] T. Gold, “Rotating Neutron Stars as the Origin of the Pulsating Radio Sources,” *Nature*, vol. 218, no. 5143, pp. 731–732, 1968.
- [25] R. N. Manchester, G. B. Hobbs, A. Teoh, and M. Hobbs, “The Australia Telescope National Facility Pulsar Catalogue,” *The Astronomical Journal*, vol. 129, no. 4, p. 1993, 2005. <http://www.atnf.csiro.au/research/pulsar/psrcat>.

- 
- [26] Cristobal M. Espinoza and Andrew G. Lyne and Ben W. Stappers and Michael Kramer, “A study of 315 glitches in the rotation of 102 pulsars,” *MNRAS*, 2010.
- [27] A. Melatos, C. Peralta, and J. S. B. Wyithe, “Avalanche dynamics of radio pulsar glitches,” *The Astrophysical Journal*, vol. 672, no. 2, p. 1103, 2008.
- [28] J. P. Yuan, N. Wang, R. N. Manchester, and Z. Y. Liu, “29 glitches detected at urumqi observatory,” *Monthly Notices of the Royal Astronomical Society*, vol. 404, no. 1, pp. 289–304, 2010.
- [29] W. Baade and F. Zwicky, “Cosmic Rays from Super-novae,” *Proceedings of the National Academy of Science*, vol. 20, pp. 259–263, May 1934.
- [30] P. J. Siemens, “Astrophysics: Softening of neutron stars,” *Nature*, no. 6002, p. 430430, 1985.
- [31] A. Hewish, S. J. Bell, J. D. H. Pilkington, P. F. Scott, and R. A. Collins, “Observation of a Rapidly Pulsating Radio Source,” *Nature*, vol. 217, pp. 709–713, Feb. 1968.
- [32] F. Pacini, “Energy Emission from a Neutron Star,” *Nature*, vol. 216, pp. 567–568, Nov. 1967.
- [33] A. G. Lyne and F. Graham-Smith, *Pulsar Astronomy*. Cambridge University Press, 2012.
- [34] M. Baldo, E. E. Saperstein, and S. V. Tolokonnikov, “Upper edge of the neutron star inner crust: The drip point and its vicinity,” *Phys. Rev. C*, vol. 76, p. 025803, Aug 2007.

- 
- [35] J. M. Lattimer and M. Prakash, “Neutron Star Structure and the Equation of State,” *The Astrophysical Journal*, vol. 550, no. 1, p. 426, 2001.
- [36] D. Lorimer, *Handbook of Pulsar Astronomy*. Cambridge Observing Handbooks for Research Astronomers, Cambridge University Press, 2005.
- [37] G. Hobbs, A. Lyne, and M. Kramer, “Pulsar Timing Noise,” *Chinese Journal of Astronomy and Astrophysics*, vol. 6, no. S2, p. 169, 2006.
- [38] B. L., E. R.I., and V. R. K.A., “Pulsar glitches as probes of neutron star interiors,” *Nature*, vol. 359, pp. 616–618, 1992.
- [39] G. Baym, C. Pethick, D. Pines, and M. Ruderman, “Spin up in neutron stars: The future of the Vela pulsar,” *Nature*, vol. 224, pp. 872–874, 1969.
- [40] P. W. Anderson and N. Itoh, “Pulsar glitches and restlessness as a hard superfluidity phenomenon,” *Nature*, vol. 256, pp. 25–27, July 1975.
- [41] R. D. R. Mandal, S. Konar, M. Dey, and J. Dey, “The micro-glitch in PSR B1821-24: a case for a strange pulsar?,” *Monthly Notices of the Royal Astronomical Society*, vol. 399, no. 2, pp. 822–826, 2009.
- [42] P. Kaaret, E. H. Morgan, R. Vanderspek, and J. A. Tomsick, “Discovery of the Millisecond X-Ray Pulsar HETE J1900.1 -2455,” *The Astrophysical Journal*, vol. 638, no. 2, p. 963, 2006.
- [43] L. Keek and J. in 't Zand, “On burning regimes and long duration X-ray bursts,” *PoS*, vol. INTEGRAL08, p. 032, 2008.
- [44] K. D. Kokkotas and B. Schmidt, “Quasi-Normal Modes of Stars and Black Holes,” *Living Reviews in Relativity*, vol. 2, no. 2, 1999.
- [45] S. Chandrasekhar, “Solutions of Two Problems in the Theory of Gravitational Radiation,” *Phys. Rev. Lett.*, vol. 24, pp. 611–615, Mar 1970.

- 
- [46] J. L. Friedman and B. F. Schutz, “Secular instability of rotating Newtonian stars,” *The Astrophysical Journal*, vol. 222, pp. 281–296, May 1978.
- [47] N. Andersson, K. D. Kokkotas, and N. Stergioulas, “On the Relevance of the  $r$ -Mode Instability for Accreting Neutron Stars and White Dwarfs,” *The Astrophysical Journal*, vol. 516, no. 1, p. 307, 1999.
- [48] K. Glampedakis and N. Andersson, “Hydrodynamical Trigger Mechanism for Pulsar Glitches,” *Phys. Rev. Lett.*, vol. 102, p. 141101, Apr 2009.
- [49] N. Andersson, “A New Class of Unstable Modes of Rotating Relativistic Stars,” *The Astrophysical Journal*, vol. 502, no. 2, p. 708, 1998.
- [50] Y. Levin and G. Ushomirsky, “Crust-core coupling and  $r$ -mode damping in neutron stars: a toy model,” *Monthly Notices of the Royal Astronomical Society*, vol. 324, no. 4, pp. 917–922, 2001.
- [51] I. Santiago-Prieto, I. S. Heng, D. I. Jones, and J. Clark, “Prospects for transient gravitational waves at  $r$ -mode frequencies associated with pulsar glitches,” *Journal of Physics: Conference Series*, vol. 363, no. 1, p. 012042, 2012.
- [52] T. L. S. Collaboration and S. Buchner, “Search for gravitational waves associated with the August 2006 timing glitch of the Vela pulsar,” *Phys. Rev. D*, vol. 83, p. 042001, Feb 2011.
- [53] B. J. Owen, “How to adapt broad-band gravitational-wave searches for  $r$ -modes,” *Phys. Rev. D*, vol. 82, p. 104002, Nov 2010.
- [54] H. P. Greenspan, *The Theory of Rotating Fluids*. Breukelen Press, 1990.

- 
- [55] K. H. Lockitch, J. L. Friedman, and N. Andersson, “Rotational modes of relativistic stars: Numerical results,” *Phys. Rev. D*, vol. 68, p. 124010, Dec 2003.
- [56] L. Lindblom, G. Mendell, and B. J. Owen, “Second-order rotational effects on the  $r$ -modes of neutron stars,” *Phys. Rev. D*, vol. 60, p. 064006, Aug 1999.
- [57] I. D. Jones, “Private communications,” 2011.
- [58] L. Lindblom, B. J. Owen, and S. M. Morsink, “Gravitational Radiation Instability in Hot Young Neutron Stars,” *Phys. Rev. Lett.*, vol. 80, pp. 4843–4846, Jun 1998.
- [59] B. J. Owen, “Gravitational waves from the  $r$ -modes of rapidly rotating neutron stars,” *AIP Conference Proceedings*, vol. 523, no. 1, pp. 55–64, 2000.
- [60] B. J. Owen, L. Lindblom, C. Cutler, B. F. Schutz, A. Vecchio, and N. Andersson, “Gravitational waves from hot young rapidly rotating neutron stars,” *Phys. Rev. D*, vol. 58, p. 084020, Sep 1998.
- [61] L. Bildsten and G. Ushomirsky, “Viscous Boundary-Layer Damping of  $r$ -Modes in Neutron Stars,” *The Astrophysical Journal Letters*, vol. 529, no. 1, p. L33, 2000.
- [62] P. Jaranowski, *Analysis of gravitational-wave data*. Cambridge New York: Cambridge University Press, 2009.
- [63] T. L. S. Collaboration, “First upper limits from LIGO on gravitational wave bursts,” *Phys. Rev. D*, vol. 69, p. 102001, May 2004.

- 
- [64] W. C. G. Ho, N. Andersson, and B. Haskell, “Revealing the physics of r-modes in low-mass x-ray binaries,” *Phys. Rev. Lett.*, vol. 107, p. 101101, Aug 2011.
- [65] B. Haskell, N. Degenaar, and W. C. G. Ho, “Constraining the physics of the r-mode instability in neutron stars with x-ray and ultraviolet observations,” *Monthly Notices of the Royal Astronomical Society*, vol. 424, no. 1, pp. 93–103, 2012.
- [66] D. Chakrabarty, E. H. Morgan, M. P. Muno, D. K. Galloway, R. Wijnands, *et al.*, “Nuclear-powered millisecond pulsars and the maximum spin frequency of neutron stars,” *Nature*, vol. 424, pp. 42–44, 2003.
- [67] A. Patruno, “The accreting millisecond x-ray pulsar igr j00291+5934: Evidence for a long timescale spin evolution,” *The Astrophysical Journal*, vol. 722, no. 1, p. 909, 2010.
- [68] A. L. Watts, B. Krishnan, L. Bildsten, and B. F. Schutz, “Detecting gravitational wave emission from the known accreting neutron stars,” *Monthly Notices of the Royal Astronomical Society*, vol. 389, no. 2, pp. 839–868, 2008.
- [69] L. Keek, J. J. M. in ’t Zand, E. Kuulkers, A. Cumming, E. F. Brown, and M. Suzuki, “First superburst from a classical low-mass x-ray binary transient,” *A&A*, vol. 479, no. 1, pp. 177–188, 2008.
- [70] T. E. Strohmayer, C. B. Markwardt, and E. Kuulkers, “Discovery of the spin frequency of 4u 0614+09 with the swift burst alert telescope,” *The Astrophysical Journal Letters*, vol. 672, no. 1, p. L37, 2008.
- [71] T. E. Strohmayer and C. B. Markwardt, “Evidence for a millisecond pulsar in 4u 1636-53 during a superburst,” 2002.

- 
- [72] A. P. Smale, W. Zhang, and N. E. White, “Discovery of kilohertz quasi-periodic oscillations from 4u 1820303 with rossi x-ray timing explorer,” *The Astrophysical Journal Letters*, vol. 483, no. 2, p. L119, 1997.
- [73] R. Wijnands, M. van der Klis, M. Mendez, J. van Paradijs, W. H. Lewin, *et al.*, “Discovery of kilohertz quasi-periodic oscillations in 4u 1735-44,” 1998.
- [74] S. Migliari, J. C. A. Miller-Jones, and D. M. Russell, “The influence of spin on jet power in neutron star x-ray binaries,” *Monthly Notices of the Royal Astronomical Society*, vol. 415, no. 3, pp. 2407–2416, 2011.
- [75] P. Jaranowski, A. Królak, and B. F. Schutz, “Data analysis of gravitational-wave signals from spinning neutron stars: The signal and its detection,” *Phys. Rev. D*, vol. 58, p. 063001, Aug 1998.
- [76] J. Clark, *An Evidence Based Search For Transient Gravitational Waves From Neutron Stars*. PhD thesis, University of Glasgow, 2008.
- [77] LVC, “Plans for the first aLIGO engineering run (ER1) LIGO Document G1101296-v1,” Feb. 2011.
- [78] LVC, “Engineering run 3.” [https://wiki.ligo.org/DAC/ER3#Engineering\\_Run\\_3](https://wiki.ligo.org/DAC/ER3#Engineering_Run_3), May 2013.
- [79] LVC, “Engineering run 2.” <https://wiki.ligo.org/DAC/ER2>, Sept. 2012.
- [80] V. collaboration, “VIRGO logbook.” [https://tds.ego-gw.it/itf/osl\\_virgo/index.php?callRep=30954](https://tds.ego-gw.it/itf/osl_virgo/index.php?callRep=30954), 2013.